FREE ENERGY CALCULATIONS OF CONFORMATIONAL TRANSITIONS IN SUPRAMOLECULES AND AMPHIPHILIC BILAYERS

Tolpekina, T.V.
Free energy calculations of conformational transitions
in supramolecules and amphiphilic bilayers
Thesis, University of Twente, Enschede
– with refences – summary in Dutch
ISBN: 90–365–2092–4.

Printed by: Print Partners Ipskamp, Enschede

FREE ENERGY CALCULATIONS OF CONFORMATIONAL TRANSITIONS IN SUPRAMOLECULES AND AMPHIPHILIC BILAYERS

PROEFSCHRIFT

ter verkrijging van
de graad van doctor aan de Universiteit Twente,
op gezag van de rector magnificus,
prof. dr. F.A. van Vught,
volgens besluit van het College voor Promoties
in het openbaar te verdedigen
op donderdag 5 november 2003 om 16.45 uur

door

Tetyana Vitaliyivna Tolpekina

geboren op 3 februari 1975
te Odessa

Dit proefschrift is goedgekeurd door:

de promotor

Prof. dr. W.J. Briels

en de assistenet-promotor

dr. W.K. den Otter

Contents

1 Introduction

1.1 Supramolecules

Supramolecules can be defined as the organized entities that result from the association of two or more molecules held together by intermolecular forces: hydrogen bonding, electrostatic interactions, hydrophobic interactions, coordination bonds and host-guest interactions. The terms ”supramolecule” (1973) and ”supramolecular chemistry” (1978) were introduced by Jean-Marie Lehn, who shared the 1987 Nobel Prize in Chemistry with Charles J. Pedersen and Donald J. Cram for the synthesis of host-guest compounds. Such synthetic systems serve as perfect models for enzymes and other natural biological molecules with host-guest interactions. One example of these synthetic hosts are the calixarenes, utilized in such applications as enzyme mimics, ion carriers and selective complexing agents [68]. Calix[n]arenes are macrocyclic molecules built from 4 to 8 phenol rings linked via methylene units [69], see Fig. 1.1. The name calixarene was suggested by C. David Gutsche as a combination of *calix*, indicating a similarity between the shape of these molecules and a Greek vase (*calix crater*), and *arene*, denoting a compound with aromatic rings [71, 72]. Any hydrogen atom at the upper rim or from the hydroxyl groups at the lower rim in Fig. 1.1 can be replaced by other sidegroups to modify the properties of calixarenes. Such high capability to functionalisation makes calixarenes popular building blocks in supramolecular chemistry.

Calix[4]arenes have four different conformations, distinguished by the orientation of the phenol rings with respect to the central annulus, see Fig. 1.1. The conformation with all phenol rings pointing in the same direction is the “cone” conformation. In this conformation the calix[4]arene has a vase-like shape with a cavity inside and thus can form molecular complexes with smaller molecules. These molecular complexes have been observed by X-ray

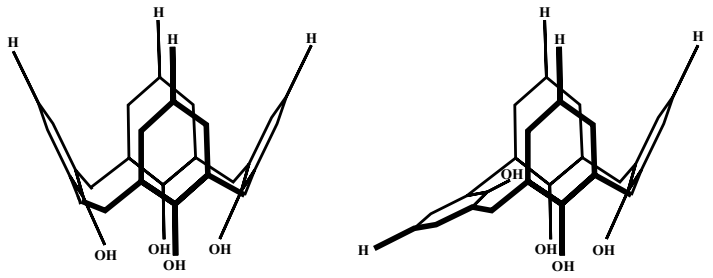

Figure 1.1: Cone (left) and paco (right) conformations of a calix[4]arene.

structure determination and NMR [15, 24, 144]. In the “paco” (short for partial cone) conformation one of the phenol rings is rotated with respect to the other three phenol rings, see Fig. 1.1. There are two conformations in which two phenol rings are oriented in a different direction than the other two phenol rings, namely the “1,2-alternate” with two neighboring rings rotated, and the “ 1,3-alternate” with two opposite rings rotated. When the two remaining phenol rings are also rotated the calix[4]arenes have “inverted cone” conformation. The rates of this cone to inverted cone isomerization for calix[4]arenes with different side groups and in various solvents have been measured with ^{1}H-NMR [10, 70].

1.2 Amphiphilic bilayers as membrane

Membranes are responsible for many important functions of living cells. They serve as a barrier between the interior of a cell and the outside world, and maintain nonequilibrium concentrations of substances in the cytoplasm. Pore formation is the first step of various biological processes such as fusion, cell lysis, and processes related to the transport of ions and small molecules across a membrane. The latter initiated the development of targeted drug delivery and gene therapy. Real biomembranes are complex objects, because - mixed composition proteins. It is more convenient to study the process of pore formation in simpler membranes: amphiphilic bilayers.

Amphiphiles, such as soap molecules or the lipids of biological membranes, consist of a hydrophobic tail and hydrophilic head. This conflicting structure is responsible for the self-assembly of amphiphiles in water into different aggregates to shield the hydrophobic tails

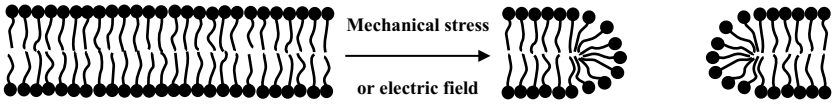

Figure 1.2: Cross-section of an intact bilayer (left) and a bilayer with a pore (right).

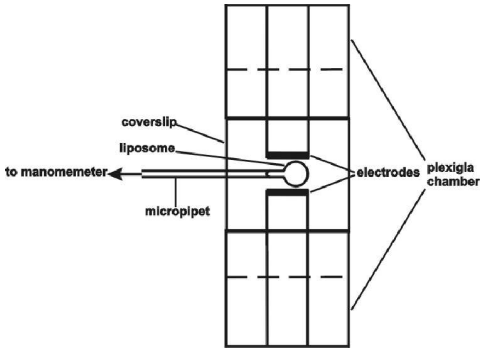

Figure 1.3: Top view of the experimental chamber used by Zhelev and Needham. (Reproduced with permission from [159])

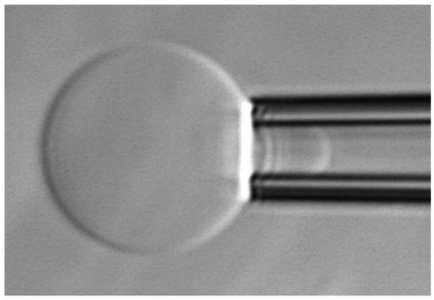

Figure 1.4: Microscope image of a bilayer vesicle aspirated into a micropipette. (Reproduced with permission from [47])

from water: cylindrical or spherical micelles, bilayers and vesicles. In this thesis we consider only amphiphilic bilayers. When the bilayer is exposed to external forces, *e. g.* a mechanical stress or a strong electric field, the bilayer can yield and open up a pore. The process of pore formation is necessarily accompanied by the rearrangement of the amphiphiles which (are going to) constitute the edge of the pore to shield the hydrophobic tails from water, see Fig. 1.2.

Pore formation has been studied experimentally since the 1960's using different techniques: mechanical stress, electroporation, optical illumination, imploding bubbles, adhesion at a substrate, optical tweezers and puncturing by a sharp tip. The experimental study of pores in membranes is complicated due to the short time life of the produced pores: either the pore closes rapidly or the membrane ruptures. Recently developed techniques allow one to extend the time life of a pore. In 1992 D. V. Zhelev and D. Needham presented the first study of long-lived pores in lipid membranes.

Pore formation in a bilayer vesicle was initiated by a single, square, electric pulse. To

prevent the pore from closing, the vesicle was aspirated into a micropipet, see Fig. 1.3 and Fig. 1.4. Thus, by controlling the pipet suction pressure, the surface tension of the membrane was made to balance the line tension of the pore [159]. The time life of the pore was extended to 10μs in this experiment. A second expedient to extend the time life of a pore is to perform the experiment in a highly viscous solvent [123].

1.3 Conformational transitions

This thesis reports on the free energy calculation of conformational transitions in two, it would seem, absolutely different processes. The isomerization of calix[4]arene considered here is the transition of a calix[4]arene molecule from the cone conformation into the paco conformation, and represents the rearrangement of atoms within the molecule, whereas the formation of a pore in an amphiphilic bilayer involves the rearrangement of the molecules within a large molecular assembly. The free energy profiles of the calix[4]arene and the stretched bilayer with a pore are similar, see Figs. 1.5 and 1.6. Both curves have two minima corresponding to their respective stable states: the cone and paco conformations for the calix[4]arene; the intact and the perforated states for the bilayer. The barriers dividing the stable states are 12-15 kcal/mol, depending on the solvent, for the calix[4]arene and 10-20 kcal/mol, depending on the stretching tension, for the bilayer. Thus, both transition processes are activated processes and occur rarely.

The theoretical treatment of activated processe requires the introduction of a reaction coordinate for the process concerned. The free energy profile of this activated processes is then calculated as a function of the reaction coordinate. Usually this concept is applied to chemical reactions with simple reaction coordinates, such as a bond length or a dihedral angle. In this thesis we show that the calculation of a free energy as a function of a reaction coordinate is more general and can be used for quite different activated processes.

1.4 Thesis outline

The main theoretical background of this thesis is statistical mechanics. Hence a concise introduction to statistical mechanics begins *Chapter 2*. This chapter is devoted to the theory

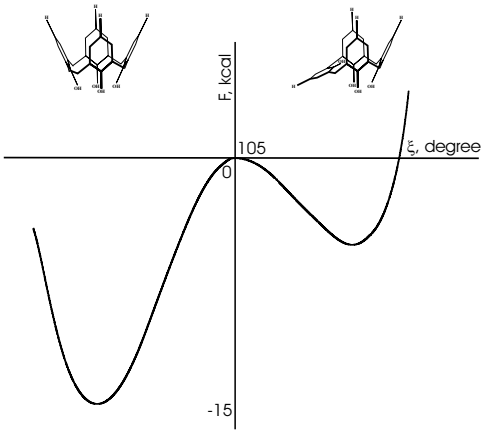

Figure 1.5: Free energy F, as a function of the angle ξ between the central annulus and the rotating phenol ring.

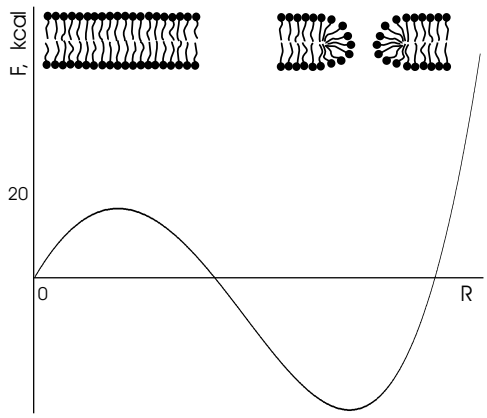

Figure 1.6: Free energy F, as a function of the pore radius R, for a stretched bilayer.

used in the thesis: reaction rate theory, basics of molecular dynamics simulations, methods for free energy calculations and Helfrich's theory of the free energy of a bilayer.

In *Chapter 3* we investigate the influence of solvation on the conformational isomerism of calix[4]arene and *p-tert*-butyl[4]. The free energies of solvation in chloroform and water for different conformations are computed using the quantum mechanical and semiclassical formalisms of the Miertus, Scrocco and Tomasi (MST) model. The results are compared with values calculated by molecular dynamics simulations in the next chapter.

In *Chapter 4* the isomerization reaction of calix[4]arene and *p-tert*-butyl-calix[4]arene in vacuum and in chloroform are studied by molecular dynamics simulations. Three methods are used to obtain the free energy as a function of the reaction coordinate: umbrella sampling for a calix[4]arene in vacuum and in chloroform and a *p-tert*-butyl-calix[4]arene in a vacuum; window sampling and a combined coupling parameter-umbrella sampling approach for a *p-tert*-butyl-calix[4]arene in chloroform. The conformational inversion rates are calculated by the reactive flux method and compared with experimental values.

In *Chapter 5* we study pore formation in an amphiphilic bilayer, simulated by a coarse-grained model. The free energy as a function of the reaction coordinate is calculated by the thermodynamic integration method from data sampled with molecular dynamics simulations

with a constrained reaction coordinate. We consider three cases: an unstretched bilayer and bilayers with small (3.5%) and large (25%) relative elongations. To compare the results with the macroscopic approach described in the next chapter, we convert the free energy as a function of the computationally convenient reaction coordinate into the free energy as a function of the pore radius.

In *Chapter 6* we present simulations of a punctured amphiphilic bilayer under various tensions, with a coarse-grained model. We propose a simple expression for the free energy of a square bilayer containing a circular pore. The line tension coefficient is calculated by three different approaches.

At the end of the thesis, the results are summarized in both English and Dutch.

2 Theory

2.1 Statistical Mechanics

Statistical mechanics relates the physical properties of a macroscopic system to the microscopic properties of the atoms or molecules (particles) constituting this system. Due to the tremendous number of particles in a macroscopic system, Statistical mechanics considers the physical properties of a macroscopic system as an ensemble average by using statistics of the microscopic states.

A microscopic state of a system consisting of N particles is described by a set coordinates $\mathbf{r}_1$, $\mathbf{r}_2$, ..., $\mathbf{r}_N \equiv r^{3N}$ and momenta $\mathbf{p}_1$, $\mathbf{p}_2$, ..., $\mathbf{p}_N \equiv p^{3N}$, and is represented by a point in phase space. The microscopic state is a possible realization of a macroscopic system. The collection of all independent realizations of a macroscopic system is called an ensemble. Here we consider the canonical ensemble, regarding a system of N identical particles in a volume V at an absolute temperature T. The probability to find this system in the volume element $dr^{3N}dp^{3N}$ centered at the point $r^{3N}p^{3N}$ phase space is given by the Boltzmann distribution,

$$\rho(r^{3N}, p^{3N})dr^{3N}dp^{3N} = \frac{1}{Q}\frac{1}{h^{3N}N!}\exp\big[-\beta H(r^{3N}, p^{3N})\big]dr^{3N}dp^{3N}, \tag{2.1}$$

where $\beta = 1/k_BT$, k_B is Boltzmann's constant, h is Planck's constant and H is the Hamiltonian, which determines the energy of the system as a function of its coordinates and momenta. The factor $1/N!$ accounts for the indistinguishability of the particles, and $1/h^{3N}$ connects the classical mechanical and quantum mechanical distributions. The partition function Q is used to normalize the distribution,

$$Q = \frac{1}{h^{3N}N!}\int \exp\big[-\beta H(r^{3N}, p^{3N})\big]dr^{3N}dp^{3N}. \tag{2.2}$$

The measured value of a macroscopic property F equals the ensemble average, being the expectation value of the associated microscopic property f over the microscopic realizations:

$$F = \langle f \rangle = \frac{1}{Q} \frac{1}{h^{3N} N!} \int f(r^{3N}, p^{3N}) \exp\left[-\beta H(r^{3N}, p^{3N}) \right] dr^{3N} dp^{3N}. \tag{2.3}$$

This integral is generally impossible to calculate analytically. In molecular dynamics simulations the calculation of the macroscopic property F is founded on the ergodic hypothesis [101], which states that the ensemble average is equal to the average over time, see Section 2.4,

$$\langle f \rangle = \overline{f}, \tag{2.4}$$

where the time average is,

$$\overline{f} = \lim_{T \to \infty} \frac{1}{T} \int_0^T f[r^{3N}(t), p^{3N}(t)] dt. \tag{2.5}$$

In other words, the dynamical evolution of a system for a sufficiently long period of time serves as a representative sample of all possible realization.

At short (in a macroscopic sense) times the behavior of a system is well described by the famous Onsager regression hypothesis [111, 112], which states that slow microscopic fluctuations of f around equilibrium on average decay according to macroscopic laws:

$$\langle \Delta f(t) \Delta f(0) \rangle = \langle (\Delta f(0))^2 \rangle \phi(t), \tag{2.6}$$

$\phi(t)$ is not just any function, but describes the dynamics of F, $F(t) = F(0)\phi(t)$, provided the value of $F(0)$ is small enough to lie in the linear regime. On the left hand side of this equation we encounter a time correlation function,

$$\langle f(t) g(0) \rangle = \int \rho\left(r^{3N}, p^{3N}, 0\right) f\left(r^{3N}, p^{3N}, t\right) g\left(r^{3N}, p^{3N}, 0\right) dr^{3N} dp^{3N}. \tag{2.7}$$

From this definition and time independence of ρ follows the property

$$\langle f(t+\tau) g(\tau) \rangle = \langle f(t) g(0) \rangle. \tag{2.8}$$

After differentiating Eq. (2.8) with respect to τ and substituting $\tau = 0$, an other property of the correlation function is obtained:

$$\langle \dot{f}(t) g(0) \rangle = -\langle f(t) \dot{g}(0) \rangle. \tag{2.9}$$

Here and below a dot represents the derivative with respect to time.

2.2 Reaction rate theory

The isomerization of calix[4]arene and *p-tert*-butyl-calix[4]arene studied in this thesis is the reversible unimolecular reaction between reactants R and products P:

$$R \underset{k_r}{\overset{k_f}{\rightleftarrows}} P. \tag{2.10}$$

This reaction is a bi-continuous process: reactants is turned into products, while simultaneously a fraction of the products is turned into reactants. The mass conservation law for this reaction reads as

$$R + P = 1. \tag{2.11}$$

The conversions per unit of time are described by phenomenological equations for the population dynamics:

$$\dot{R} = -k_f R + k_r P, \tag{2.12}$$

$$\dot{P} = k_f R - k_r P, \tag{2.13}$$

where k_f and k_r are the rate constants of the forward and reverse reactions respectively. By definition, the equilibrium constant of the reaction is the ratio of the rate constants $K = k_r/k_f$. At equilibrium the left sides of Eqs. (2.12) and (2.13) equal zero and the equilibrium constant can be expressed as the ratio of the equilibrium fractions,

$$K = \frac{R_{eq}}{P_{eq}}. \tag{2.14}$$

Consider the deviation from equilibrium $\Delta P(t) = P(t) - P_{eq}$. Combining Eqs. (2.13) and (2.14), the relaxation of this deviation is given by

$$\Delta P(t) = \Delta P(0) \exp(-\lambda t), \tag{2.15}$$

where $\lambda = k_f + k_r$ is the relaxation rate. Using Eq. (2.14) we can express the forward reaction rate as

$$k_f = \lambda P_{eq}. \tag{2.16}$$

The calculation of the forward reaction rate k_f directly from Eq. (2.16) in a molecular dynamics simulation is not possible for reactions with a high activation barrier, like the isomerization

of a calix[4]arene, because the relaxation to equilibrium is too slow. Below we discuss the calculation method of the reaction rate for such reactions.

2.2.1 Reactive flux method

In this thesis we restrict ourselves to reactions in systems with a low concentration of reacting solute. In this case the reacting molecules do not interact with each other. Since the molecules behave identically, it suffices to consider a single molecule.

We begin the microscopic consideration of the reaction with the introduction of a parameter that separates products and reactants. Such a parameter is the reaction coordinate ξ, defined such that it is positive for products and negative for reactants. So, reactants and products are divided by the transition state plane $\xi = \xi^{\neq}$, which is located in the thinly populated area near the top of the energy barrier, separating reactants and products. The reaction coordinate ξ is usually chosen to be a function of the coordinates of the reacting molecule only [11, 29]. The probability for a molecule to be in the product state is obtained by summing over all realizations that classify as a product,

$$\langle p \rangle = \frac{1}{Q}\frac{h^{-3N}}{N!}\int \Theta[\xi(\Gamma^N)]\exp[-\beta H(\Gamma^N)]d\Gamma^N = \langle \Theta(\xi)\rangle, \tag{2.17}$$

where Θ is the Heaviside step function. The probability for a molecule to be in the reactant state is given by Eq. (2.17) with ξ replaced by $-\xi$. According to Onsager regression hypothesis, Eq. (2.6), the average decay of a spontaneous deviation from equilibrium is given as

$$\frac{\langle \Delta\Theta[\xi(t)]\Delta\Theta[\xi(0)]\rangle}{\langle(\Delta\Theta[\xi(0)])^2\rangle} = \exp(-\lambda t), \tag{2.18}$$

where $\exp(-\lambda t)$ is the macroscopic response from Eq. (2.15). Differentiating Eq. (2.18) with respect to time we arrive at

$$\frac{\langle \Delta\dot{\Theta}[\xi(t)]\Delta\Theta[\xi(0)]\rangle}{\langle(\Delta\Theta[\xi(0)])^2\rangle} = -\lambda\exp(-\lambda t). \tag{2.19}$$

As mentioned above, the time interval interesting for simulations is $\tau_v \ll t \ll \lambda^{-1}$, where τ_v is a molecular vibrations time. On this time interval Eq. (2.19) can be rewritten with the help of Eq. (2.9) as

$$\frac{\langle \Theta[\xi(t)]\dot{\xi}(0)\delta[\xi(0)]\rangle}{\langle(\Delta\Theta[\xi(0)])^2\rangle} = \lambda, \tag{2.20}$$

where $\delta(\xi)$ is the Dirac delta function arising from differentiation of the Heaviside function. Combining Eqs. (2.16) and (2.20), and using $\langle \Delta\Theta^2 \rangle = \langle \Theta^2 \rangle - \langle \Theta \rangle^2 = \langle p \rangle \langle r \rangle$, we obtain the forward reaction rate

$$k_f^{RF}(t) = \frac{\langle \delta[\xi(0)]\dot{\xi}(0)\Theta[\xi(t)] \rangle}{\langle \Theta[-\xi(0)] \rangle}. \tag{2.21}$$

The numerator of Eq. (2.21) equals the Boltzmann weighted average velocity of molecules that cross the transition state at time zero and are found in the product state at time t: the reactive flux. The denominator is just the equilibrium fraction of reactants. So the forward reaction rate is given by the reactive flux (RF) theory as the ratio of the reactive flux of molecules to the population of the reactant.

2.2.2 Transition state theory and transmission coefficient

The Eyring's transition state theory (TST) expression [51] of reaction rate k^{TST} can be obtained from Eq. (2.21) in the limit of time t going to zero. In TST the reaction rate depends on the flux of molecules crossing the transition state in the forward direction at time zero:

$$k_f^{TST}(t) = \frac{\langle \delta[\xi(0)]\dot{\xi}(0)\Theta[\dot{\xi}(0)] \rangle}{\langle \Theta[-\xi(0)] \rangle}. \tag{2.22}$$

Transition state theory gives an over-estimated value as compared to the true reaction rate, because TST is based on the assumption that every reactant crossing the transition state will end up as a product and does not take into account the possibility of rapid re-crossings [51]. As a compensation, the RF theory introduces a transmission coefficient, whose value lies between zero and one [29, 74],

$$k_f^{RF} = \kappa k_f^{TST}. \tag{2.23}$$

Substitution of Eqs. (2.21) and (2.22) in Eq. (2.23) gives the expression for the transmission coefficient κ,

$$\kappa(t) = \frac{\langle \delta[\xi(0)]\dot{\xi}(0)\Theta[\xi(t)] \rangle}{\langle \delta[\xi(0)]\dot{\xi}(0)\Theta[\dot{\xi}(0)] \rangle}. \tag{2.24}$$

The numerator of Eq. (2.24) is the reactive flux. For very short times both fluxes are almost the same and $\kappa = 1$. Due to re-crossings the reactive flux, and therefore the transmission

coefficient, reduces in time. If the energy barrier is high, and the energy transfer to the solvent is efficient, then only those molecules that are still near the transition state are capable of recrossing. Once the molecule has reached the reactant or product state, and its excess energy has been dissipated by the solvent, it will only recross on a time scale associated with the reaction rate itself. This suggests that $\kappa(t)$ shows rapid transient decay from a value of one to a plateau value $\kappa_{plateau}$ in the time interval $0 \leq t \ll \lambda^{-1}$ and exponential decay at time scales of the order of $1/\lambda$. The true reaction rate in Eq. (2.23) is calculated with $\kappa_{plateau}$,

$$k_f^{RF} = \kappa_{plateau} k_f^{TST}. \tag{2.25}$$

Clearly, the transmission coefficient can be calculated from short MD simulations, with starting configuration sample from the transition state. The TST rate can be expressed as

$$k^{TST} = \frac{\langle \dot{\xi}(0)\delta[\xi(0)]\Theta[\xi(0)]\rangle}{\langle \delta[\xi(0)]\rangle} \frac{\langle \delta[\xi(0)]\rangle}{\langle \Theta[\xi(0)]\rangle}, \tag{2.26}$$

where the first fraction is the readily established average velocity of molecules crossing the transition state. The second fraction denotes the probability for a reactant to reach the transition state, which forms the major bottle neck in MD studies of reactions. In Section 2.6 we discuss several approaches to calculate the probability distribution $P(\xi)$, or free energy function

$$A(\xi) = -kT \ln P(\xi). \tag{2.27}$$

2.3 Free energy of a membrane

Just like the above introduced free energy describes the probability distribution of the reaction coordinate, irrespective of the other coordinates, Helfrich's theory [78] for the free energy of a bilayer gives the probability to find a bilayer with a certain global shape, without considering the positions of all atoms constituting the bilayer. In this model the shape of the membrane is assumed to vary smoothly along the membrane. The local shape of the membrane surface can be characterized by the principal curvatures k_1 and k_2 or by the mean curvature $H = (k_1 + k_2)/2$ and the Gaussian curvature $K = k_1 k_2$ [84]. Taking also into account uniformly distributed stretch or compression, the expression for the free energy of a membrane takes

the form [42, 78, 122, 133]

$$F = \int \{2\kappa(H - c_0)^2 + \bar{\kappa}K\}da + \frac{1}{2}K_A A_0 \left(\frac{A - A_0}{A_0}\right)^2, \tag{2.28}$$

The spontaneous curvature $c_0$is the curvature energy per unit area of a flat membrane ($k_1 = k_2 = 0$) and reflects the tendency of a flat membrane to bend due to non-vanishing internal stresses. For the bilayer studied in *Chapters 5 and 6*, the spontaneous curvature vanishes. The bending modulus κ measures the curvature energy caused by the deviation from the spontaneous curvature. The saddle-splay modulus $\bar{\kappa}$ relates to saddle-like deformations. K_A is the compressibility modulus, and A_0 and A are the equilibrium and actual surface area respectively.

In *Chapter 5 and 6* we extend the model by introducing a term describing the edge energy of a pore. The radius of the pore will then serve as the reaction coordinate.

2.4 Molecular Dynamics Simulations

Molecular Dynamics (MD) simulations [8, 56] reproduce the dynamical evolution of a system at a molecular (atomic) level by using classical mechanics (or quantum mechanics, if it is necessary). Such an approach allows us to obtain not only statistical averages (see Section 2.1) but also dynamical properties of the system (see Eq. (2.24)). In that way, MD serves as an experiment of mechanical statistics.

Consider a system consisting of N atoms. The position of atom i with mass m_i at each moment of time t is described by a radius vector $\mathbf{r}_i(t)$. The motion of atom i is determined by the Newton's equations of motion,

$$m_i \ddot{\mathbf{r}}_i = \mathbf{f}_i, \tag{2.29}$$

$$\mathbf{f}_i = -\nabla_i \Phi(\mathbf{r}^N), \tag{2.30}$$

where $\mathbf{f}_i$ is the force acting on the atom i and $\Phi(\mathbf{r}^N)$ is the potential energy function. We consider potential energy functions in more detail Section 2.5.

The system of N coupled differential Eqs. (2.29) and (2.30) can be solved numerically. One of the methods to integrate this system step by step is the leap-frog Verlet algorithm. This method is based on a Taylor expansion of the position $\mathbf{r}_i$ at time $t_n = t_0 + n\Delta t$. For sufficiently

small time step Δt,

$$\mathbf{r}_i(t_n \pm \Delta t) = \mathbf{r}_i(t_n) \pm \dot{\mathbf{r}}_i(t_n)\Delta t + \frac{1}{2}\ddot{\mathbf{r}}_i(t_n)\Delta t^2 \pm \frac{1}{6}\dddot{\mathbf{r}}_i(t_n)\Delta t^3 + o(\Delta t^4). \tag{2.31}$$

The recursion relation between the velocity at the former and the new step reads as:

$$\mathbf{v}_i\left(t_n + \frac{\Delta t}{2}\right) = \mathbf{v}_i\left(t_n - \frac{\Delta t}{2}\right) - \frac{\Delta t}{m_i}\nabla_i \Phi(\mathbf{r}^N(t_n)) + o(\Delta t^3), \tag{2.32}$$

subject to Eqs. (2.29)and (2.30). The recursion relation for the coordinates is given by:

$$\mathbf{r}_i(t_n + \Delta t) = \mathbf{r}_i(t_n) + \mathbf{v}_i\left(t_n + \frac{\Delta t}{2}\right)\Delta t + o(\Delta t^4). \tag{2.33}$$

One of the most important parameters of any simulation is the time step. Increasing the time step accelerates the sampling of the system, but the numerical accuracy of the integration algorithm sets an upper limit to the step size. The common way to increase the time step of a simulation is to fixate intramolecular bond lengths. This is possible because the high-frequency vibrations of these bonds have almost no influence on the other motions in the system. Constraining the bond length $\sigma = |\mathbf{r}_{ij}|$ between two atoms i and j to the constant value σ^* gives rise to an extra force in Newton's equation of motion for atoms i,

$$m_i\ddot{\mathbf{r}}_i(t) = \mathbf{f}_i(t) + \lambda_\sigma(t)\vec{\nabla}_i\sigma(t), \tag{2.34}$$

where λ_σ is the Lagrange multiplier chosen such that the constraint is satisfied at every moment. The new position of atom i j after one time step Δt according to the Verlet algorithm and Eq. (2.34) reads

$$\mathbf{r}_i(t + \Delta t) = \mathbf{r}_i^{'}(t + \Delta t) + \frac{\Delta t^2}{m_i}\lambda_\sigma(t)\vec{\nabla}_i\sigma(t), \tag{2.35}$$

where the prime denotes the position of atom i at time $t + \Delta t$ in the absence of the constraint. The Lagrange multiplier is found by solving $|\mathbf{r}_{ij}(t + \Delta)| = \sigma^*$ to first order, and iterating this step till the desired accuracy is reached. For a system of many constraints, this procedure is iterated over all constraints until all constraints are obeyed simultaneously. This calculation scheme for constraining bond lengths constraining was proposed by Ryckaert *et al.*and is known as the SHAKE algorithm [121]. In Section 2.6.1 and *Chapters 5 and 6* the constraint of the reaction coordinate will be performed in the same way.

2.5 Potential

The execution of an MD simulation requires knowing the potential energy of a system as a function of the coordinates, $\Phi(\mathbf{r}^N)$. In most cases the potential energy is introduced by an empirical function. This function incorporates potentials for intramolecular interactions — bond stretching, angle bending, o-o-p bending (improper dihedral) out of plane bending, torsional rotation (dihedral) and Urey-Bradley for 1-3 interactions — and for intermolecular interactions — Lennard-Jones for Van der Waals interactions and Coulombic for electrostatic interactions

$$\begin{aligned}\Phi_{\mathtt{em}}(\mathbf{r}^N) = &\frac{1}{2}\sum_{i=1}^{\mathtt{bonds}} k_i^b(b_i-b_i^0)^2 + \frac{1}{2}\sum_{i=1}^{\mathtt{angles}} k_i^\theta(\theta_i-\theta_i^0)^2 + \frac{1}{2}\sum_{i=1}^{\mathtt{impropers}} k_i^w(w_i-w_i^0)^2 \\ &+ \sum_{i=1}^{\mathtt{dihedrals}} k_i^\phi\{1+\cos(n\phi_i-\delta_i)\} + \frac{1}{2}\sum_{i=1}^{\mathtt{Urey-\ Bradley}} k_i^{UB}(u_i-u_i^0)^2 \\ &+ \sum_{j>i}^{N}\left[4\varepsilon_{ij}\left\{\left(\frac{\sigma_{ij}}{r_{ij}}\right)^{12} - \left(\frac{\sigma_{ij}}{r_{ij}}\right)^{6}\right\} + \frac{q_i q_j}{4\pi\varepsilon_0 r_{ij}}\right].\end{aligned} \tag{2.36}$$

The coefficients and parameters can be determined by quantum chemical calculations combined with vibration spectra, thermophysical and phase coexistence data.

The empirical potential is not suitable for studying the solvent effect in case of a strong self-polarization between the solute and the solvent. One alternative is a combined quantum mechanical/molecular mechanical method (QM/MM). In this method the solute is treated quantum mechanically and the explicit solvent molecules are simulated by using the empirical potential ($\Phi_{\mathtt{em}}$) Eq. (2.36),

$$\Phi_{\mathtt{pot}} = \Phi_{\mathtt{QM}} + \Phi_{\mathtt{em}} + \Phi_{\mathtt{QM/MM}}. \tag{2.37}$$

where the potential $\Phi_{\mathtt{QM/MM}}$ couples the two regions. The potential energy $\Phi_{\mathtt{QM}}$ is calculated from the time-independent Schrödinger equation with a Hamiltonian,

$$\widehat{H} = -\frac{\hbar^2}{2m}\Delta + \Phi(x,y,z), \tag{2.38}$$

where the first term on the right hand side is an operator associated with the kinetic energy and the second term gives the potential energy for the electron interactions. An other alternative is the supermolecule approach, in which the solute and a few solvent molecules are treated quantum mechanically, one may even study dynamics of the system fully quantum mechanical *e. g.* by using the method of Carr and Parrinello [27].

2.6 Free energy calculation

The calculation of free energies is an essential task for the physical description of activated processes. It provides information on the locations and populations of the stable states and the transition states, and hence on the transition rates. Reaction rate theory introduces a convenient way for the theoretical treatment of an activated processes via the reaction coordinate ξ, see Section 2.2. Consequently, the free energy is calculated here as a function of the reaction coordinate.

This free energy is determined as

$$A(\xi) = -k_B T \ln Q(\xi), \tag{2.39}$$

where the partition function $Q(\xi)$ reads

$$Q(\xi) = \int \delta[\xi(r^{3N}) - \xi^*] \exp\left[-\beta H(r^{3N}, p^{3N})\right] dr^{3N} dp^{3N}. \tag{2.40}$$

So the free energy function $A(\xi)$ can be obtained by making a probability distribution of ξ for a system that is free to sample the entire range of the reaction coordinate. But it is extremely inefficient to do so for a system with a high energy barrier (as studied in this thesis) because the system spends most of its time in the stable states and the barrier region will be sampled very poorly. The two methods described below are applied in this thesis in order to eliminate this sampling problem.

2.6.1 Potential of mean constraint force

The main idea of the potentail of mean constraint force method(PMCF) is to apply a constrain to the reaction coordinate. On the one hand, the system is thus forced to sample the entire range of the reaction coordinate. On the other hand, one intuitively feels that the constrain force is closely related to the derivative of the free energy. This insight by van Gunsteren [146] was put on a firmer footing by Mülders, Schlitter *et al.* [106], and was eventually proven by den Otter and Briels [38] of the various re-derivations and extensions presented in the literature [34, 40, 41, 134]. We follow that of Schlitter and Klähn [126] here.

The partition function of a reaction coordinate constrained system is:

$$Q_c(\xi) = \int \exp\left[-\beta H_c(\xi, q^{3N-1}, p_q^{3N-1})\right] dq^{3N-1} dp_q^{3N-1}, \tag{2.41}$$

$$A_c(r) = -k_B T \ln Q_c(\xi), \tag{2.42}$$

where q^{3N-1} denotes the unconstrained coordinates, p_q^{3N-1} are their canonical momenta, and $H_c(\xi, q^{3N-1}, p_q^{3N-1})$ is the Hamiltonian of the constrained system. From the Eqs. (2.39) and (2.42), the free energy change of an unconstrained system dA/dr is given by

$$\frac{dA}{dr} = \frac{dA_c}{dr} - k_B T \frac{d}{dr} \ln \frac{Q(r)}{Q_c(r)}. \tag{2.43}$$

The first term on the right hand side of Eq. (2.43) is the free energy derivative of the constrained system; it equals the ensemble average of the constraint force in the constrained ensemble [106]:

$$\frac{dA_c}{dr} = \langle \lambda_\xi \rangle_c, \tag{2.44}$$

where λ_ξ is the previously introduced Lagrange multiplier of the constraint force. The correction term in Eq. (2.43) stems from the integral over the conjugate moment to ξ, which is implicit in Q but excluded in Q_c because $\dot{xi} = 0$ in the constrained ensemble. As Schlitter and Klähn [126] showed,

$$\frac{Q(r)}{Q_c(r)} = const \times \langle z^{-1/2} \rangle_c, \tag{2.45}$$

where z is the metric tensor

$$z = \sum_i \frac{1}{m_i} \left(\frac{\partial \xi}{\partial \mathbf{r}_i} \right)^2. \tag{2.46}$$

Integrating Eq. (2.43) after substituting Eqs. (2.44) and (2.45), the free energy can be rewritten as

$$A(\xi) = \int \langle \lambda_\xi \rangle_c \, d\xi - k_B T \ln \langle z^{-1/2} \rangle_c. \tag{2.47}$$

Thus the free energy as a function of the reaction coordinate can be calculated from MD simulations performed with a constrained reaction coordinate according to Eq. (2.47).

2.6.2 Umbrella sampling method

The umbrella sampling method is based on the notation that a reduction of the free energy differences between the stable conformations and the transition state improves the sampling

of the reaction coordinate. This is achieved by adding an "umbrella" potential $U(r^{3N})$ to the existing potential energy of the system. The probability distribution of the system with the umbrella potential reads

$$P_U(\xi) = \frac{1}{Q_U} \frac{h^{-3N}}{N!} \int\int \delta[\xi(r^{3N}) - \xi^*] \exp\left[-\beta\{H(r^{3N}, p^{3N}) + U(r^{3N})\}\right] dr^{3N}\, dp^{3N}. \quad (2.48)$$

In case the umbrella potential is a function of the reaction coordinate only, the distribution in the biased run is easily converted into the probability distribution of the unbiased run,

$$P(\xi) = const \times P_U(\xi) \exp[\beta U(\xi)], \quad (2.49)$$

where *const* is an irrelevant proportionality constant. The particular choice $U(\xi) = -A(\xi)$ would make P_U a constant, independent of ξ. To calculate the free energy $A(\xi)$, long simulation with a trial umbrella potential U_0 is performed. Then the sampled probability distribution is converted into a potential U_1 according to

$$U_1(\xi) = -k_B T \ln P(\xi). \quad (2.50)$$

The new trial umbrella potential $U_0 + U_1$ is used for a second simulation and so on, until the probability distribution is reasonably flat. The umbrella potential of the run with the flat distribution gives the free energy as a function of the reaction coordinate.

3 Impact of the solvent on the conformational isomerism of calix[4]arenes: a study based on continuum solvation models

The influence of solvation on the conformational isomerism of calix[4]arene and p-tert-butyl-calix[4]arene has been investigated by using the continuum model reported by Miertus, Scrocco and Tomasi (MST). The quantum mechanical (QM) and semiclassical (SC) formalisms of the MST model have been considered for two different solvents (chloroform and water). The suitability of the QM-MST and SC-MST methods has been examined by comparison with previous results derived from classical molecular dynamics (MD) simulations with explicit solvent molecules. The application of the continuum model to the solute configurations generated by using in vacuo classical MD simulations provides a fast strategy to evaluate the effects of the solvent on the conformational preferences of calixarenes. These encouraging results allow us to propose the use of continuum models to solutes with complex molecular structures, which are traditionally studied by MD simulations. *

3.1 Introduction

An understanding of many chemical process cannot be achieved without an accurate description of the solvent effects [114, 119, 149]. In the past decades, this realization has led to the development of a wide variety of computational methods, which are able to describe the effects of the solvent on molecular energies, structures and properties. Such

∗ The work described in this chapter previously appeared in J. Org. Chem. **69**, 951 (2004) [4].

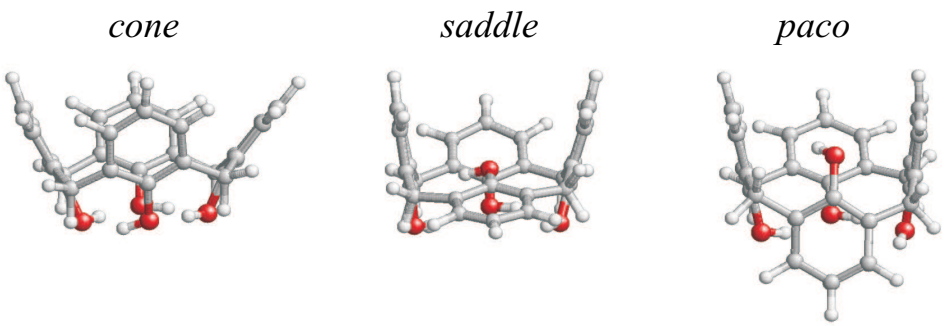

Figure 3.1: Atomistic representation of the cone, saddle and paco conformations for **1**.

methods can broadly be classified into two different categories: discrete and continuum [31, 59, 83, 114, 143, 148]. The discrete model considers explicitly the microscopic representation of the solvent molecules. This model is rigorous and accurate results can be expected, although serious shortcomings derived from its computational expensiveness exist. In practice, the solvated system is usually described according to one of the following three approaches [59, 83, 114, 148]: a) supermolecule approach (the solute and the solvent are treated quantum mechanically and, therefore, only a few molecules can be explicitly included to mimic the whole environment surrounding the solute), (b) quantum mechanics/molecular mechanics (QM/MM) approach (the solute is treated quantum mechanically and the explicit solvent molecules are simulated using a classical force-field), (c) molecular mechanics (MM) approach (both the solute and the solvent are described by means of classical particles).

The accuracy of the results produced by each approach depends on several factors as the size of the solute, the number of solvent molecules considered, the magnitude of the contribution due to the self-polarization between the solute and the solvent, the goodness of the fixed classical potentials, etc.

In the continuum model the solvent is represented as a structureless polarizable medium characterized by properties such as the dielectric constant and the thermal expansion coefficient [31, 114, 143]. The macroscopic continuum medium reacts against the solute charge distribution, generating a reaction field that in turn affects the solute charge distribution. Thus, the self-polarization between the solute and the solvent is accounted for properly by using QM methods. The continuum model has the obvious shortcoming that short-range interactions be-

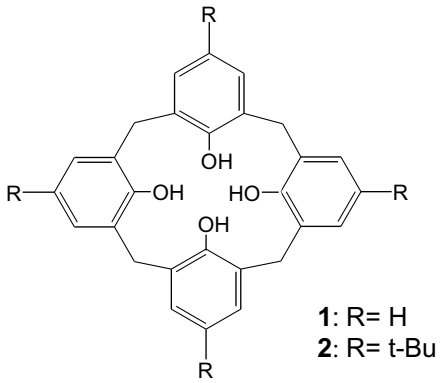

Figure 3.2: Schema

tween solute and solvent are not well represented. This deficiency is partially removed by the combined continuum/discrete strategy [2, 3, 28, 30], in which the solute is surrounded by an appropriate number of explicit solvent molecules, and then this cluster, as a unique entity, is inserted in the continuum medium.

Complex organic molecules are the subject of intensive investigations in the field of supramolecular chemistry. Among them, calixarenes have received considerable attention because these compounds are able to bind a variety of guests [81, 153]. Calixarenes are synthetic macrocyclic molecules built from phenolic units. The simplest representative of these macrocycles is the calix[4]arene (**1**), which only involves four phenol rings (Figure 3.2). Many other compounds have been prepared by introducing selective chemical modifications, the more common being at the phenolic hydroxy group, the para-position of the rings, and the methylene bridges [18, 87, 116, 132].

The conformational flexibility of **1** and its derivatives mainly arises from an oxygen-through-the-annulus rotation mechanism. The most relevant conformations are those denoted cone and partial-cone (paco), which differ in the orientation of one phenol ring with respect to the other three (Figure 3.1). NMR spectroscopy results indicated that, in some cases, the dynamic equilibrium between the cone and paco conformations is profoundly influenced by the polarity of the solvent [26, 81, 82, 132, 145]. This conformational isomerism has been investigated by using theoretical methods in which the solvent is either neglected [17, 53, 132, 145] or described using a discrete model through the MM approach [36, 39, 65, 142, 150],

the rates calculated with the latter method for the isomerization of calix[4]arene being in excellent agreement with experimental data [36, 39, 142].

As far as we know, the continuum model has not previously been used to investigate the role of the solvent in the cone-to-paco conformational transition. This is an amazing situation since the application of this model to medium size molecules such as calix[4]arenes is computationally less expensive than the simulation of a periodic box containing many discrete solvent molecules. It should be noted that the inclusion of explicit solvent molecules implies that many configurations must be generated using molecular dynamics (MD) or Monte Carlo (MC) simulations to obtain a statistical treatment of the intermolecular interactions. Furthermore, the continuum model has successfully been employed to study the binding properties of calix[4]pyrrole [21, 156], a closely related compound with pyrrole rings rather than phenolic units, indicating that it provides a good description of molecules with complex architectures in solution.

The aim of this work is to investigate the isomerization of calixarenes by using the continuum model. For this purpose, the MST model [12, 93, 96, 113, 114], which is an optimized version of the method developed by Miertus, Scrocco and Tomasi [103, 104, 143], has been used to explore the role of the solvent in the cone-to-paco transition of **1** and p-tert-butylcalix[4]arene (**2**). Calculations have been performed considering the polarization effects within the QM and semiclassical (SC) frameworks of the MST model. Thus, a comparison between the results derived from QM-MST and SC-MST calculations will be valuable to check the reliability of the latter method when complex organic molecules are considered. Particular attention has been paid to the parametrization of the charges in SC-MST calculations. Furthermore, we have also studied the influence of the polarity of the environment by considering both chloroform and water as solvents.

3.2 Methodology and Technical Details

3.2.1 Generation of the Conformations

Three different conformational states (Figure 3.1) were considered for **1** and **2**: (i) the cone; (ii) the paco; and (iii) the saddle point, which corresponds to the transition state of the cone-to-paco transformation. It should be noted that thermal motion provides a certain degree

of conformational freedom to such states. Accordingly, 100 configurations were generated for each conformational state through MD simulations with classical potentials. The force-field parameters for **1** and **2** were identical with those used in refs 12 and 13a. Simulations were performed in vacuo at 300 K, no cutoff being used for the nonbonding interactions. Configurations of the saddle point were generated using constrained MD simulations. All calculations were performed with the GROMOS87 [16] and *DL_POLY* _2.0 [130] computer packages.

3.2.2 The MST Continuum Model

In the MST model, the solute is placed inside a molecular shape cavity embedded in the infinite dielectric medium. The free energy of solvation (ΔG_{sol}) is estimated from the addition of the electrostatic, cavitation and van der Waals contributions [12, 93, 96, 113].

$$\Delta G_{sol} = \Delta G_{ele} + \Delta G_{cav} + \Delta G_{vdW} \tag{3.1}$$

The cavitation term has been computed using Pierotti scaled particle theory [118] adapted to molecular-shaped solutes [12, 93, 96, 113, 114]. In Eq. (3.2), $\Delta G_{P,i}$ is the cavitation free energy of atom i in Pierotti's formalism, S_i is the solvent-exposed surface of atom i, S_T is the total solvent-exposed surface of the molecule and N is the number of atoms.

$$\Delta G_{cav} = \sum_{i=1}^{N} \frac{S_i}{S_T} \Delta G_{P,i} \tag{3.2}$$

The van der Waals term has been evaluated by means of an empirically developed [12, 93, 96, 113] linear relation with the molecular surface area,

$$\Delta G_{vdW} = \sum_{i=1}^{N} \xi_i S_i \tag{3.3}$$

where ξ is the surface parameter of atom i. Specific surface parameters have been derived for different solvents [12, 33, 93, 96, 113].

The electrostatic interaction between the solute and the solvent has been calculated by using the procedure originally developed by Tomasi and co-workers [103, 104, 143]. Accordingly, the polarization of the dielectric by the solute charge distribution induces a reaction field, whose effect on the solute charge distribution is accounted for by a perturbation

operator $\widehat{V}_R$ added to the gas-phase Hamiltonian in vacuo, $\widehat{H}^0$:

$$\widehat{H} = \widehat{H}^0 + \widehat{V}_R \tag{3.4}$$

The perturbation operator is described in terms of a set of imaginary charges spread over the solute cavity (Eq. (3.5)), which are obtained by solving the Laplace equation with suitable boundary conditions (Eq. (3.6)). In Eq. (3.5), M is the total number of surface elements in which the solute/solvent boundary is divided, and $\{q_j\}$ is the set of charges (located at r_j) that represent the solvent response. In Eq. (3.6), ε is the solvent dielectric constant, V_T stands for the total (solute+solvent) electrostatic potential, and n is the unit vector normal to the surface element j. From these charges, the ΔG_{ele} can be obtained by using a QM or SC formalism.

$$\widehat{V}_R = \sum_{i=1}^{M} \frac{q_i}{|r_i - r|} \tag{3.5}$$

$$q_j = -\frac{\varepsilon - 1}{4\pi\varepsilon} S_j \left(\frac{\partial V_T}{\partial n} \right)_j \tag{3.6}$$

Choice of the solute/solvent interface is very important to provide reliable values of the electrostatic contribution. In the MST method the solvent-exposed surface, which is obtained upon an appropriate scaling of the atomic radii, is used to define the solute/solvent boundary. To avoid the presence of regions of dielectric medium that are too thin to accommodate a real solvent molecule, the scaling factor (κ) was specifically derived for each solvent. MC simulation indicated that the best values of κ for chloroform and water are 1.6 and 1.2 [12, 93, 96, 113], respectively, which were used throughout the study.

3.2.3 Quantum Mechanical Formalism of the MST Model (QM-MST)

If a QM formalism is used, the electrostatic contribution is determined as follows:

$$\Delta G_{ele} = \left\langle \psi^{sol} \middle| \widehat{H}^0 + \frac{1}{2}\widehat{V}_R \middle| \psi^{sol} \right\rangle - \left\langle \psi^0 \middle| \widehat{H}^0 \middle| \psi^0 \right\rangle \tag{3.7}$$

where ψ is the solute wave function, and indices "0" and "sol" represent gas-phase and solvent environments, respectively. QM-MST calculations were performed by using the optimized versions developed for the semiempirical AM1 wave function [44], which are implemented in the modified version of the MOPAC [135] program.

3.2.4 Semiclassical Formalism of the MST Model (SC-MST)

In the classical framework ΔG_{ele} adopts the expression indicated in Eq. (3.8), where $\{Q_i\}$ and $\{q_k\}$ correspond to the sets of partial charges that represent the charge distribution of the solute and the solvent reaction field, and where r_i and r_k stand for the position vectors of the solute and solvent charges, respectively.

$$\Delta G_{ele} = \frac{1}{2} \sum_{i=1}^{N} \sum_{k=1}^{M} \frac{Q_i q_k}{|r_i - r_k|} \tag{3.8}$$

To account for the contribution arising from the solute-solvent polarization effects, which are neglected in Eq. (3.8), ΔG_{ele} can be expressed as [94, 95, 115]:

$$\Delta G_{ele} = \frac{1}{2} \sum_{i=1}^{N} \sum_{k=1}^{M} \frac{Q_i^0 q_k(Q_i^{sol})}{|r_i - r_k|} \tag{3.9}$$

where $\{Q_i^0\}$ and $\{Q_i^{sol}\}$ are the charge distributions of the solute in the gas phase and in solution, respectively, and $\{q_k(Q_i^{sol})\}$ is the solvent reaction field computed from the charges that represent the fully relaxed charge distribution of the solute in solution. In the SC-MST procedure the electrostatic interaction between the solute and the solvent is evaluated by using Eq. (3.9) rather than Eq. (3.7) [94, 95, 115].

Obviously, the reliability of the SC-MST procedure largely depends on $\{Q_i^0\}$ and $\{Q_i^{sol}\}$. In the present study electrostatic potential-derived charges centered at the nuclei were computed at the ab initio HF/6-31G(d) level [77] by using the Gaussian 98 computer program [57]. The influence of the strategy used to derive $\{Q_i^0\}$ and $\{Q_i^{sol}\}$ was examined considering three different approaches:

Approach-1 (A1). Charges were computed only for the cone, which is the most stable conformation of both **1** and **2**, the electrostatic parameters for the paco and saddle being directly transferred from those of the cone. Furthermore, the four chemically equivalent fragments contained in the compounds under study (each fragment contains a phenolic ring and a methylene bridge) were constrained to have identical site charges. This approach closely follows the standard practice in MM of assigning identical charges to equivalent groups.

Approach-2 (A2). The dependence of the charges upon the conformation was taken into account. A specific set of atomic charges was computed for each of the three conformational states by using the procedure described above. However, chemically equivalent fragments were still required to have identical site charges within each state.

Approach-3 (A3). A set of parameters was developed for each conformation like above (A2), but no constraint was applied in the parametrization. Thus, each phenol was allowed to have its own set of atomic charges. For the paco and saddle large differences were found between the charges of the rotated phenolic unit and the other three, even although some differences were also detected among the latter.

For the three approaches, we included the effects produced by small thermal atomic motions on electrostatic parameters by evaluating the charges on several representative configurations of each conformation, and weighting them according to Boltzmann's distribution [7, 120].

3.3 Results and Discussion

3.3.1 Quantum Mechanical Calculations

The ΔG_{sol} values were computed for the cone, saddle and paco conformations of **1** and **2** by using QM-MST calculations. A set of 100 configurations, which were generated through MD simulations in a vacuum, was considered for each conformational state. Results are displayed in Table 3.1 and Table 3.2, which also show the effect of the solvent on the isomerization barrier [$\Delta\Delta G_{sol}$(cone-saddle)] and on the reaction equilibrium between cone and paco [$\Delta\Delta G_{sol}$(cone-paco)].

The solvation of both **1** and **2** is more favorable in chloroform than in water. Thus, the free energy to transfer such compounds in the cone conformation from water to the organic solvent is -12.3 kcal and -26.6 kcal/mol, respectively. Similar values are predicted for the saddle (-10.6 and -26.2 kcal/mol, respectively) and paco (-10.6 and -25.4 kcal/mol, respectively) conformations.

On the other hand, QM-MST calculations indicate that the influence of the organic solvent on the isomerization barrier is negligible for **1** and small for **2**. Thus, the$\Delta\Delta G_{sol}$(cone-saddle) predicted in chloroform solution for **1** is 0.0 kcal/mol, which is good agreement with the value previously estimated by using a discrete solvation model through MD simulations (0.7 kcal/mol) [36]. Accordingly, the interactions between the solute and the bulk solvent are predicted to be similar for these two conformational states.

The value provided in Table 3.2 for **2** (-1.2 kcal/mol) indicates that the interactions of bulk

chloroform with tert-butyl substituents are slightly more favorable for the saddle than for the cone. This feature was not fully supported by MD simulations, the estimations provided by different sampling schemes being 0.0 (windows umbrella sampling) and 0.3 kcal/mol (combined coupling parameter-umbrella sampling) [142]. However, the deviation between QM-MST and MD (1.2-1.5 kcal/mol) is within the error currently accepted when very different models are compared [32, 58, 63, 79].

The solvent-induced barriers decrease to -1.7 and -1.6 kcal/mol for **1** and **2**, respectively, when the environment is bulk water. The variation of the barrier with the polarity of the environment is consistent with the features detected by Kollman and co-workers [65] using MD simulations, and indicates that the hydration of the cone is worse than that of the saddle.

The $\Delta\Delta G_{sol}$(cone-paco) predicted in chloroform solution for **1** and **2** is 0.3 and -0.3 kcal/mol, respectively. Thus, the solvation predicted by QM-MST is similar for the two conformations even when the phenol ring is substituted in the para position by the *tert*-butyl group. The values derived from MD simulations were 1.3 and 1.6 kcal/mol for **1** and **2**, respectively.

Again, the differences between the results provided by continuum and discrete models are within an acceptable interval. On the other hand, the paco conformation is clearly better hydrated than the cone in all cases, as was also predicted by MD simulations [150]. It is interesting to examine the influence of the number of configurations considered for each conformational state on ΔG_{sol}. Figure 3.3 shows the values of the ΔG_{sol} in aqueous solution for the configurations generated to represent the saddle conformation of **1**. Each point corresponds to one of the 100 configurations generated by MD simulations whereas the solid line displays the final weighted average. It is worth noting that ΔG_{sol} ranges from -8.4 to -11.6 kcal/mol indicating that this thermodynamic parameter is considerably affected by small atomic displacements. Thus, to predict free energy differences associated with conformational changes, a significant number of configurations must be used to represent each conformational state of flexible molecules. In this case the mean ΔG_{sol} values are converged after $\sim$30 configurations.

Similar results were obtained for the cone and paco conformations of **1** and for **2**, the ΔG_{sol} values ranging in these cases (in absolute values) from 7.8 to 10.1 kcal/mol (cone, **1**), 8.4-11.2 kcal/mol (paco, **1**), 7.0-10.1 kcal/mol (cone, **2**), 7.7-11.2 kcal/mol (paco, **2**) and 9.3-

Table 3.1: Free energies of solvation (ΔG_{sol}, in kcal/mol) in chloroform and water computed for the cone, saddle and paco conformational states of **1**[a] (see Fig. 3.2) using different formalisms of the MST[b] model. The influence of the solvent on the conformational isomerism of this compound is expressed in terms of $\Delta\Delta G_{sol}$.

		QM	SC(A1)	SC(A2)	SC(A3)
chloroform	ΔG_{sol}(cone)	-21.6	-22.2	-22.2	-22.8
	ΔG_{sol}(saddle)	-21.6	-24.4	-23.4	-22.7
	ΔG_{sol}(paco)	-21.3	-25.0	-23.7	-22.8
	$\Delta\Delta G_{sol}$(cone-saddle)	0.0	-2.2	-1.2	0.1
	$\Delta\Delta G_{sol}$(cone-paco)	0.3	-2.8	-1.5	0.0
water	ΔG_{sol}(cone)	-9.3	-14.1	-14.1	-14.8
	ΔG_{sol}(saddle)	-11.0	-18.9	-16.6	-16.1
	ΔG_{sol}(paco)	-10.7	-20.5	-17.7	-16.2
	$\Delta\Delta G_{sol}$(cone-saddle)	-1.7	-4.8	-2.5	-1.3
	$\Delta\Delta G_{sol}$(cone-paco)	-1.4	-6.4	-3.6	-1.4

[a] A set of 100 configurations were considered for each conformational state. [b] MST: Miertus, Scrocco and Tomasi solvation model. QM: quantum mechanical at the semiempirical AM1 level. SC(A1): semiclassical-approximation 1; SC(A2): semiclassical-approximation 2. SC(A3): semiclassical-approximation 3. For a more detailed description of the methods used to evaluate the ΔG_{sol} see the Methods section.

Table 3.2: Free energies of solvation (ΔG_{sol}, in kcal/mol) in chloroform and water computed for the cone, saddle and paco conformational states of **2**[a] (see Fig. 3.2) using different formalisms of the MST[b] model. The influence of the solvent on the conformational isomerism of this compound is expressed in terms of $\Delta\Delta G_{sol}$.

		QM	SC(A1)	SC(A2)	SC(A3)
chloroform	ΔG_{sol}(cone)	-35.9	-36.2	-36.2	-38.3
	ΔG_{sol}(saddle)	-37.1	-38.7	-37.8	-39.1
	ΔG_{sol}(paco)	-36.2	-41.3	-39.8	-38.8
	$\Delta\Delta G_{sol}$(cone-saddle)	-1.2	-2.5	-1.6	-0.8
	$\Delta\Delta G_{sol}$(cone-paco)	-0.3	-5.1	-3.6	-0.5
water	ΔG_{sol}(cone)	-9.3	-11.3	-11.3	-10.7
	ΔG_{sol}(saddle)	-10.9	-17.7	-14.4	-13.1
	ΔG_{sol}(paco)	-10.8	-19.1	-15.2	-12.4
	$\Delta\Delta G_{sol}$(cone-saddle)	-1.6	-6.4	-3.1	-2.4
	$\Delta\Delta G_{sol}$(cone-paco)	-1.7	-7.8	-3.9	-1.7

[a] A set of 100 configurations, which were generated by using molecular dynamics simulations, were considered for each conformational state. [b] MST: Miertus, Scrocco and Tomasi solvation model. QM: quantum mechanical at the semiempirical AM1 level. SC(A1): semiclassical-approximation 1; SC(A2): semiclassical-approximation 2. SC(A3): semiclassical-approximation 3. For a more detailed description of the methods used to evaluate the ΔG_{sol} see the Methods section.

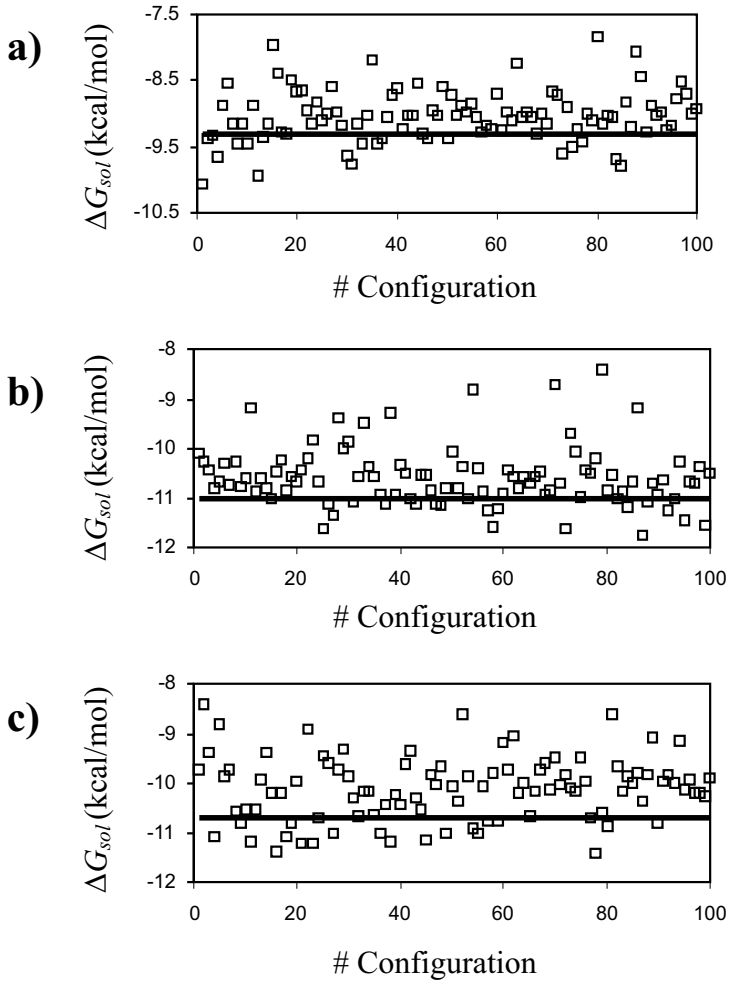

Figure 3.3: ΔG_{sol} in aqueous solution calculated by using the QM-MST method for 100 configurations of the cone (a), saddle (b) and paco (c) conformational states of **1**. The solid line corresponds to the final weighted average value.

11.7 kcal/mol (saddle, **2**). These variations are smaller (typically 50% less) in chloroform solution. It should be noted that the influence of the solvent on the internal degrees of freedom of the solute is usually accounted for by discrete methods based on MM. However, these simulations are computationally very demanding, since most of the computer time is spent on sampling the solvent configurational space. The combination of the continuum approach to represent the solvent with the solute configurations generated by MD simulations in vacuo provides a useful alternative to discrete methods to represent flexible molecules in solution.

3.3.2 Semiclassical Calculations

ΔG_{sol} values derived from SC(A1)-, SC(A2)- and SC(A3)-MST calculations are included in Table 3.1 and Table 3.2. It is worth noting that the reliability of the SC-MST results strongly depends on the quality of the atomic charges used to describe the QM electronic distribution of the solute. The influence of the electrostatic parameters on the ΔG_sol values predicted by this method has been examined by computing the mean unsigned difference with respect to the QM-MST results (Table 3.3).

The poor results provided by the SC(A1)-MST method, which involves many of the approximations typically applied in classical MM, are surprising and even disturbing. The mean unsigned differences are 2.3 and 6.6 kcal/mol in chloroform and aqueous solution, respectively, which arise from the unsatisfactory description of the ΔG_{sol} for the paco and saddle conformations. Furthermore, the influence of the solvent in the $\Delta\Delta G_{sol}$(cone-saddle) barrier was overestimated by 2.2 and 1.3 kcal/mol (in absolute value) for **1** and **2**, respectively, in chloroform solution, and by 3.1 and 4.8 kcal/mol in aqueous solution. The error is even larger in the difference $\Delta\Delta G_{sol}$(cone-paco): 3.1 and 4.8 kcal/mol for **1** and **2**, respectively, in chloroform solution, and 5.0 and 6.1 kcal/mol in aqueous solution. These results clearly indicate that the atom-centered charges derived from the cone conformation are not able to represent the QM electronic distribution of the saddle and paco states. This deficiency could be avoided by deriving explicit charge models for each conformation, as was described in the Section 3.2 (Approximation 2).

Results provided by the SC(A2)-MST formalism indicate a significant improvement with respect to those obtained with the SC(A1)-MST one. As is reflected in Table 3.3, the mean

Table 3.3: Mean unsigned difference (in kcal/mol) between the free energies of solvation determined from QM-MST and SC-MST calculations on the three conformational states of **1** and **2**.

method MST	chloroform	water
SC(A1)	2.3	6.6
SC(A2)	1.6	4.5
SC(A3)	1.8	3.5

unsigned difference decreases by about 30% in both chloroform and water. Furthermore, the $\Delta\Delta G_{sol}$ values predicted by the former method are smaller than those computed by using the latter one by about a half. This reduction is similar for the two solutes, indicating that for solutes with complex electron distributions, like calixarenes, the electrostatic parameters cannot be transferred routinely among different conformations. Despite this notable improvement, a detailed inspection of Table 3.1 and 2 shows that the conformationally dependent charges still produce significant errors, the $\Delta\Delta G_{sol}$ values computed with the SC(A2)-MST method being approximately twice as large as those predicted by QM-MST. This feature motivated the investigation of a new model in which the electrostatic parameters are accurately obtained (Approximation 3) not only for each conformation but also for each fragment of the molecule.

The $\Delta\Delta G_{sol}$ values obtained for **1** and **2** using the SC(A3)-MST formalism are in excellent agreement with those produced by the QM-MST method. Thus, although the ΔG_{sol} obtained with the SC(A3)-MST and SC(A2)-MST methods present similar unsigned differences with respect to the QM-MST ones, a marked improvement is achieved by the latter approximation in the relative values. This is specially notable for **1**, where the largest difference with respect to the $\Delta\Delta G_{sol}$ values predicted by QM-MST is 0.4 kcal/mol. Accordingly, the electrostatic charges directly derived from the fitting between the quantum and classical molecular electrostatic produces a drastic increase in the quality of the results.

The systematic overestimation of the ΔG_{sol} values produced by SC(A2)-MST and

SC(A3)-MST calculations is attributed to the use of an atom-centered charge model since all the other simplifications typically used in the parametrization of electrostatic charges have been omitted, especially in the latter approximation. An atom-centered model involves a drastic simplification of the description of the molecular charge distribution, which can often provide a sufficiently accurate representation of the molecular systems. Nevertheless, in this case a more precise representation of the charge distribution is needed. Accordingly, more sophisticated models, like the multicentric ones [6, 154, 155], should be employed to obtain a better quantitative agreement between SC- and QM-MST results.

3.3.3 Analysis of the Reliability of the MST Method

Inspection of the literature reveals that experimental ΔG_{sol} values for **1** and **2** are not available. The experimental measurement of this thermodynamic parameter is precluded in many cases by the technical difficulties of obtaining equilibrium constants for large exothermic reactions like the solvation of a solute. As a consequence, the ΔG_{sol} values for important bioorganic systems, like for instance the nucleic acid bases and some amino acids, remain unknown, making the theoretical methods powerful tools to provide new insights into the solution-phase properties of such compounds. However, to make quantitative predictions, it is necessary to be able to calculate ΔG_{sol} to high accuracy and this is the subject of this section. QM and SC calculations have been performed to calibrate the reliability of ΔG_{sol} values provided by MST for complex molecules such as calixarenes.

Table 3.4 compares the experimental and predicted ΔG_{sol} in chloroform and water for a few small model compounds that are closely related to the investigated calixarenes. As expected, the performance of the MST method is very consistent in both chloroform and aqueous solutions.

In chloroform solution the largest error between the QM-MST and experimental ΔG_{sol} values is 1.3 kcal/mol and the mean unsigned deviation is 0.6 kcal/mol, whereas in aqueous solution these values are 2.0 and 0.8 kcal/mol, respectively. The rms deviation between QM-MST and experimental values is 0.9 and 1.1 kcal/mol for solvation in chloroform and water, respectively. Analysis of the ΔG_{sol} determined from SC-MST calculations provides similar statistical parameters. Inspection of the mean signed deviation indicates that both the QM and SC formalisms of the MST model tend to slightly overestimate slightly the ΔG_{sol}. Overall,

Table 3.4: Free energies of solvation (ΔG_{sol}, in kcal/mol) in chloroform (first line) and water (second line) determined from QM-MST and SC-MST calculations on selected model compounds and statistical comparison between the theoretical and experimental values.

compd	exptl	QM-MST	SC-MST
water	-2.0	-2.7	-3.6
	-6.3	-6.1	-7.2
methanol	-3.4	-3.0	-3.5
	-5.1	-3.6	-4.1
dimethyl ether	-	-3.4	-3.6
	-1.9	-2.0	-2.5
diethyl ether	-4.3	-4.4	-4.4
	-1.8	-2.5	-3.4
benzene	-4.6	-5.9	-3.8
	-0.9	-1.6	-1.8
phenol	-7.1	-7.2	-8.0
	-6.6	-4.6	-6.4
toluene	-5.4	-6.5	-6.7
	-0.9	-1.9	-1.6
ethylbenzene	-5.8	-7.1	-7.3
	-0.8	-2.0	-1.5
p-cresol	-7.6	-7.7	-7.9
	-6.1	-6.3	-6.8
rms[a]	-	0.9	1.1
		1.1	0.9
mud (msd)[b]	-	0.6(-0.5)	0.8(-0.6)
	-	0.8(0.0)	0.8(-0.5)

[a]rms: root mean square deviation. [b]mud: mean unsigned deviation. msd: mean signed deviation.

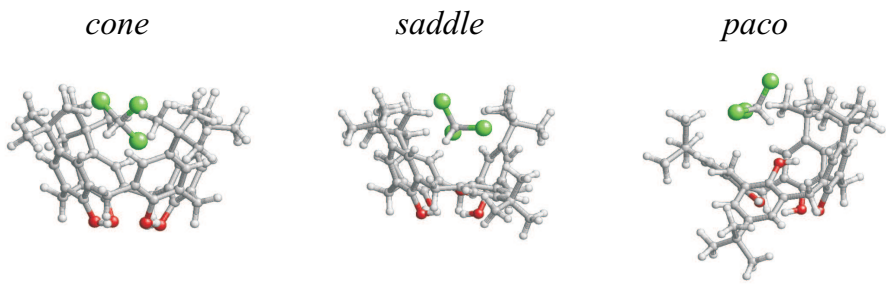

Figure 3.4: Atomistic representation of the cone, saddle and paco conformations for 2. The chloroform molecule trapped inside the cavity is also displayed.

there is excellent agreement between experimental and theoretical ΔG_{sol} in the two solvents for the series of selected model compounds.

On the other hand, the omission of specific solute-solvent interactions could limit the usefulness of continuum models for organic solutes with complex molecular structures. This situation is specially important for **2**, whose cavity is large enough to capture a chloroform molecule [15, 142]. Thus, a very accurate description of the solute/solvent interface is required to account for the influence on ΔG_{sol} of the solvent molecule trapped in the cavity of the solute. It should be emphasized that discrete models are able to represent this situation satisfactorily [142].

The reliability of the MST model to study the solvation of organic solutes with complex molecular structures has been demonstrated in recent studies involving calixpyrroles [21] and rotaxanes [54]. However, we gave put the model further to test by comparing the ΔG_{sol} predicted by all-continuum QM-MST calculations with that obtained through a discrete/QM-MST model [2, 3, 5], in which the captured chloroform is explicitly represented. SC calculations were not performed to avoid the influence of the electrostatic parametrization on this analysis. A set of 25 configurations was selected for each conformational state of **2** from MD trajectories in chloroform solution, with a solvent molecule inside the molecular cavity in all selected configurations [142]. This situation is illustrated in Figure 3.4, which shows a representative configuration of the cone, saddle and paco.

The ΔG_{sol} for **2** with one explicit chloroform molecule ($\Delta G_{sol}^{\text{E-CHL}}$) was computed as the sum of the gas-phase binding energy (ΔE_{gp}) between the solute and the explicit chloroform

Table 3.5: Free energies of solvation[a] (in kcal/mol) in chloroform computed for the cone, saddle and paco conformational states of **2** using discrete/continuum and all continuum calculations.

	cone	saddle	paco
$\Delta G_{sol}^{\text{E-CHL}}$	-36.4	-38.2	-37.2
$\Delta G_{sol}^{\text{D/MST}}$	-32.4	-34.9	-33.5
$\Delta G_{sol}(\mathbf{2})$	-35.9	-37.1	-36.2
$\Delta G_{sol}^{\text{D/MST}} - \Delta G_{sol}(\mathbf{2})$	3.2±1.1	2.2±0.9	2.7±1.2

[a] $\Delta G_{sol}^{\text{E-CHL}}$ corresponds to the free energy of solvation of the complex $\mathbf{2}\cdot\text{CHCl}_3$ estimated by using Eq. (3.10). $\Delta G_{sol}^{\text{D/MST}}$ is the free energy of solvation of **2** obtained by using the formalism indicated in Eq. (3.11) for discrete/continuum models. $\Delta G_{sol}(\mathbf{2})$ is the free energy of solvation of **2** obtained by using all continuum calculations. In all cases the QM-MST continuum method was used.

molecule, which for consistency was computed at the semiempirical AM1 level [44], and the ΔG_{sol} computed for the complex ($\mathbf{2}\cdot\text{CHCl}_3$) using the QM-MST method [2, 3, 5]:

$$\Delta G_{sol}^{\text{E-CHL}} = \Delta E_{\text{gp}} + \Delta G_{sol}(\mathbf{2}\cdot\text{CHCl}_3) \tag{3.10}$$

Ideally, $\Delta G_{sol}^{\text{E-CHL}}$ should be identical with the sum of the ΔG_{sol} values computed for the chloroform molecule and for **2** with use of the all-continuum model. Therefore, the ΔG_{sol} for **2** provided by the combined discrete/QM-MST model ($\Delta G_{sol}^{\text{D/MST}}$) can be determined as:

$$\Delta G_{sol}^{\text{D/MST}} = \Delta G_{sol}^{\text{E-CHL}} - \Delta G_{sol}(\text{CHCl}_3) \tag{3.11}$$

Obviously, the differences between $\Delta G_{sol}^{\text{D/MST}}$ and the ΔG_{sol} obtained by using the same conditions in the all-continuum model allow one to estimate the accuracy of the latter to describe the solvation of **2**. Table 3.5 shows the values of $\Delta G_{sol}^{\text{E-CHL}}$ and $\Delta G_{sol}^{\text{D/MST}}$ for the three conformational states of **2**. Inspection of the $\Delta G_{sol}^{\text{E-CHL}}$ estimations reveals that the chloroform molecule trapped inside the cavity does not alter the solvation order of the three conformational states. Thus, the interaction between the $\mathbf{2}\cdot\text{CHCl}_3$ complex and the bulk chloroform

increases as follows: saddle > paco > cone. Furthermore, the $\Delta\Delta G_{sol}^{\text{E-CHL}}$ (cone-saddle) and $\Delta\Delta G_{sol}^{\text{E-CHL}}$(cone-paco) values are -1.8 and -0.8 kcal/mol, respectively, which are very similar to the values obtained without including any explicit solvent molecule.

A similar qualitative agreement is reflected by the values of $\Delta G_{sol}^{\text{D/MST}}$ estimated for the cone, saddle and paco conformations. However, the $\Delta G_{sol}^{\text{D/MST}}$ values are underestimated by about 3 kcal/mol with respect to the ΔG_{sol} obtained by using the all continuum model, although relative values present a noticeable agreement. This systematic failure is probably due to an overestimation of the ΔG_{sol} predicted by QM-MST for the chloroform molecule (Eq. (3.11)). Thus, the excellent agreement found between $\Delta\Delta G_{sol}^{\text{D/MST}}$ and $\Delta\Delta G_{sol}$ values allow us to conclude that the MST continuum model provides a satisfactory description of the molecular cavity, i.e. no explicit solvent molecule is required.

3.4 Conclusions

The results presented in this chapter allow us to conclude that the MST continuum model is able to provide, at least qualitatively, a reliable description of the role of the solvent on the conformational isomerism of complex solutes such as calixarenes. Support to this conclusion comes from the comparison between the results obtained in the present work for different frameworks of the MST model with those reported in previous studies where the discrete solvation model was employed through classical MD simulations. It has been shown that the effects of the solvent on the conformational preferences of calixarenes are satisfactorily reproduced by using a combined approach in which the configurational space of the solute is sampled through in vacuo MD simulations and the bulk solvent is represented with an implicit continuum model. From a practical point of view, this appears to be an efficient approach that requires less computer power than conventional MD simulations with their explicit description of solvent particles. The strategy was tested with two representative calixarenes, **1** and **2**, and using two different solvents. It is very encouraging that the application of the QM-MST method to the configurations generated in vacuo correctly reproduces the tendencies previously predicted by MD simulations in solution.

The performance of the SC-MST method has been examined, Particular attention has been paid to the parametrization of the atomic charges required to evaluate the electrostatic

contribution to ΔG_{sol}. The results reveal that the SC-MST method is an inexpensive procedure to investigate solvation effects when suitable atomic charges are used. Thus, the accuracy of the results clearly depends on the quality of the electrostatic parameters. The results presented here indicate that the method works well when standard molecular electrostatic potential-derived charges are directly used, i.e. avoiding the approximations usually employed in the MM calculations. Furthermore, better results should be obtained by improving the charge representation, e.g. by using atomic dipoles or multicentric charges.

Finally, it should be mentioned that although the results presented in this study give confidence in the suitability of inexpensive MST continuum model to account for solvation effects on the conformational preferences of calixarenes, the method would present a potential limitation. This is the lack of information about solvent molecules plays a relevant structural or dynamical roles. In these cases MD with explicit solvent molecules is usually the most appropriate procedure [36, 39, 142]. However, in some cases these deficiencies can be alternatively corrected by introducing discrete solvent molecules into the continuum calculation with little increase in computer expense. In this way both macroscopic and microscopic solvation effects are taken into account. In summary, each strategy has its strengths and shortcomings, and the judicious selection of the appropriate method to be used in the study of a particular problem is probably the most important decision for the study of a chemical process in solution.

4 Influence of a captured solvent molecule on the isomerization rates of calixarenes

The conformational inversion rates of calix[4]arene and p-tert-butyl-calix[4]-arene in vacuum and in chloroform have been calculated by using molecular dynamics simulations, as a model study for a process with a pronounced solvent effect. The reaction of a p-tert-butyl-calix[4]arene in chloroform is complicated by the ability of one its conformations to capture a chloroform molecule in its cavity, while the smaller cavity of the calix[4]arene is too small for an inclusion. The relatively easily obtained free energies of conformational inversion in a vacuum prove to be a great asset in the calculations with calix[4]arene in chloroform. But they are of limited use for p-tert-butyl-calix[4]arene in chloroform, where we had to resort to more advanced methods, to wit, window sampling and a combined coupling parameter - umbrella sampling approach. Conformational inversion rates calculated by the reactive flux method are in good agreement with experimental data. *

4.1 Introduction

Calix[4]arenes are macrocyclic molecules consisting of four phenol rings connected via methylene bridges in the ortho positions with respect to the hydroxyl group, see Fig. 4.1. Ever since their discovery in the 1940's and 1950's, they have continued to attract the attention of supra molecular chemists [73]. Calixarenes are renowned for their usage as building blocks

∗ The work described in this chapter previously appeared in J. Phys. Chem. B **107**, 14476 (2003) [142].

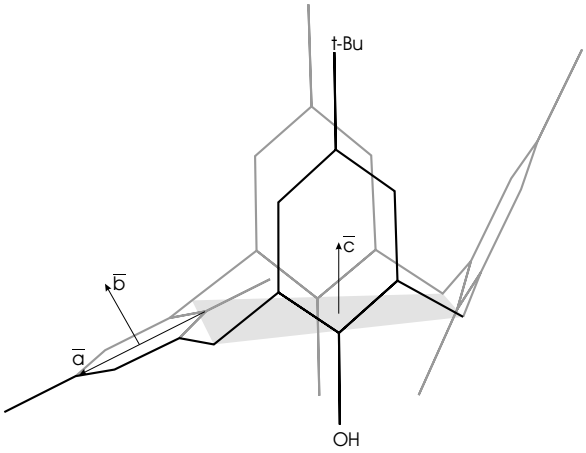

Figure 4.1: The standard calix[4]arene has hydroxyl groups attached at the lower rim of the benzene rings, and hydrogens at the upper rim. The *p-tert*-butyl-calix[4]arene has $C(CH_3)_3$ groups at the upper rim. The drawn vectors are instrumental in the definition of the reaction coordinate. For clarity, we show the side groups for one phenol ring.

in large aggregates stabilized by hydrogen bonds. Zinke [160] and subsequent workers with calixarenes have noted their propensity to form molecular complexes with smaller molecules, a direct consequence of the presence of a cavity in the center of a calixarene [9, 67, 144]. The properties that make calixarenes so popular, their small size and versatility, also make them very suitable for computer modelling. By studying the isomerization process of solvated calixarenes, we want to illustrate and validate the capabilities of current simulation methods.

Calix[4]arenes have four different conformations, distinguished by the rotation of the phenol rings with respect to the central annulus, with the methylene groups acting as hinges. In the “cone” conformation all phenol rings are oriented in the same direction. When one of the phenol rings is rotated with respect to the other three phenol rings, the conformation is called “paco” (short for partial cone). The conformations with two rotated phenol rings are “1,2-alternate”(two neighboring phenol rings have rotated) and “1,3-alternate”(two opposite phenol rings have rotated).

The isomerization reaction from cone to paco will be studied in this chapter by molecular dynamics simulations (MD). The free energy barrier between these two conformations was

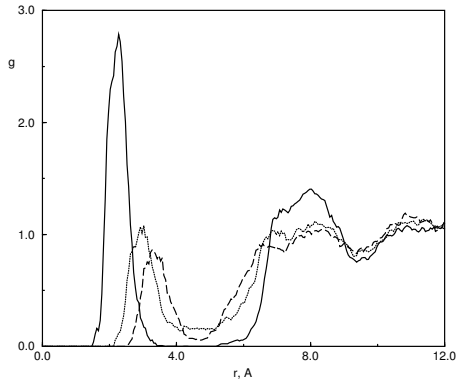

Figure 4.2: Radial distribution functions of the carbon atom of chloroform relative to the center of mass of the *p-tert*-butyl-calix[4]arene for the cone (solid line), paco (dashed line) and transition state (dotted line) configuration.

determined by NMR experiments to be about 15-16 kcal/mol [10, 70]. This means that the molecule stays in the cone conformation for most of the time, and crosses the transition state corresponding to the top of the energy barrier only once every 10 to 100 ms. So, the conformational inversion rate cannot be obtained from a normal MD run, which typically covers only 10 to 100 ns. Previous calculations of rate constants and reaction equilibria have therefore focused on locating the energy minima and transition states, and their normal modes in a vacuum [53, 65, 75, 76, 125, 151]. Simulations with solvents have placed the emphasis on the complexation with ions [1, 152, 66]. To bridge the aforementioned time gap, in the reactive flux method the reaction rate is expressed as the product of two terms. First the probability of a calix in the cone conformation to reach the top of the energy barrier is calculated. Being an equilibrium property, statistical mechanics offers routes to calculate this probability in the allotted time. Second, the chance that a molecule at the top proceeds to the paco conformation is calculated. These downhill runs proceed very quickly, typically taking only a couple of picoseconds.

For reactions with a clear-cut reaction barrier the above approach works satisfactorily, but less obvious reaction paths require more advanced calculation methods, like “transition path sampling” [22]. Although these techniques are well-established, their practical application is

frequently less straightforward. Fig. 4.2 shows the radial distribution function of chloroform solvent molecules around a *p-tert*-butyl-calix[4]arene, a calix with *tert*-butyl groups at the upper rim. One clearly sees a sharp peak followed by a region of zero probability for the cone conformation, indicating that one chloroform molecule is firmly captured in the cavity of the *p-tert*-butyl-calix[4]arene. Inclusions of chloroform, and a range of other molecules, in calix[4]arenes have also been observed by X-ray structure determination [24, 144], NMR [15, 24] and quantum mechanical calculations [13, 25, 110]. It suggests that the solvent will have a pronounced effect on the reaction, which complicates the calculations. In Sections 4.2 and 4.4 we describe and compare different approaches to this problem. In Section 4.5 we find a good agreement between our calculated rates and experimental values, and for the simpler "bare" calix we recover rates previously calculated by a different technique. A detailed analysis of the captured chloroform, and its influence on the reaction, is presented in Section 4.6.

4.2 Theory

4.2.1 Reaction Rates

The calculation of the reaction rate requires the introduction of a parameter which separates products and reactants. This parameter, or reaction coordinate, ξ, is usually chosen to be a function of the coordinates of the reacting molecule only [11, 29, 74]. A reaction coordinate is defined such that it is larger than $\xi^{\neq}$ for products and smaller than $\xi^{\neq}$ for reactants. So, reactants and products are divided by the transition state plane $\xi = \xi^{\neq}$, which is located in the thinly populated area near the top of the energy barrier.

According to Eyring's transition state theory (TST), the forward rate constant is calculated as the instantaneous product-bound flux through the transition state, normalized by the population of the reactant space [11, 29, 39, 51, 56, 74]:

$$k_f^{TST} = \frac{\langle \dot{\xi}\Theta(\dot{\xi})\delta(\xi - \xi^{\neq})\rangle}{\langle \Theta(\xi^{\neq} - \xi)\rangle} = \frac{\langle |\dot{\xi}|\rangle_{\xi^{\neq}}}{2} \frac{P(\xi^{\neq})}{\int_{-\infty}^{\xi^{\neq}} P(\xi)\, d\xi}. \tag{4.1}$$

Here $\dot{\xi} = d\xi/dt$, δ and Θ are the Dirac delta function and Heaviside step function, respectively, and the broken brackets denote a canonical average, with the subscript $\xi^{\neq}$ indicting

a restriction to the transition state. The probability distribution on the right-hand side represents an integral of the Boltzmann factor over all configurations with the same value of the reaction coordinate [39, 56]:

$$P(\xi^*) = \frac{1}{Q} h^{-3N} \int\int \delta[\xi(\mathbf{X}) - \xi^*] \exp[-\beta H(\mathbf{X}, \mathbf{p}_X)] \, d\mathbf{X} \, d\mathbf{p}_X, \tag{4.2}$$

where H is the Hamiltonian, $\mathbf{X}$ is the collection of all $3N$ coordinates, $\mathbf{p}_X$ are conjugate momenta, h is Planck's constant, and $\beta = 1/k_B T$. The partition function Q arises as the normalization factor of the distribution.

Transition state theory gives an over-estimated value as compared with the true reaction rate, because TST does not take into account the possibility of rapid re-crossings [11, 29, 39, 51, 56, 74]. For example, a molecule can cross the transition state, collide with a solvent particle, and bounce back to its original configuration. Such a trajectory will contribute to the TST rate (it once crosses the transition state with a positive velocity), but it does not contribute to the true reaction rate. Likewise, re-crossings will also be occurring if the chosen transition state happened to lie below the top of the energy barrier. As a compensation, the reactive flux method (RF) introduces a transmission coefficient κ, whose value lies between zero and one [29, 74]:

$$k_f^{RF} = \kappa k_f^{TST}. \tag{4.3}$$

Under the conditions that classical mechanics adequately describes the motion of the molecule, the transmission coefficient can be calculated exactly. From Onsager's regression hypothesis it follows [29, 74], that re-crossings within a time t following the initial crossing reduce the reaction rate by a factor

$$\kappa(t) = \frac{\left\langle \delta[\xi(0) - \xi^{\neq}] \, \dot{\xi}(0) \, \theta[\xi(t) - \xi^{\neq}] \right\rangle}{\left\langle \delta[\xi(0) - \xi^{\neq}] \, \dot{\xi}(0) \, \theta[\dot{\xi}(0)] \right\rangle}. \tag{4.4}$$

If the energy barrier is high, and the energy transfer to the solvent is efficient, then only molecules that are still near the transition state are capable of re-crossing. Once the molecule has reached the reactant or product state, and its excess energy has been dissipated by the solvent, it will only re-cross on a time scale associated with the reaction rate itself. This suggests that $\kappa(t)$ shows a rapid transient decay from a value of 1 to a plateau value, which in turn is decaying very slowly. It is this plateau value which enters in eq. 4.3.

Substituting eq. 4.1 into eq. 4.3, and converting probability distributions into free energies using

$$A(\xi) = -k_B T \ln P(\xi) + constant, \tag{4.5}$$

we rewrite the expression for the RF rate as

$$k_f^{RF} = \kappa \sqrt{\frac{k_B T}{2\pi}} \left\langle \sqrt{\sum_i \frac{1}{m_i} \left(\frac{\partial \xi}{\partial x_i}\right)^2} \right\rangle_{\xi^{\neq}} \exp\left[-\frac{A(\xi^{\neq}) - A_R}{k_B T} \right]. \tag{4.6}$$

Here A_R is the free energy of the integrated probability of the reactant well, and the average velocity of the reaction coordinate has been re-cast in an easily evaluated form [36, 39]. In the experimental literature a slightly different definition of the free energy is commonly used, by writing a measured reaction rate as

$$k_f^{exp} = \frac{k_B T}{h} \exp\left[-\frac{\Delta A^{\neq}}{k_B T} \right]. \tag{4.7}$$

4.2.2 Umbrella sampling

As mentioned in the section 4.1, the high free energy barrier means that the molecule stays in one conformation for a long time. The barrier region will be sampled very poorly in a simulation, and it is quite likely that it is not sampled at all. To eliminate the difficulties with the sampling, we add to the existing potential energy an "umbrella" potential $U(\mathbf{X})$, which reduces the free energy differences between reactants, products and transition state. The probability distribution of the system with the umbrella potential reads

$$P_U(\xi) = \frac{1}{Q_U} h^{-3N} \int\int \delta[\xi(\mathbf{X}) - \xi^*] \exp\left[-\beta \{H(\mathbf{X}, \mathbf{p}_X) + U(\mathbf{X})\} \right] d\mathbf{X}\, d\mathbf{p}_X. \tag{4.8}$$

In case the umbrella potential is a function of the reaction coordinate only, the distribution in the biased run is easily converted into the probability distribution of the unbiased run,

$$P(\xi) = c\, P_U(\xi) \exp[\beta U(\xi)], \tag{4.9}$$

where c is a proportionality constant. The particular choice $U(\xi) = -A(\xi)$ would make P_U a constant, independent of ξ. In the biased run then, the barrier between products and reactants has effectively vanished, and both regions can be sampled sufficiently with a single run. But,

at the start of our simulations we do not know what the free energy function looks like, so we can only make educated guesses for the umbrella. If a long simulation with a trial umbrella samples the entire range of the reaction coordinate but the distribution is not reasonably flat, then the sampled probability distribution may be converted into a potential according to eq. 4.5 and added to the existing umbrella to define a new trial umbrella for a second simulation and so on. A useful first guess for an umbrella is the minimum energy as a function of the reaction coordinate.

It all becomes a bit more complicated if the initial guess fails to sample the entire relevant range of the reaction coordinate. In this work we used two extensions of umbrella sampling to circumvent this deficiency. In "windows" sampling [85] the single umbrella for the entire range is replaced by a series of L umbrellas $U_l(\xi)$, $l = 1, ..., L$, each covering a small range of the reaction coordinate. The calculated distributions $P_l(\xi)$ are then combined into a single distribution by using the proportionality constants c to match the partial distributions at the overlap of successive windows. In the second method we combine umbrella sampling with the coupling parameter approach. The later is frequently used for thermodynamic integration of the free energy difference between similar molecules [99, 100, 117, 157]. A coupling parameter λ transforms the force field representative of molecule A ($\lambda = 0$) into the force field representative of molecule B ($\lambda = 1$) via a series of intermediate, non-physical molecules:

$$\Phi(\mathbf{X}, \lambda) = (1 - \lambda)\, \Phi_A(\mathbf{X}) + \lambda\, \Phi_B(\mathbf{X}). \tag{4.10}$$

In the current case, the coupling parameter was used to turn on the interaction between the isomerizing solute and the solvent. We used a series of runs from $\lambda = 1$ (no interaction) to $\lambda = 0$ (full interaction) with $\lambda_{i+1} = \lambda_i - \Delta\lambda$, and a different umbrella potential $U_\lambda(\xi)$ for each λ_i. The probability distribution in this case is just

$$P_\lambda(\xi) = \frac{1}{Q_{U,\lambda}} \int \delta[\xi(\mathbf{X}) - \xi^{\neq}] \exp\left[-\beta\{\Phi(\mathbf{X}, \lambda) + U_\lambda(\xi)\}\right] d\mathbf{X}. \tag{4.11}$$

Like standard umbrella sampling, this will only work efficiently if we have a reasonably flat distribution for each λ_i. This is achieved by using the umbrella that flattened the distribution at λ_i as the first trial umbrella potential for λ_{i+1}, provided the steps $\Delta\lambda$ are sufficiently small.

4.3 Model and Simulation details

As a reaction coordinate we use the intuitively appealing angle between the rotating phenol ring and the central annulus. For this purpose, the carbon atoms of the phenol ring are numbered 1 through 6, starting at the carbon connected to the hydroxyl group, and the carbons of the methyl group connecting rings are labelled a through d, with a and b at either side of the rotating ring. The orientation of the phenol ring is then described by the vectors $\mathbf{a} = \mathbf{x_4} - \mathbf{x_1}$ and $\mathbf{b} = (\mathbf{x_5} - \mathbf{x_2}) \times (\mathbf{x_6} - \mathbf{x_3})$. For the central annulus the vector $\mathbf{c} = (\mathbf{x_a} - \mathbf{x_c}) \times (\mathbf{x_b} - \mathbf{x_d})$ is used. The main value of the reaction coordinate is given by the angle φ_a between **a** and **c**. As this angle proves unreliable for configurations where **a** and **c** are roughly parallel, and to extend the range beyond $0 - 180°$, we introduce a second angle, φ_b between **b** and **c**. By simple arithmetic manipulations the value of φ_b is made to correspond with φ_a, and a smooth switching function is introduced to combine the two into a single differentiable reaction coordinate.

Both calixarenes were modelled using the CHARMM parameter set, version 22. This force field has been used before for reaction rate calculations and molecular modeling of calixarenes [36, 37, 39, 53, 125]. Of course, the results depend on the force field used. The complete force field can be found in ref [53]. All bond lengths involving a hydrogen atom were constrained using the SHAKE algorithm, to accelerate the calculations with a negligible loss of accuracy [37]. For the simulations in a vacuum the range of the nonbonded interactions was set at infinity. In chloroform the intermolecular interactions were truncated at 1.3 nm, using a charge group list, while the nonbonded intra-calix interactions were not truncated at all. The chloroform was modeled as rigid bodies by using the potential of ref [45]. The truncated octahedral periodic simulation box contained 317 chloroform molecules surrounding the calix (box size≈4.4 nm) and 386 molecules around the *p-tert*-butyl-calix[4]arene (≈4.8 nm), which is sufficiently large to prevent any solvent molecule from interacting with a solute and one of its periodic images simultaneously. The temperature and pressure were stabilized at 300 K and 1 bar, by a Nosé-Hoover baro-thermostat, using time constants of 0.1 and 0.5 ps, respectively. All simulations were done with a modified version of DL_POLY_2.0 [131].

4.4 Free energy

As a first estimate for the umbrella we used the minimum energy as a function of the reaction coordinate for the molecule in a vacuum. The minima were calculated by cooling the molecule down to 10 K, with a Gaussian temperature constraint, keeping the reaction coordinate constrained during every run. In the subsequent umbrella runs in a vacuum the region of motion of the reaction coordinate was restricted from $-20°$ to $200°$, to reduce the chances of "spontaneous" conformational transitions due to the high stress in the molecule beyond these extremes. These outermost conformations have much higher energies than the cone and paco minima (at approximately $31°$ and $168°$ respectively), thus only highly improbable conformations are excluded. This limitation was done by adding two Fermi−Dirac-like functions to the umbrella, chosen such that they were virtually zero in the interesting region and rapidly increased at the borders. The umbrella potential lowered not only the cone to paco transition state but also the paco to 1,2-alternate and paco to 1,3-alternate transition states. (In the 1,2-alternate conformation, either one of the phenol rings neighboring the rotated phenol of the paco is also rotated. In the 1,3-alternate conformation the opposite phenol ring is rotated.) Once a molecule reaches these alternate conformations in a simulation, it does not easily return to the cone or paco conformation. To avoid these problems, the umbrella potential was modified to

$$U(\mathbf{X}) = f(\xi) + f_2(\xi_2) + f_3(\xi_3) + f_4(\xi_4), \tag{4.12}$$

where $f(\xi)$ is the initial umbrella potential, and the three $f_i(\xi_i)$ $(i = 2,4)$ are Fermi−Dirac-like potentials depending on the angle between the annular plane and the phenol ring of the respective alternate reaction. Equations 4.8 and 4.9 were rewritten accordingly.

The probability distributions in a vacuum obtained with the minimum energy as umbrella were far from flat. For the *p-tert*-butyl-calix[4]arene we even had to use three windows to sample the whole range of ξ. The overall distributions were transformed into extra umbrella potentials according to eq. 4.5, and the systems were run again. This procedure was iterated both for the calix and the *p-tert*-butyl-calix[4]arene. The final simulations, with just one window covering all values of ξ, were continued for 18 and 19 ns for calix and *p-tert*-butyl-calix[4]arene respectively and gave flat distributions. The resulting free energy differences between transition state and cone well were 13.3 kcal/mol for a calix[4]arene and 13.9

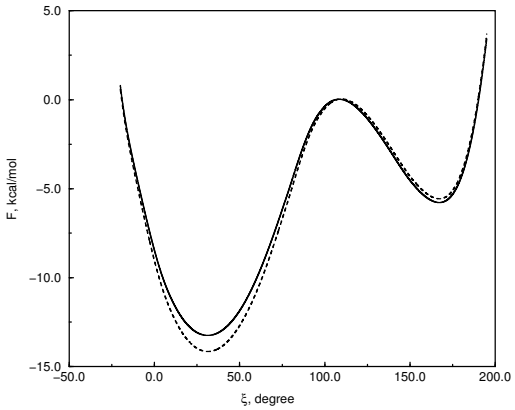

Figure 4.3: Free energy of a calix[4]arene in a vacuum (solid) and in chloroform (dashed).

kcal/mol for a *p-tert*-butyl-calix[4]arene, see Figs. 4.3 and 4.4.

The natural choice for the umbrella potential for the simulation of a calix[4]arene in chloroform was the umbrella potential that gave a flat distribution in a vacuum. The run with this umbrella lasted 16 ns. The distribution was transformed into a potential by eq. 4.5, and added to the existing umbrella. With this new umbrella the distribution was satisfactorily flat over 11 ns. The free energy difference between the transition state and the cone well was calculated to be 14.2 kcal/mol, see Fig. 4.3. The increase of this difference showed the same tendency as in previous works [36, 39]. We postpone the discussion of the conformational inversion rates until Section 4.5.

The first simulation of a *p-tert*-butyl-calix[4]arene in chloroform was also made with the final vacuum umbrella. This simulation was disastrous: it failed to satisfactorily sample the entire range of the reaction coordinate. The simple reason was that one of the chloroform molecules was caught in the cavity. As mentioned above, we resorted to two different methods to obtain the probability distribution of a *p-tert*-butyl-calix[4]arene in chloroform. In the window sampling approach the vacuum umbrella was used again as a first estimate, supplemented with ten different windowing potentials, which restricted the motion of ξ roughly to the range from $20°l - 40°$ to $20°l$, with l the number of the window. Because of the narrowness of the windows, the reaction coordinate sampled the whole width, be it with large

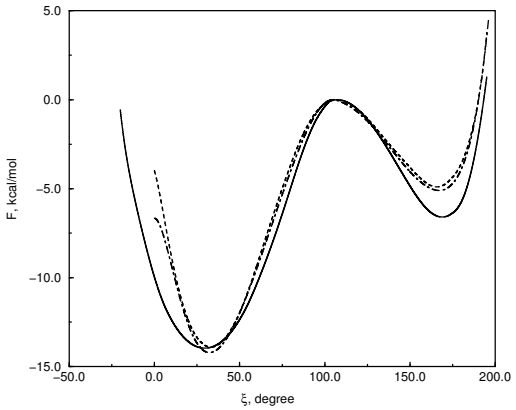

Figure 4.4: Free energy of a *p-tert*-butyl-calix[4]arene in a vacuum (solid) and in chloroform, obtained with windows umbrella sampling (dashed) and combined coupling parameter - umbrella sampling (dot-dashed).

variations within several of the $P_l(\xi)$. The large overlaps between neighboring windows were exploited to combine the ten individual distributions into a single overall distribution, which was then transformed into a new umbrella potential for the entire range of ξ. The ensuing distribution was not completely flat, and one more iteration step was taken. The final flat distribution was received by averaging over three runs with different start configurations, each run lasting 9.5 ns. The free energy difference between the transition plane and the cone state is 13.9 kcal/mol, see Fig. 4.4. This value was reproduced by the three individual runs to within 0.1 kcal/mol. We want to draw attention to the shift of the cone, transition and paco states with respect to their positions in a vacuum.

The second approach was to little by little turn on the interactions between the *p-tert*-butyl-calix[4]arene and the chloroform, whilst adjusting the umbrella potential at the same time to keep the distribution as flat as possible. We started from the situation $\lambda = 1$, denoting a complete lack of interactions between the *p-tert*-butyl-calix[4]arene and the solvent (but with full-blown interactions within the *p-tert*-butyl-calix[4]arene and within the chloroform). In this case the vacuum umbrella gave a flat distribution, of course. The value of λ was then decreased with steps of $\Delta\lambda = 0.1$. To accommodate the calix, a cavity had to be formed in the

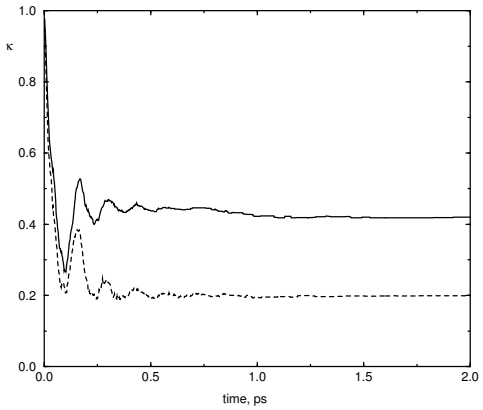

Figure 4.5: Transmission coefficients of a calix[4]arene in a vacuum (solid) and in chloroform (dashed).

chloroform, which was facilitated by the volume rescaling routine used to keep the system at a constant pressure. We used two different systems for the simulations from $\lambda = 0.9$ to $\lambda = 0.3$. When the distributions of both systems were found to agree with one another and did not change any more, the average distribution was transformed into the extra umbrella potential to be used for the next λ. The average time for each simulation was 7.5 ns. The simulations from $\lambda = 0.2$ to 0.0 followed the same procedure, with a third system added to increase the precision of the calculations, which were becoming slower because of the increased solvent interactions. The final flat distribution for $\lambda = 0$ was received from three runs with a duration of 9.5 ns each. The free energy difference between the transition plane and the cone state is 14.2 kcal/mol see Fig. 4.4. This value compares well with the 13.9 kcal/mol obtained by window umbrella sampling.

4.5 Conformational inversion rate

In the previous section the free energies of our systems were produced as functions of the reaction coordinate, $A(\xi)$. After the substitution of $A(\xi)$ in eq. 4.5, the reaction rate k_f^{TST} is easily calculated by eq. 4.1. The results are collected in Table 4.1 and Table 4.2. Here the

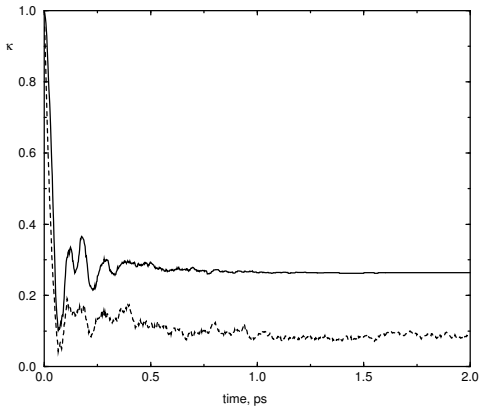

Figure 4.6: Transmission coefficients of a *p-tert*-butyl-calix[4]arene in a vacuum (solid) and in chloroform (dashed).

transition state , i.e. $\xi^{\neq}$, was defined as the value of ξ for which $A(\xi)$ reached a maximum. From a physical point of view, a value 10° to the left or to the right would have been equally justified, though it would have produced a different (higher) reaction rate, as explained before. To obtain the true reaction rate, we next calculated the transmission coefficient, see eq. 4.4. The first step was to create configurations belonging to the transition plane, which was done by constraining the reaction coordinate to $\xi^{\neq}$ during a simulation. The atomic coordinates were saved every picosecond. Next, 1000 relaxation runs were performed for each molecule to get the transmission function. These were started with the saved coordinates, combined with random velocities drawn from a velocity-weighted Maxwell−Boltzmann distribution [37]. The transmission coefficients reached their plateau values after about 1 ps, as depicted in Fig. 4.5 and Fig. 4.6.

The results for the calix[4]arene are shown in Table 4.1, those for the *p-tert*-butyl-calix[4]-arene in Table 4.2. In Table 4.1 we also included the simulation results from ref. [39], which were realized under the same conditions and with the identical force field, but with a different reaction coordinate. This difference led to a different free energy function and therefore to the difference between the transition state theory rates. It is noteworthy that, after multiplication by their respective transmission coefficients, the reaction rates k^{RF} are virtually identical.

Table 4.1: **Computed and experimental rates of calix[4]arene in vacuum and in chloroform.**

Solvent	k^{TST}, s^{-1}	κ	k^{RF}, s^{-1}	k^{exp}, s^{-1}
Vacuum[a]	481	0.42	202	
Vacuum[b]	241	0.92	222	
Chloroform[a]	110	0.20	22	8[c], 30[d]
Chloroform[b]	84	0.43	36	8[c], 30[d]

[a]This work. [b]Calculations by den Otter and Briels [39]. [c]Experimental results by Araki *et al.* [10]. [d]Experimental results by Gutsche and Bauer [70].

The conformational inversion rates are also in good agreement with the values obtained from experimental data. Gutsche and Bauer [70] measured a coalescence temperature with temperature-dependent ^{1}H NMR for the hydrogens connected to the hinge carbons, and derived the isomerization rate at this temperature from the chemical shift. They converted the rate into a free energy by

$$\Delta A^{\neq} = RT_{coalescence} \ln \left(\frac{6.62 \times 10^{12}}{k_{coalescence}} \right). \tag{4.13}$$

Araki *et al.* [10] measured the reaction rate as a function of temperature and obtained the free energy from an Arrhenius plot. Assuming that the free energy is independent of the temperature, we calculated the reaction rates at 300 K from the data provided in ref. [70] and ref. [10] by eq. 4.7. These rates correspond to the cone to inverted cone reaction (all four rings have rotated), because the intermediate conformations have too short a life-time to be detectable, and are therefore not directly comparable to our rates.

The inversion reaction consists of four steps, with one phenol ring rotating in each step [53]. These steps are independent, as the energy barriers between consecutive minima are much higher than k_BT. In schematic form,

$$\mathrm{C} \underset{k_2}{\overset{k_1}{\rightleftarrows}} \mathrm{P} \underset{k_4}{\overset{k_3}{\rightleftarrows}} \mathrm{A} \underset{k_3}{\overset{k_4}{\rightleftarrows}} \mathrm{P}' \underset{k_1}{\overset{k_2}{\rightleftarrows}} \mathrm{C}', \tag{4.14}$$

Table 4.2: **Computed and experimental rates of *p-tert*-butyl-calix[4]arene in vacuum and in chloroform.**

Solvent	k^{TST}, s^{-1}	κ	k^{RF}, s^{-1}	k^{exp}, s^{-1}
Vacuum[a]	151	0.26	39	
Chloroform, windows sampling[a]	234	0.09	20	3.6[b],12[c]
Chloroform, λ sampling[a]	151	0.09	13	3.6[b], 12[c]

.

[a]This work. [b]Experimental results by Araki *et al.* [10]. [c]Experimental results by Gutsche and Bauer [70]

where C, P and A denote the sum of all cone, paco and alternate conformations respectively, and where primes indicate conformations in which the majority of the phenol rings are pointing downward. Our calculations concern the rotation of *one* of the phenol rings of a cone. As there are four phenol rings, the overall cone-to-paco rate is four times higher, $k_1 = 4k^R F_f$. The calculated free energy functions can also be used to determine the reverse reaction rates, from paco to cone, which have the exact same transmission coefficients as the forward reactions. In this case the ordinal number of the rotating phenol is fixed by the particular paco conformation one is looking at, hence $k_2 = k^R F_r = 0.97 \cdot 10^8 s^{-1}$ for *p-tert*-butyl-calix[4]arene. Any paco can proceed to an alternate conformation through three different routes, by rotating the phenol ring to the left, to the right, or opposite to the rotated phenol ring of the paco. The latter reaction requires breaking up two hydrogen bonds, and the former two reactions require breaking up only one hydrogen bond and are therefore much quicker, $k_3 = k_3' + k_3''$. Because of the directionality of the hydrogen bonds, the rates of the two paco to 1,2-alternate reactions are different. Applying transition state theory to the free energy profile in a vacuum, we find $k_3' = 0.35 \cdot 10^8 s^{-1}$ and $k_3'' = 0.69 \cdot 10^8 s^{-1}$. Next, the set of coupled differential equations represented by eq. 4.14 is analytically solved to give five relaxation times, the largest of which corresponds to the inversion process. Inserting the above numerical values (k_4 is irrelevant), the final expression for the *p-tert*-butyl-calix[4]arene reads

$$k_{inv}^{exp} \approx 2k_f^{RF}. \tag{4.15}$$

An identical analysis of the calix, with k_2 though k_3 determined using the methods outlined above, yields [36, 39]

$$k_{inv}^{exp} \approx 3k_f^{RF}. \tag{4.16}$$

By inverting these equations, we arrive at the experimental rates listed in Table 4.1 and Table 4.2. They agree very well with our simulation results.

4.6 Structural analysis

The above numerical results show a mixed picture. On the one hand, the free energy curve of the calix is nearly identical in a vacuum and in solvent. The small differences and the reduced transmission coefficient do, however, reduce the conformational inversion rate in solvent by nearly an order of magnitude. On the other hand, the free energy profile of the *p-tert*-calix[4]arene has drastically changed in the solvent, but the final conformational inversion rate has gone down only by a factor of two to three. It is difficult to determine in which way exactly the interactions between the solute and the solvent, and the induced changes in the entropies and internal energies of the solute and the solvent, affect the reaction.

The interplay between solute and solvent can perhaps be better understood by studying the distribution of the solvent in the first solvation shell around the solute. In Fig. 4.7 scatter plots are given of the positions of the carbon atoms of the chloroform molecules in the vicinity of the *p-tert*-butyl-calix[4]arene. These plots were collected from simulations of about 1 ns each. The simulation of the cone was run with the normal force field, the paco required an extra potential to prevent the rare spontaneous transition to a cone, while the transition state could only be sampled by constraining the reaction coordinate. In the analysis, the translational and rotational displacements of the *p-tert*-butyl-calix[4]arene were calculated and the whole box was subjected to the same correction to keep the *p-tert*-butyl-calix[4]arene at a constant position and orientation, before the relative positions of the chloroforms were determined [37, 39]. Comparable plots for the calix[4]arene can be found in ref. [39]. Although a different reaction coordinate was used in those calculations, there are no discernible difference for the distributions around the transition state of the calix[4]arene. As the simulations of cone and paco do not depend on the reaction coordinate at all, they obviously are identical.

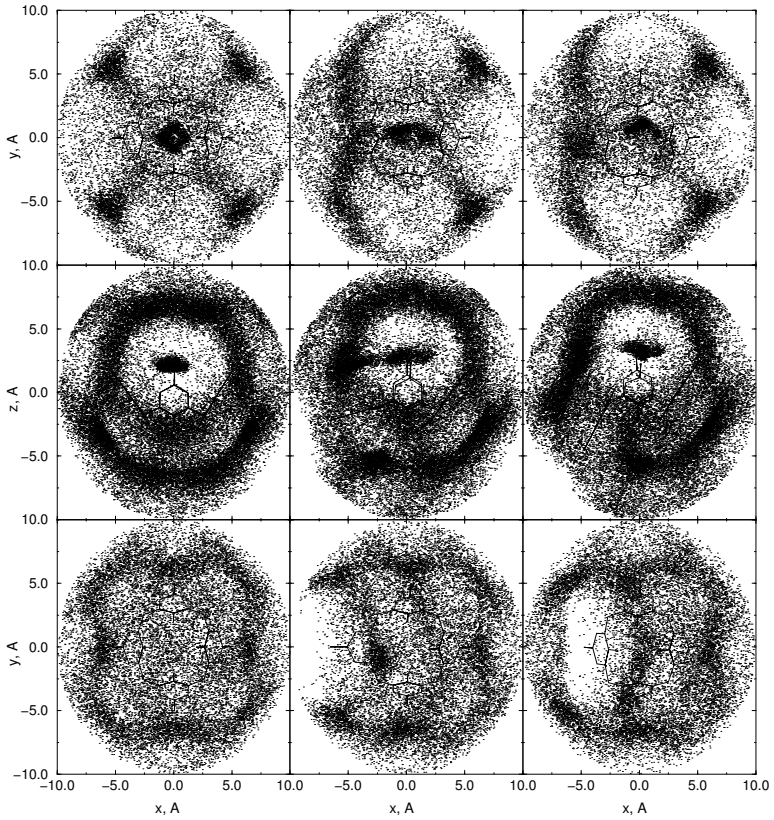

Figure 4.7: Density distributions of the carbon atoms of chloroform, after correcting for the orientation of the *p-tert*-butyl-calix[4]arene. From left to right are shown the cone, transition state, and paco conformation. The middle row gives a side view, the upper row a top view of the carbons with a positive z-coordinate, and the bottom row a top view of the carbons with a negative z-coordinate. The configurations shown are averaged over the simulation.

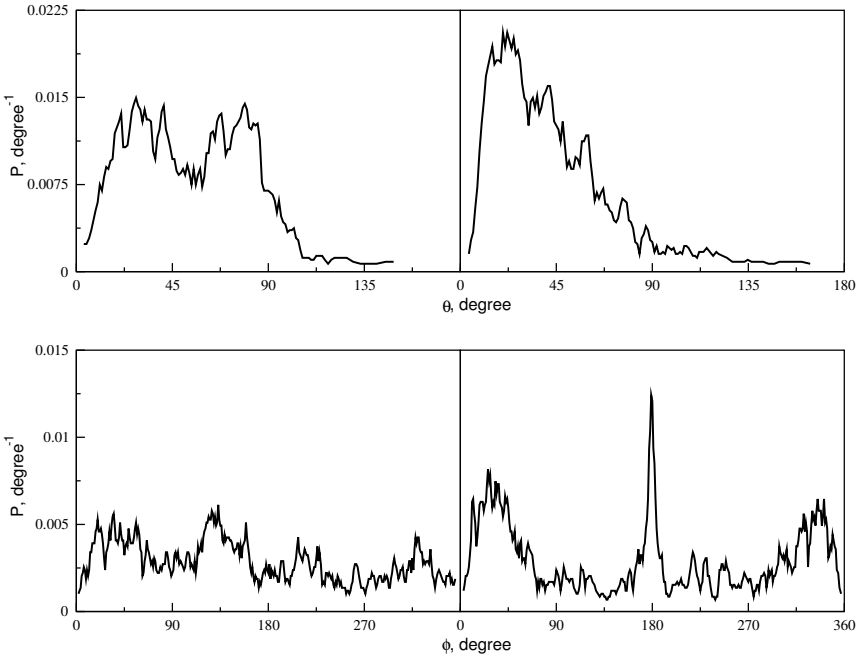

Figure 4.8: Probability distributions of the angles describing the orientation of the nearest chloroform molecule for the cone (left) and paco (right) conformations. Note that for a perfectly random distribution $P(\theta) \sim \sin(\theta)$ and $P(\phi)$ =constant.

The two top plots in the left column of Fig. 4.7 clearly show that the textitp-tert-butylcalix[4]arene in the cone configuration captures a chloroform inside its cavity. The radial distribution function of the chloroform around the cone, see Fig. 4.2, reveals a wide gap around 4.5 Å, suggesting that the captured chloroform molecule hardly ever escapes. This is also corroborated by the fact that in all simulations of a cone, one and the same chloroform was observed to reside within the cavity throughout the entire simulation. In the calix, on the other hand, there is a tendency for a chloroform to hover just above the calix, but this chloroform is exchanged regularly (about once every 0.5 ns) for another chloroform. Below both calixarenes, the polar hydroxyl groups are not capable of orienting the polar chloroform. The plots in the middle column and those in the right column show that the transition state

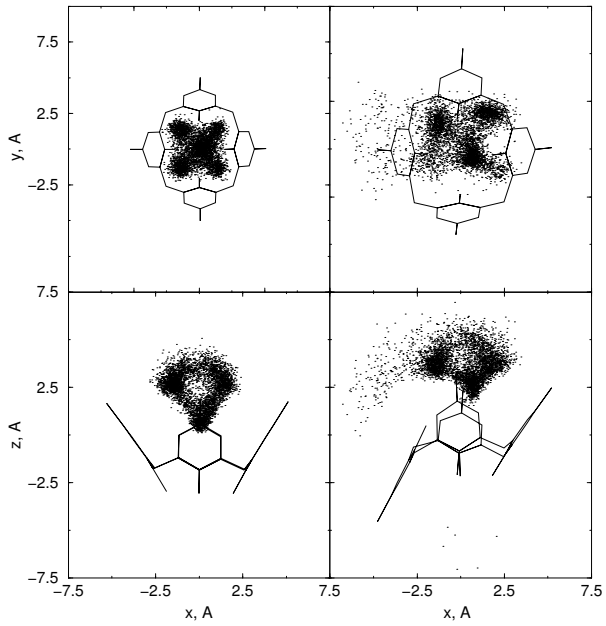

Figure 4.9: Density distributions of the chlorine atoms of the captured chloroformmolecule, in cone (left) and paco (right) conformations. The upper row gives a top view, and the bottom row a side view. The configurations shown are averaged over the simulation.

and the paco also induce quite some structure in the solvent, but they are not capable of immobilizing a chloroform.

The orientation of the chloroform molecule inside the cavity of the *p-tert*-butyl-calix[4]-arene can be described with two angles. The angle θ is defined as the angle between the vector **d**, pointing from a chloroform hydrogen to its carbon, and the normal vector **c** introduced earlier. Fig. 4.8 shows that the vector **d** is pointing downward with two preferred angles of approximately 25° and 75° for the cone conformation. The first maximum corresponds to an orientation with the hydrogen of the chloroform pointing towards the annulus, and the second maximum corresponds to an orientation with one of the chlorines pointing down. In X-ray diffraction experiments on the solid state of a complex of *p-tert*-butyl-calix[4]arene and chloroform, a value of 68° was found for θ at room temperature [15]. This corresponds well

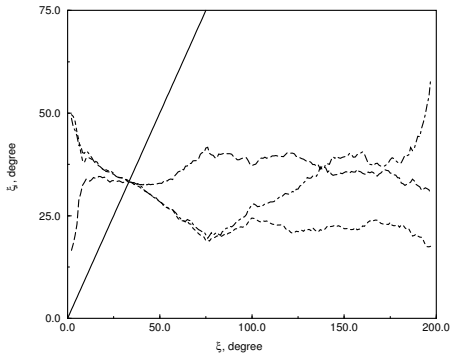

Figure 4.10: The equilibrium angles of the phenol rings to the right (dot-dashed), to the left (dashed) and opposite (long dashed) to the rotating phenol ring as functions of the reaction coordinate. The straight line denotes the rotating ring itself.

with our second peak, though it should be noted that the orientation in the solid state need not be identical with that in the liquid state. In further agreement with their findings, the top left plot in Fig. 4.7 shows that the carbon of the chloroform does not lie above the center of the calix. The second angle is obtained by projection **d** onto the annular plane of the calix, and calculating the angle ,ϕ between this projection and the coplanar vector $\mathbf{x_b} + \mathbf{x_c} - \mathbf{x_a} - \mathbf{x_d}$. Thus, an angle of 90° indicates that the hydrogen of the chloroform is directed toward the rotating phenol ring, 180° corresponds with the hydrogen directed at the neighboring phenol, to the left (at the top view), and so on. The captured molecule rotates freely inside the cavity of the cone conformer, as can be seen from the distribution of ϕ in Fig. 4.8.

Four-fold symmetry relating to the symmetry of the calix is visible, with maximum between the phenol rings. The density distribution of the chlorines of the captured chloroform reveals a similar symmetry, see Fig. 4.9, again with a preference for the positions directly above the hinge carbons. In the paco conformation the rotations of the chloroform are significantly reduced. Its hydrogen is predominantly directed at 25° with respect to the annulus. The in-plane distribution has only three peaks: one on either side of the ring to the left of the rotating ring and one directly at the ring to the right. Fig. 4.9 reveals that there are only three regions of high chlorine density left, all of which lie at the same side of the *p-tert*-butylcalix[4]arene.

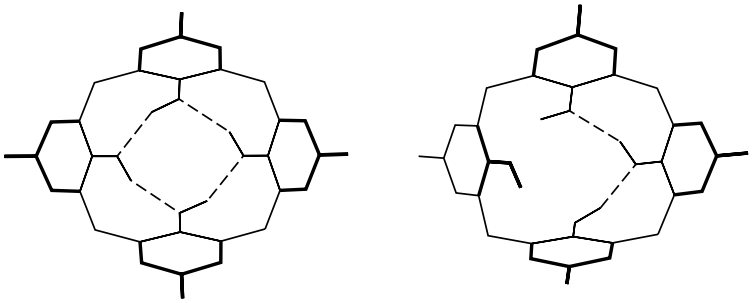

Figure 4.11: The cone (left) and paco (right) conformations with their hydrogen bonds at the lower rim.

As mentioned before, we introduced an angle for each of the three phenol rings besides the rotating phenol ring. The average values of these four angles are given in Fig. 4.10 as functions of the reaction coordinate. The rotations of the nonreacting phenol rings were limited to a maximum of 85° to avoid reactions to alternate conformations, a value seen here to lie far beyond the typical value of these angles. All lines intersect at 33°, which corresponds to the stable cone conformation. This conformation is symmetric because the four hydroxyl groups at the lower rim form a cyclic array of four hydrogen bonds, see Fig. 4.11. When the phenol ring rotates between 0° and 75°, the angles of its two neighboring rings are identical.

But as this ring rotates further, two hydrogen bonds are broken, see Fig. 4.10, and an asymmetric paco conformation is reached with the two neighbors (one a donor, one an acceptor) at different angles, see Fig. 4.11. In a vacuum the disparity between the two rings is already present, with equilibrium values of about 15° and 22°, respectively. The asymmetrical position of the chloroform enlarges this difference.

Auto- and cross-correlation function of the angles are depicted in Fig. 4.12 for the cone and paco conformations. The standard force field was used, supplemented in the case of the paco with a potential to prevent its transition to the cone conformation. Each run lasted 2 ns, with angles stored every 2 fs. For the cone there are only three distinct correlation functions, as expected from its symmetry. In agreement with Fig. 4.10, the transient correlation between any ring and its two neighboring rings is negative and bigger than that with its opposite ring. The correlations for the paco are all different, due to the lack of symmetry. The fluctuations of the angles are about 40% bigger in this case, as expected with the reduced number of hy-

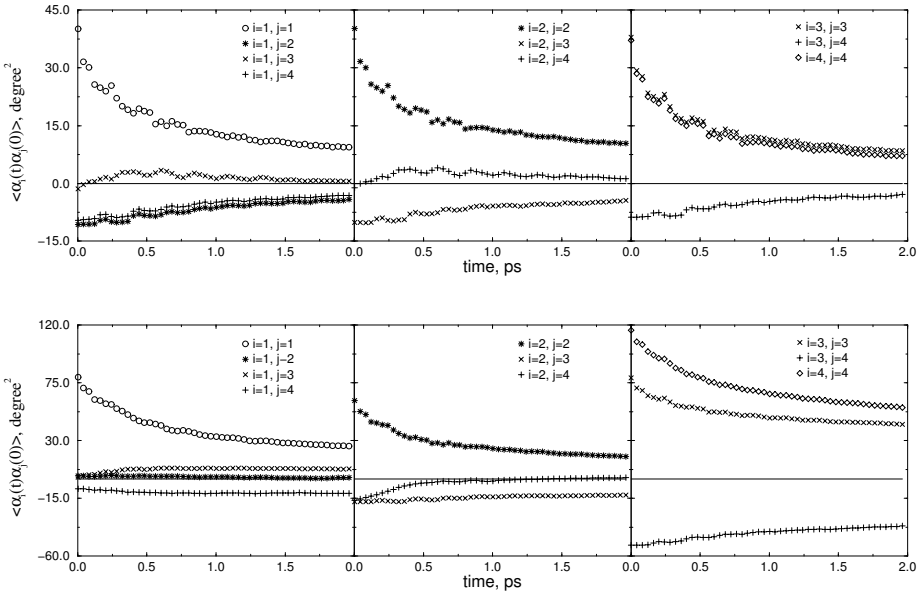

Figure 4.12: Correlation functions of the angles of phenol rings i and j, with $\alpha_i = \xi_i - \langle \xi_i \rangle$. The upper row gives the correlation functions for the cone conformation, the lower row for the paco.

drogen bonds. Surprisingly, the auto-correlations of rings 3 and 4 and their cross-correlation are slower than for the cone. From the small amplitudes of all cross-correlations, and the limited shift of the equilibria observed in Fig. 4.10, we conclude that the coupling between two rings is so weak that the isomerization steps in eq. 4.14 are independent.

Further insight into the reaction process is obtained from the average energies of the conformations. In a vacuum, the energy difference between cone and paco is $\Delta E^{vac} = \langle E^{vac}_{paco} \rangle - \langle E^{vac}_{cone} \rangle = 9.2$ kcal/mol. This difference is mainly due to Coulombic interactions, which account for 7.8 kcal/mol, and bending terms, 1.4 kcal/mol, with the remaining terms adding less than 0.7 kcal/mol each. The free energy difference between the two conformations is $\Delta A^{vac} = 7.4$ kcal/mol, implying that the entropy of the paco is higher by $\Delta S^{vac} = 6$ cal/(mol K). In chloroform the difference in the total energies has risen to $\Delta E^{sol} = 11.9$ kcal/mol, hence $\Delta\Delta E = 2.7$ kcal/mol. This rise is mainly due to an increase of the van der Waals interactions (including interactions with and within solvent) by $\Delta\Delta E^{vdw} = 3.5$ kcal/mol, while the Coulombic and bending terms dropped by 1.0 kcal/mol each. We think that these differences, which stabilize the cone with respect to the paco, arise mainly from the strong binding with the captured chloroform molecule. The solvent increased the free energy difference to $\Delta A^{sol} = 9.0$ kcal/mol ($\Delta\Delta A = 1.6$ kcal/mol). The entropy difference is therefore even larger in chloroform, $\Delta S^{sol} = 9.7$ kcal/mol ($\Delta\Delta S = 2.7$ cal/(mol K)), which we speculate is largely caused by the immobilization of one chloroform inside the cavity of the *p-tert*-butyl-calix[4]arene. The comparison of these results with quantum mechanical calculations, using a continuum model to represent the solvent [4] was given in *Chapter 3*.

4.7 Conclusions

The isomerization rates of calix[4]arene and *p-tert*-butyl-calix[4]arene in a vacuum and in chloroform have been studied with molecular dynamics simulations. Whereas the free energy as a function of the angle of the rotating phenol was relatively easily calculated for the former molecule, it proved much harder for the latter as it held on with tenacity to a chloroform molecule. Two methods were tried in the latter case: windows umbrella sampling and a combined coupling parameter – umbrella approach. Both methods coped well with the captured chloroform, their final free energy distributions being very similar, though the

combined coupling parameter – umbrella approach required much more time than windows umbrella sampling. The reactive flux method was used to obtain the rate constants. All rates are in good agreement with the experimental data. The conformational inversion rate of the calix[4]arene is close to the value previously calculated with a different reaction coordinate, illustrating the robustness of the reactive flux method.

5 Nucleation free energy of pore formation in an amphiphilic bilayer studied by molecular dynamics simulations

The formation of a pore in a membrane requires a considerable rearrangement of the amphiphilic molecules about to form the bilayer edge surrounding the pore, and hence is accompanied by a steep increase of the free energy. Recent rupture and conductance experiments suggest that this reshuffling process is also responsible for a small energy barrier that stabilises 'pre-pores' with diameters of less than one nanometer, rendering both the opening and closing of pores an activated process. We use the potential of mean constraint force (PMCF) method to study this free energy profile, as a function of pore radius, in a coarse grained bilayer model. The calculations shows that the free energy rises by 15 to 20 kT during pore opening, making it an extremely rare nucleation event. Although we do not observe a barrier to pore closure, the results do make the existence of such a barrier plausible. For larger pores we find a smooth transition to Litster's model, from which a line tension coefficient of about 3.7×10^{-11} Jm^{-1} is deduced. *

5.1 Introduction

Understanding biological processes in living cells is inextricably linked with the research of physical and mechanical properties of membranes isolating the cell from its environment and separating compartments within the cell. One of the most essential processes is the formation of pores in the presence of mechanical stresses. Subsequent leakage of the cell's contents and

∗ The work described in this chapter has been accpeted to J. Chem. Phys. [140].

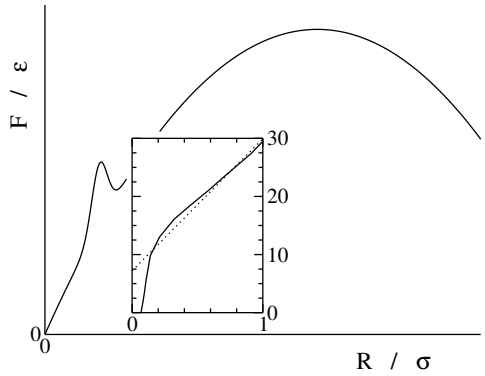

Figure 5.1: Sketch of free energy versus pore radius for a stretched membrane. The main peak is the traditional barrier to rupture, following Litster's mesoscopic model. Our focus is on the low R region, where a pore is being formed in a bilayer. Recent experiments propose a peak, which stabilises a pre-pore state, in this region. The insert shows the results of our calculations.

penetration of infectious agents through the pore can easily cause death to the cell, whereas their pivotal role in the fusion of cells, the possibility to insert medicinal molecules or to transport genes or ions across the membrane, give a positive meaning to pores in membranes. Thus, the study of pore formation in amphiphilic or lipid bilayers has attracted researchers for over thirty years.

The first theoretical expression for the free energy difference between an intact bilayer and an equally sized bilayer containing a pore was proposed by Litster in 1975 [90]. Litster assumed that this difference consists of an edge free energy $2\pi R k_C$ residing in the circumference of a circular pore of radius R, in combination with a reduction of the elastic surface energy by $\pi R^2\gamma$, where γ is the surface tension. This mesoscopic model predicts a maximum in the free energy of $\pi k_C^2/\gamma$ at $R = k_C/\gamma$, see Fig. 5.1. Pores with a smaller radius will eventually reseal, while larger pores grow indefinitely (rupture). Membranes are usually punctured by applying transmembrane electrical potential differences of a few hundreds of millivolts. By observing the dynamics of resealing of pores in phospholipid membranes, typical values of about $(0.5\text{ - }5)\times 10^{-11}$ N have been found for the line tension coefficient k_C [19, 23, 48, 159]. These values have been neatly reproduced by means of molecular dynamics simulations of an

atomistic model of DPPC membranes [88] as well as by a generic coarse grain model [141] suggested first by Goetz and Lipowsky [61, 62]. Similar values have been used as input in a mean field study of pore formation in diblock copolymer membranes [138] and in a network simulation of pore formation and rupture [124]. The latter process has been studied by us in *Chapter 6*, where we describe the dependence of the phase diagram of a punctured membrane on the size of the (zero tension) membrane. The model by Litster is sufficiently general to provide the basic language for a variety of pore-related membrane problems. For example, the stability of peptide induced pores in lipid membranes has been described [80, 89] by discussing the influence of the peptides on the line tension.

In *Chapter 6* we have described the presence of a barrier between the stable and metastable states of a stretched periodic flat membrane and its gross implications for puncturing and rupturing membranes. In that chapter, like in Litster's model, it was tacitly assumed that creating a pore in a membrane does not require any other work than the ones described by the elastic and the edge free energies, which actually only describes the thermodynamics of an already existing pore. It is obvious, however, that creating a pore requires different rearrangements of the amphiphiles than enlarging the circumference of an existing pore. In principle, therefore, Litster's model should be extended by adding a term proportional to the number of pores in the membrane. In cases where just one pore of mesoscopic size opens up, like in *Chapter 6*, this would have no consequences whatsoever on the thermodynamic description. Pore nucleation in itself, however, is a very important process for the functioning and treatment of living cells. Therefore, we have set out to study this process in greater detail.

The amphiphiles in an intact bilayer are all oriented more or less parallel to each other and perpendicular to the plane defined by the layer. Characteristic of a bilayer edge are tilted amphiphiles, whose heads form (in cross-section) a semi-circular surface with a radius comparable to the length of the molecule and whose tails point to the centre of this semi-circle, *i. e.* they are directed diagonally or even parallel to the membrane [90]. The rearrangements needed to go from one state to the other result in a free energy difference between the intact and the punctured membrane. If the reaction path proceeds along very unfavourable configurations, this could even lead to a free energy barrier between the two states, as depicted in Fig. 5.1 superimposed on the mesoscopic prediction. The existence of this additional pore nucleation barrier was stipulated by Evans *et al.* [46, 48] who refer to the state right after the

nucleation barrier as a closed metastable defect state. In a series of experiments these authors measured the distribution of rupture times after the onset of a gradually increasing stress in the membrane. Using a three state kinetic model based on the characteristics of Fig. 5.1, they were able to describe their data, thereby giving credibility to the existence of the hypothesised pore nucleation barrier. From their data it follows that the closed metastable defect in the case of lipid bilayers has a radius of about 0.6 nm. The height of the barrier is probably just a few k_BT, where k_B is Boltzmann's constant and T the temperature. Additional evidence for the stipulated nucleation barrier was provided by the conductance measurements of Melikov *et al.* [102], revealing that large ion conducting pores initially collapse to form nonconductive ($R < 1$ nm) easily reopenable pre-pores with lifetimes up to a few hundreds of milliseconds, before eventually closing completely.

Thus far, simulation studies of pore formation in bilayers have been limited to exposing the bilayer to an extremely high tension, or elongation, and awaiting the inevitable; free energy changes are not accessible in this set up. In this chapter we present the first simulation study of the free energy change during the reversible opening of a small pore in a bilayer. To this effect, we propose a method to calculate the free energy profile as a function of the pore radius, under any desired surface tension, and apply it to a coarse grained amphiphilic model for radii ranging from zero (*i. e.* the intact bilayer) upto the start of the mesoscopic regime. In Section 5.2 we describe the theoretical methods that we have used to perform these calculations, and in Section 5.3 we describe the simulation details. In Section 5.4 we present our main results, which we finally discuss in Section 5.5.

5.2 Theory

As discussed in the previous section, we assume that pore formation in amphiphilic bilayers is an activated process [46, 48]. The free energy landscape for such a process can be calculated by means of the potential of mean constraint force (PMCF) method usually applied to study rare events such as chemical and isomerisation reactions. This method allows one to obtain the free energy as a function of some reaction coordinate ξ separating products and reactants, even in cases where a high activation barrier renders the observation of a spontaneous transition extremely unlikely. In the case of pore formation in an amphiphilic bilayer, we consider

products and reactants to be the intact bilayer and the metastable pre-pore respectively. The specific choice of the reaction coordinate will be given in section 5.3.

In order to apply the PMCF method one has to fix the reaction coordinate throughout the simulation. Fixation of the reaction coordinate is achieved by adding a constraint to the Lagrangian of the free system,

$$\mathscr{L}_c(\Gamma,\dot{\Gamma}) = \mathscr{L}_f(\Gamma,\dot{\Gamma}) + \lambda_\xi(\xi(\Gamma) - \xi), \tag{5.1}$$

where Γ represents the coordinates of configuration space and $\dot{\Gamma}$ their velocities. The constraint on the reaction coordinate results in an additional force $\lambda_\xi \nabla_i \xi$ on the i^{th} particle. The value of the Lagrangian multiplier λ_ξ must be chosen such that the constraint $\xi(\Gamma) = \xi$ is met at any instant of the simulation, and may be calculated numerically, as for example in the SHAKE algorithm [121]. By doing so, the time derivative of the reaction coordinate automatically equals zero, $\dot{\xi} = 0$. The integral of $\langle\lambda_\xi\rangle_\xi$ with respect to ξ may be shown [106] to be the potential of mean constraint force (PMCF). The angular brackets denote a run time average, the subscript ξ indicates that the run is performed with the reaction coordinate mechanically constrained to the specific value ξ. It was conjectured by van Gunsteren [147] that this potential is approximately equal to the free energy of the reaction coordinate ξ,

$$F(\xi) = -k_B T \ln \int \delta[\xi(\Gamma) - \xi] \exp[-\beta H(\Gamma, P_\Gamma)]\, d\Gamma\, dP_\Gamma. \tag{5.2}$$

Here P_Γ represents the generalised momenta conjugate to the coordinates Γ, H denotes the Hamiltonian and $\beta = 1/k_B T$. Later it was shown by den Otter and Briels [38, 40, 41] that the difference between the two functions can be calculated from the same constrained simulation that needs to be performed to calculate $\langle\lambda_\xi\rangle_\xi$. Recently their result was rewritten to a much neater expression by Schlitter and Klähn [126]:

$$F(\xi) = \int_0^\xi \langle\lambda_\xi\rangle_\xi \, d\xi - k_B T \ln\langle Z_\xi^{-1/2}\rangle_\xi + F_0. \tag{5.3}$$

The second term on the right hand side is the metric tensor correction, with

$$Z_\xi = \sum_{i=1}^{N} \frac{1}{m_i} \nabla_i \xi \cdot \nabla_i \xi. \tag{5.4}$$

It represents the difference between the phase spaces sampled by a system that is mechanically constrained to $\xi(\Gamma) = \xi$, hence $\dot{\xi} = 0$, and by a system that is restricted to $\xi(\Gamma) = \xi$

without a limitation on the velocity $\dot{\xi}$, as in Eq. (5.2). The last term in Eq. (5.3) is an arbitrary constant F_0, whose choice will be indicated in Section 5.4.

5.3 Simulation details

In our simulation we have used a coarse-grained model introduced by Goetz and Lipowsky [62]. This model was successfully applied before to calculate the elastic modulus, bending modulus and edge free energy of an amphiphilic bilayer [42, 61, 141] and, with some minor changes, of a worm-like micelle [43]. Here we only give a brief description of this model. The amphiphiles consist of one head particle and four tail particles, the latter representing three to four CH_2 groups each. The solvent particles, representing two water molecules, are identical to the head particles. Most nonbonded interactions are modelled by the usual Lennard-Jones potential, $\Phi_{\mathrm{LJ}}(r) = 4\varepsilon[(r/\sigma)^{-12} - (r/\sigma)^{-6}]$, with σ = 1/3 nm and ε = 2 kJ/mol. Exceptions are the hydrophobic interactions between tail particles and head or water particles, which are mimicked by a purely repulsive soft core potential, $\Phi_{\mathrm{SC}}(r) = \varepsilon(r/\sigma_{\mathrm{SC}})^{-9}$, with $\sigma_{\mathrm{SC}} = 1.05\sigma$. These potentials are implemented in the 'shifted force' fashion, ensuring that both the potential and its first derivative vanish at the cut-off distance, $r_c = 2.5\sigma$. The particles of an amphiphilic molecule are held together by a harmonic bond potential, $\Phi_{\mathrm{bnd}}(l) = 5000\varepsilon\sigma^{-2}(l-l_0)^2$, with $l_0 = \sigma$, while an angle potential $\Phi_{\mathrm{ang}}(\phi) = 2\varepsilon[1-\cos(\phi)]$ introduces a bending stiffness between every set of three consecutively bonded particles. There are no dihedral potentials. All particles have the same mass m = 36 a.u., which combines with a number density of 2 particles per $3\sigma^3$ to a specific weight of just over 1000 kg/m^3. The temperature is 325 K, or $1.35\varepsilon/k_BT$, and is maintained by means of a Nosé-Hoover thermostat [56]. A time step of $\sqrt{m\sigma^2/\varepsilon}/500 \approx 2.8$ fs is used in the Verlet leap-frog integration scheme [56]. The simulations were performed with a tailored version of DL_POLY_2.0 [131].

The initial simulation boxes were created by constructing two parallel square lattice layers holding 24×24 straight amphiphilic molecules each, with their heads pointing outward, and by randomly adding 10 800 solvent particles. The bilayers were oriented parallel to the square xy face of the box. In the first box the sides $L_{\parallel}$ of this face were matched to produce a tensionless state, $L_{\parallel}^2 = A_0$, which for the current model amounts to an area [35] of $1218\sigma^2$.

The second box was slightly elongated, under constant volume, to $(L_\parallel^2 - A_0)/A_0 = 3.5\%$, exposing the bilayer to a surface tension large enough to cause rupture of large vesicles in experiments [48]. In order to cause spontaneous pore formation under simulation conditions, much larger tensions [88] or elongations [141] need to be applied, resulting in too large areas per head group to faithfully study the process of pore formation; an advantage of our method is that we do not have to stress the bilayer. It proves convenient to run the PMCF calculations at constant surface area, rather than at constant surface tension, as this avoids contributions from volume rescaling moves to the free energy, and from the constraint to the pressure. To minimise the effect of the area constraint on the density fluctuations within the bilayer, we have used a system that is large compared to the maximum pore area. Production runs typically lasted for 5 ns, and were preceded by thorough equilibrations.

Radii of pores were measured by means of a routine inspired by the Widom particle insertion method for measuring the chemical potential in a fluid [56], as described in *Chapter 6*. In a nutshell: the radius of a circular pore, measured from the centre of the pore to the centres of the amphiphilic particles in the edge, is directly related to the fraction f of randomly inserted test particles separated by more than $r_w = 1\sigma$ along the xy direction from any amphiphilic particle, $R = \sqrt{fL_\parallel^2/\pi} + r_w$. This routine was slightly changed to be able to measure radii of smaller pores. For this purpose, only distances to tail particles were taken into consideration and r_w was reduced to 0.6σ. These smaller test particles have a finite probability of being 'accepted' in an intact bilayer, which is easily corrected for by subtracting the appropriate average background from f. Radii are then calculated using $R = \sqrt{fL_\parallel^2/\pi} + r_f$. By fitting the new method to the previous one for large pore sizes we find $r_f = -0.25\sigma$, which compares favourably with the maximum value of $r_w - l_0 = -0.4\sigma$ suggested by the following simple geometrical consideration: In an idealised picture, the amphiphiles closest to the centre of the pore lie parallel to the plane of the bilayer, with their straight tails pointing away from the centre. If the head particles are at a distance R from the centre, the tail particles nearest to the pore are at $R + l_0$, and test particles are accepted upto $R + l_0 - r_w$. In a real system the tilt of the molecules, relative to the bilayer and to the radial direction, will reduce this distance.

Intuitively, the radius of a pore seems to be an appropriate reaction coordinate for the PMCF method. In order to be eligible as reaction coordinate, however, a coordinate must be a unique function of the configuration of the system, and the procedure used to calculate

the radii of pores does not provide such a function. Instead we propose to use as a reaction coordinate:

$$\xi = \frac{\Sigma - \Sigma_0}{\Sigma_M - \Sigma_0}, \tag{5.5}$$

where

$$\Sigma = \sum_{i=1}^{N} \tanh r_i. \tag{5.6}$$

Here $r_i = \sqrt{x_i^2 + y_i^2}$ is the distance, measured parallel to the bilayer plane, between the i^{th} tail particle and the centre of the pore, conveniently located at the origin of the coordinate system, and $N = 4068$ is the number of tail particles in the box. For values of r_i larger than $15\,\sigma$ we make a smooth transition from $\tanh r_i$ to one. In Eq. (5.6), Σ_0 is the average value of Σ obtained from unconstrained simulations with the appropriate box size, *i. e.* 4598.22 for the tensionless box and 4598.56 for the stretched box. Σ_M denotes the maximum value of Σ, reached when all tail particles are pushed away to distances larger than $15\,\sigma$, *i. e.* $\Sigma_M = 4608$. Note that this poses an upper limit to the range of the reaction coordinate.

With the above definition of the reaction coordinate, constraining ξ to a positive (negative) value is equivalent to decreasing (increasing) the particle density near the origin. We can thus impose onto the bilayer a localised density fluctuation large enough for a pore to form or to close, in a deterministic fashion. By integrating the required constraint force, see Eq. (5.3), we are able to determine the probability, $\propto \exp[-\beta F(\xi)]$, with which this density fluctuation would have occurred in a non-constrained equilibrium system. Thus, the pore does not have to open up spontaneously, which is an extremely unlikely and uncontrollable event in a simulation. Nor is there the need to put the bilayer under an elongational stress, while previous simulations of pore formation relied on extreme stresses to incite the system to form a pore within the alloted time. Constrained simulations were performed for ξ ranging from about -0.35 to nearly 1, storing the values of λ_ξ and Z_ξ at every time step.

5.4 Results

The effects on the bilayer of constraining the reaction coordinate are illustrated by the top views and cross sections depicted in Figs. 5.2 and 5.3 respectively.

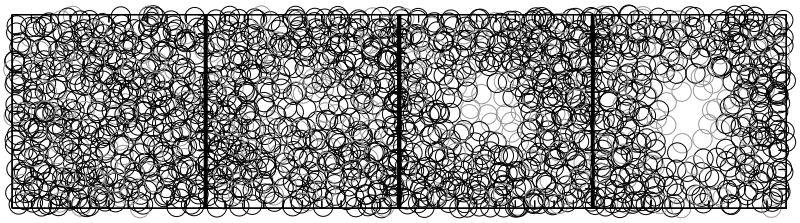

Figure 5.2: Top views of the centers of four amphiphilic bilayers, with the head particles in grey and the tail particles in black. The patches measure $10\sigma \times 10\sigma$, and depict the final configurations of runs at $\xi = 0$, 0.37, 0.80 and 0.92 (left to right). The particle insertion method does not detect a pore in the first two patches, while the latter two are determined at $R = 0.95$ and $1.48\,\sigma$. The circles are drawn to scale, solvent particles are omitted for clarity.

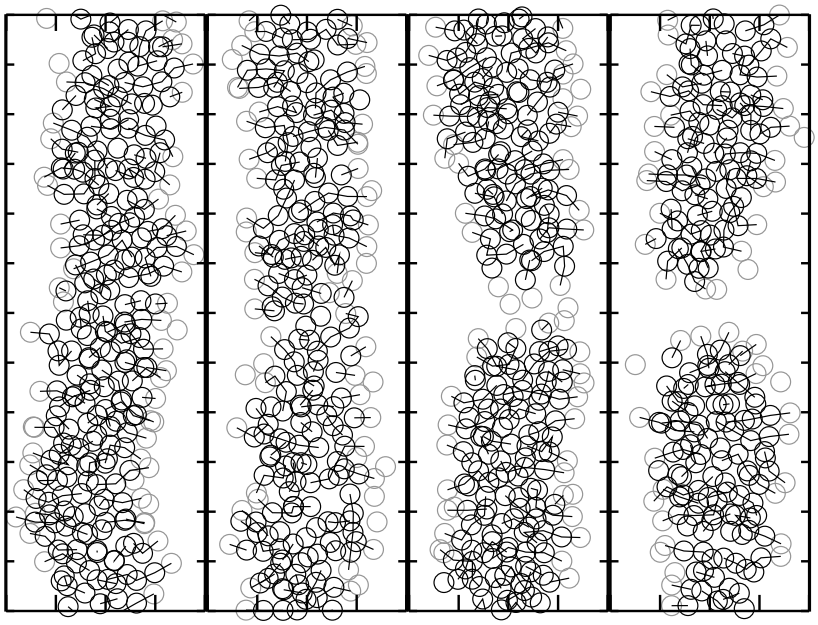

Figure 5.3: Cross sections of the four amphiphilic bilayers of Fig. 5.2, showing only those particles whose x coordinate lies within $1\,\sigma$ from the midplane. Head particles are grey, tail particles are black, and lines denote bonds between connected particles. The depicted areas measure $30\sigma \times 10\sigma$.

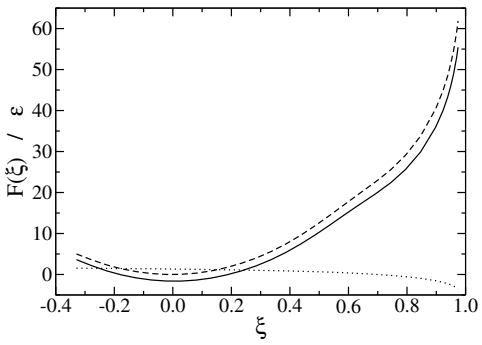

Figure 5.4: The calculated free energy profile as a function of the reaction coordinate ξ (solid line) for a tensionless membrane. Also shown are the integral of the Lagrange multiplier (PMCF, dashed) and the metric tensor correction (dotted) of Eq. (5.3).

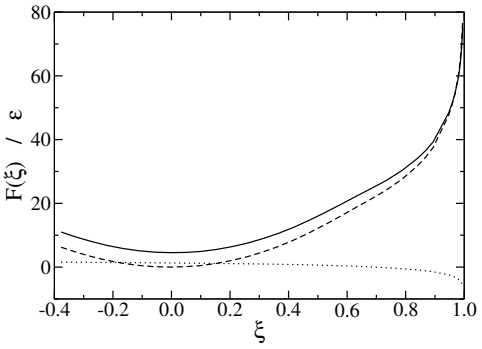

Figure 5.5: Same as Fig. 5.4, but for a bilayer under 3.5% elongation.

These, and many other snapshot we looked at, show that for low positive ξ the density of tail particles near the origin is reduced, while the bilayer remains intact. A further decrease of the density pulls the two layers of head particles locally towards each other. For $\xi \approx 0.55$ the layer of tail particles starts to develop a pore, which is filled with head particles entering from both sides. Next, the thermal motions of the head particles occasionally allow solvent particles to squeeze through the membrane. Finally, for ξ about 0.8, the head particles at opposite sides of the pore are pried apart, and a veritable transmembrane pore opens up. The radius of this pore continues to grow with increasing ξ. By decreasing the reaction coordinate we pass through the same phases in reverse order.

The free energies of pore formation as a function of ξ, as obtained by using Eq. (5.3), are shown in Figs. 5.4 and 5.5 for the tensionless membrane and for the membrane with a slight elongation of 3.5%, respectively. In both cases, the value of F_0 in Eq. (5.3) has been chosen such that

$$-k_B T \ln \int \exp\left[-\beta F(\xi, L_\parallel)\right] \, d\xi = \frac{1}{2} K_A A_0 \left(\frac{L_\parallel^2 - A_0}{A_0} \right)^2 . \tag{5.7}$$

The left hand side yields the total free energy of a square membrane with a given side $L_\parallel$,

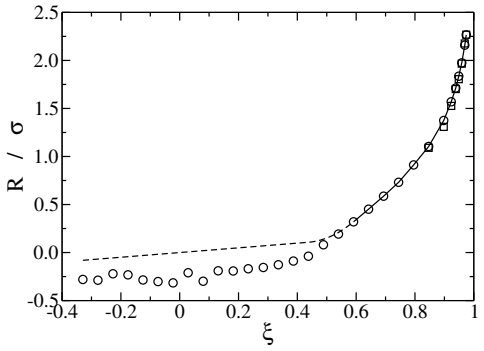

Figure 5.6: Average pore radius $\langle R \rangle_\xi$ as a function of the reaction coordinate ξ for the tensionless bilayer, calculated by the old (squares) and new (circles) particle insertion method. The constant and negative radii found for intact bilayers, $\xi < 0.5$, are artefacts of using an insertion method to detect a non-existing pore. The line, combining a fit to the data (solid) with a linear extrapolation to $R = 0$ at $\xi = 0$ (dashed), defines $R(\xi)$. The standard deviation in the radii is about $0.1\,\sigma$.

,

which for an elastic membrane is known to follow the expression on the right hand side. The elastic modulus K_A equals $8.2\,\varepsilon\sigma^{-2}$ or $250\,\mathrm{mJ\,m^{-2}}$ for the current model [35] and A_0 is the area of the tensionless bilayer introduced previously. Interestingly, both calculated free energies are nearly quadratic in ξ up to about 0.35. The figures also show the separate contributions of the integrated Lagrange multiplier and the metric tensor correction in Eq. (5.3).

In order to discuss our results in intuitively accessible terms, we would like to use the pore radius R as a reaction coordinate instead of ξ. To this end, we have calculated the average radius $\langle R \rangle_\xi$ as a function of ξ, and plotted the results in Fig. 5.6. While the old particle insertion method [141] is not capable of measuring pore radii less than about $1\,\sigma$, *i. e.* a pore just about big enough to fit a solvent particle, the modified method described in Section 5.3 can be applied to much smaller pores before it too becomes indiscriminate. We expect the latter approach to be accurate for R downto about $r_w - r_f = 0.35\sigma$, corresponding to a cavity the size of a test particle in the layer of tail particles – note that at this R the head particles form two closed layers, see Figs. 5.2 and 5.3. The drawn line in Fig. 5.6 is a fit for larger

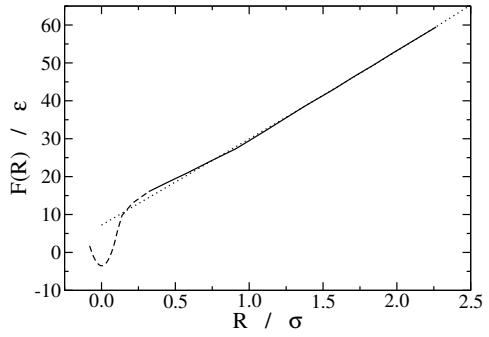

Figure 5.7: Free energy of a tensionless bilayer as a function of the pore radius. As in Fig. 5.6, the solid line denotes states with a detectable pore. The dotted region is based on an extrapolation, such that near the minimum of the curve R effectively measures the excess particle density around the origin. The dotted line is a fit to the mesoscopic theory of Eq. (5.9).

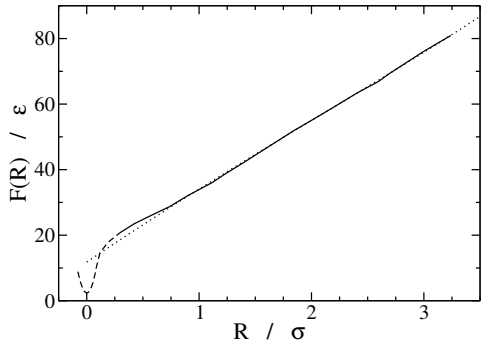

Figure 5.8: Same as Fig. 5.7, but for a bilayer under 3.5% elongation.

radii. Below $0.35\,\sigma$ we used a spline to make a smooth transition to a linear extrapolation running through $R = 0$ at $\xi = 0$, such that the derivative $dR/d\xi$ is continuous and differs from zero everywhere. The result is illustrated for the tensionless state by the dotted line in Fig. 5.6, and is virtually identical for the stretched system. Together they constitute our definition of a coordinate $R = R(\xi)$, completely defined by ξ and therefore well defined for any configuration Γ. Since R is equal to the radius of a pore in those cases where a radius is well defined, and otherwise is a smooth extrapolation to $R = 0$ for the unconstrained intact membrane, we henceforth call it the radius of a pore. Note that for small radii our definition of R is proportional to Σ, and hence to the tail particle density near the origin.

Using this definition of R, we have calculated the free energy from

$$\begin{aligned} F(R) &= -k_B T \ln \int \delta\left[R(\Gamma) - R\right] \exp\left[-\beta H(\Gamma, P_\Gamma)\right] d\Gamma\, dP_\Gamma \\ &= F(\xi) + k_B T \ln \frac{dR}{d\xi} \end{aligned} \tag{5.8}$$

and plotted the result in Fig. 5.7 for the tensionless membrane and in Fig. 5.8 for the slightly stretched membrane. In order to comply with our previous use, we have represented $F(R)$ by a drawn line for those values of R which correspond to measurable radii and by a dashed line where R is defined by extrapolation. For the larger values of R the free energies should be describable by a mesoscopic model like Litster's, augmented with an additive term resulting from the nucleation of a pore. For a punctured membrane with fixed lateral dimensions, as opposed to the fixed tension case considered by Litster, this free energy reads [141]

$$F(R,L_{\|}) = \frac{K_A}{2A_0}\left(L_{\|}^2 - \pi R^2 - A_0\right)^2 + 2\pi k_C R + F_{\mathrm{nucl}}(L_{\|}). \tag{5.9}$$

The dotted lines in Figs. 5.7 and 5.8 represent fits of this equation to our results. The contribution from the surface elasticity is small, suggesting that the area constraint does not restrict density fluctuations very much. From the fits we obtained $k_C = 3.62$ and $3.69\,\varepsilon\sigma^{-1}$ for the tensionless and stretched box respectively, and $F_{\mathrm{nucl}} = 7.2$ and $5.7\,\varepsilon$ respectively. Not only are the two values of k_C almost identical, they are also consistent with the ones obtained in our previous simulations of large stable pores [141]. The method described in the present chapter has the advantage over the one in *Chapter 6* that it can be applied to much smaller simulation boxes, which may be a necessity when atomistic models are used.

5.5 Discussion and conclusions

We have presented a method to calculate the change in free energy of an amphiphilic bilayer during the opening of a pore, and applied it to a coarse grained model mimicking lipid bilayers. Previous pore opening simulations had to rely on the unpredictable spontaneous opening of a pore, which necessitated a high surface tension and which ruled out a determination of the relevant free energy changes. By means of a constrained reaction coordinate, we are able to smoothly open and close a pore, regardless of the surface tension, allowing a direct evaluation the the free energy profile. Unlike in most previous free energy calculations, the constrained reaction coordinate is chosen not on the basis of some geometrical property (for example, a bond length or an angle), but such as to allow control of the density of tail particles within a given distance from the centre of the membrane. It is interesting to note that this reaction coordinate gives rise to rather large entropic correction terms describing the

difference between the potential of mean constraint force (PMCF) and the true free energy function. Whereas usually these corrections amount to less than 1% of the final free energy difference, in the present case they were as large as 10%.

For the larger pore radii, $R > 1\sigma$, we obtained an excellent match of the calculated free energy profile with a mesoscopic model similar to Litster's model, for a line tension coefficient equal to $3.7\,\varepsilon\sigma^{-1}$ or about $3.7\times10^{-11}\,\mathrm{Jm}^{-1}$. This results lies in the range of experimentally observed values, and is in good agreement with an earlier study [141] in which the line tension coefficient of the same system was obtained by comparing pore radii of much larger stable pores under various elongations to the predictions of the mesoscopic model, Eq. (5.9). Remarkably, the mesoscopic free energy expression holds for these rather small pores, with a line tension coefficient that is virtually independent of the curvature R of the edge.

For the intact bilayer, *i. e.* $R \approx 0$, the quadratic minima in the free energy curves measure the probability distributions of small local density fluctuations. The standard deviations calculated from these free energy functions coincide with those obtained from thermal fluctuations in unconstrained equilibrium simulations. Beyond the thermal range the free energies rise rapidly, upto some $15\,k_BT$ at $R \approx 0.25\,\sigma$. With increasing values of R, tail particles are gradually expelled from the centre of the bilayer, thereby strongly reducing the thickness of the bilayer at the origin for $R = 0.25\,\sigma$. By pushing the tail particles away from the centre, the amphiphilic molecules involved in this process, choose to tilt in order to continue to shield the remaining tail particles from the solvent. At $R \approx 0.75\,\sigma$ a pore-like state is obtained in which diametrically opposed head particles start to lose contact. At the pre-pore state the free energy of the bilayer has risen by some $25\,\varepsilon$, or $18\,k_BT$, over the collective free energy of the intact bilayer, making pore formation a rare, activated process. For even larger radii we observe a transition to the mesoscopic regime, as discussed above.

The calculated free energy profile does not contain an activation barrier to pore closure as expected on intuitive grounds and as invoked by Evans *et al.* [46, 48] and Melikov *et al.* [102] to explain their experimental results. Since the coarse grained model faithfully reproduced a number of bilayer properties to within the experimental range, notably the elastic modulus, bending rigidity and edge free energy coefficient, this result was unexpected. Despite the absence of a metastable pre-pore state, the current profile with its pronounced barriers to pore formation and to rupture may be expected to have a similar, albeit much less pronounced,

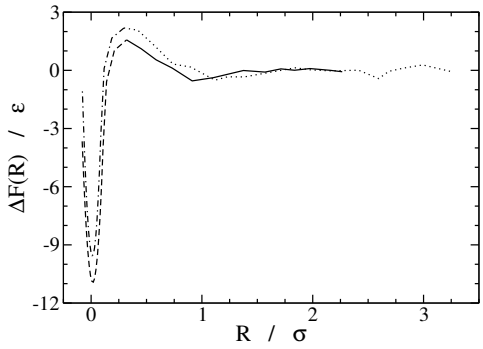

Figure 5.9: Differences between the exact free energy functions and the mesoscopic theory of Eq. (5.9), for the tensionless (solid and dashed) and the stretched (dotted and dash-dotted) membrane. For reference, the average thermal energy, k_BT, equals $1.35\,\varepsilon$.

influence on the rupture dynamics of stressed intact membranes as the three state model used by Evans *et al.* In order to emphasise the influence of the particular rearrangements of the amphiphiles needed to create a pore, we have plotted in Fig. 5.9 the difference between the exact free energy and the mesoscopic representation given in Eq. (5.7). This plot reveals that, contrary to the full free energy, the contribution resulting from pore creation does go through a maximum and that for values of R equal to about $1\,\sigma$ (or 1/3 nm) a pre-pore has developed. The differences are similar for the tensionless and the stretched membrane, with the latter having a slightly higher maximum, suggesting that the effect of tension is limited. Although the height of the maximum in Fig. 5.9 is not large enough to create a local maximum in the total free energy, we nevertheless feel that our results add to the credibility of a metastable pre-pore state as hypothesised by Evans *et al.* Assuming that the current difference plot also applies to a bilayer with a smaller edge energy coefficient, like the $6\times10^{-12}\,\mathrm{Jm}^{-1}$ or $0.6\,\varepsilon\sigma^{-1}$ reported by Evans *et al.* [48], the bilayer would have had a metastable pore. It is probable that the energy and entropy of the amphiphilic rearrangements needed to create a pore are not sufficiently well described by a coarse grained model. An atomistic model, possible in combination with a different amphiphilic architecture, will probably produce a more pronounced barrier.

6 Simulations of stable pores in membranes - system size dependence and line tension

Amphiphilic bilayers with a pore were simulated using a coarse grained model. By stretching the bilayer to 70% beyond its equilibrium surface area, we established the phase diagram of pores, identifying regions where pores are stable, metastable or unstable. A simple theoretical model is proposed to explain the phase diagram, and to calculate the critical and equilibrium relative stretches. Interestingly, these are found to scale with the inverse cubic root of the number of amphiphiles in the bilayer, thus explaining the order of magnitude difference between the simulated and the measured values. Three different methods are used to calculate a line tension coefficient of $(3.5 - 4.0) \times 10^{-11}$ *J/m, in good agreement with experimental data.* *

6.1 Introduction

Bilayers of amphiphiles or lipids are of great importance to living tissues, where they serve as the membranes surrounding cells and compartments within cells [137]. The formation of a pore in a bilayer, *e. g.* when the membrane is exposed to a mechanical stress, can have dire consequences for the cell: its contents can leak out and infective agents can sneak in, which could ultimately prove fatal. On the positive side, pores play a crucial role in the fusion of membranes, the transport of ions across the membrane, and they are convenient when inserting medicinal molecules or genes into the cell. These realisations drive the ongoing

∗ The work described in this chapter has been accpeted to J. Chem. Phys. [141].

research in amphiphilic bilayers, and of pores in particular.

Several experimental techniques are available for producing a pore in a bilayer, usually the taut membrane of a swollen vesicle, including exposure to mechanical stress [49] or a strong electric field (electroporation) [102], optical illumination [123], imploding bubbles [97], adhesion at a substrate [123], optical tweezers [14] and puncturing by a sharp tip [91]. The resulting pore is usually short-lived, as either the structurally weakened bilayer succumbs to the prevailing surface tension, or the line tension causes the pore to close rapidly. The latter transient pores usually give themselves away only by the (dyed) material that flows through the pore before closure. Over the last decade some ingenious techniques have been developed to significantly extend their life time, namely by performing the experiment in a highly viscous solvent [123], or by using aspiration into a micropipet to maintain a surface tension that can balance the line tension [159]. From these and other measurements, line tensions ranging from 0.5 to 5×10^{-11} J/m have been reported [23, 49, 91, 105, 159].

Pores have also been studied using molecular dynamics simulations. Some authors have run simulations in full atomistic detail [98, 139, 158], but it is more common to resort to coarse grained models [52, 64, 92, 107, 109] as they allow for larger system sizes and longer simulation times. Other computer simulations have modelled membranes with pores as a fluid network in which vertices can be broken and formed [128], or by density functional calculations of a bilayer exchanging amphiphiles with the surrounding solvent [108, 138]. The overall picture that emerges from the molecular dynamics simulations is that transient pores appear and disappear spontaneously, at low or vanishing surface tension, either if the line tension of the amphiphilic model is low [52, 92], or if the bilayer is weakened by defects such as a stalk [107, 109] or additives [64]. Intact bilayers with large line tensions can withstand large relative stretchings (see [64] and this work) or lateral pressures [139] before a pore opens, while considerably smaller stretchings or pressures are required to keep an existing pore open. The actual numerical values stand in sharp contrast to the experimental data, where relative stretchings of an order of magnitude less are found to suffice [86, 159]. The scaling of this property with system size constitutes an important part of the present research.

In the theoretical model of Litster [90], the free energy difference between an intact bilayer and one containing a pore of radius R is given by $\Delta F = 2\pi R\Gamma - \pi R^2\gamma$, where γ and Γ are known as the surface and line tensions respectively. From the model it follows that

pores reseal if their radius lies below a critical radius $R^* = \Gamma/\gamma$, corresponding to a maximum in ΔF, while larger pores grow indefinitely. Some of the above experiments are in conflict with the latter prediction, however, because pores larger than R^* have been observed to reseal [123, 159]. Moreover, in some simulation studies large pores were even found to be stable (at least, over the time scale available in the study). Since in these simulations the stretchings are quite large, and the chemical potential is not among the control parameters, we prefer an elastic interpretation of the free energy of the bilayer [52, 133]. In a Taylor expansion of our model in the limit of small stretchings, the two leading terms are of the same form as in Litster's model. Most other theoretical studies of pores in bilayers have focused on the actual formation process of pores, as thermal fluctuations surmounting an activation barrier [55, 60, 127], a process we will not study here.

The remainder of the chapter is organised as follows: in Section 6.2 we describe the details of our model, and the algorithm used in the determination of the pore radius. Simulation results and theory alternate in Section 6.3, where three different approaches are taken towards calculating the line tension coefficient. Our main results are summarised and discussed in Section 6.4.

6.2 Simulation details

Amphiphiles and solvent molecules were represented with a coarse-grained model introduced by Goetz and Lipowsky [61, 62], inspired by the work of Smit *et al.* [129] in the early nineties. We restrict ourselves to a very brief description of this model. Each amphiphile consists of one head particle and four tail particles, the latter representing three to four CH_2 groups each. Solvent particles, representing two water molecules, are identical to head particles. Nonbonded interactions are modelled by the usual Lennard-Jones potential, $\Phi_{\mathrm{LJ}}(r) = 4\varepsilon[(r/\sigma)^{-12} - (r/\sigma)^{-6}]$, where $\sigma = 1/3\,\mathrm{nm}$ and $\varepsilon = 2\,\mathrm{kJ/mol}$, with the exception of the hydrophobic interactions between tail particles and head or water particles, which are described by purely repulsive soft core potentials, $\Phi_{\mathrm{SC}}(r) = \varepsilon(r/\sigma_{\mathrm{SC}})^{-9}$, where $\sigma_{\mathrm{SC}} = 1.05\,\sigma$. All potentials are assumed to be of the 'shifted force' type, ensuring that both the potential and its first derivative vanish at the cut-off distance, $r_c = 2.5\,\sigma$. The particles of an amphiphilic molecule are held together by harmonic springs, $\Phi_{\mathrm{bnd}}(l) = 5000\varepsilon\sigma^{-2}(l-\sigma)^2$, while bond-

angle dependent potentials $\Phi_{\text{ang}}(\phi) = 2\varepsilon[1 - \cos(\phi)]$ introduce a bending stiffness between every set of three consecutively bonded particles. There are no dihedral potentials. All particles have the same mass $m = 36$ a.u., which combines with a number density of 2 particles per $3\,\sigma^3$ to a specific weight of just over $1000\,\text{kg/m}^3$.

The equilibrium surface area per amphiphile a_0 and the compressibility modulus K_A for the above model were calculated by den Otter and Briels [42]. After having corrected a slight mistake, we have calculated these properties again and found $a_0 = 2.12\,\sigma^2$ or $23.5\,\text{Å}^2$ and $K_A = 8.2\,\varepsilon\sigma^{-2}$ or $250\,\text{mJ m}^{-2}$ for the system size used here [35], in good agreement with Goetz and Lipowsky [61] and with experimental results.

The simulation boxes contained 1152 amphiphiles and 10 800 solvent particles. Starting configurations were made by first constructing two parallel square lattice layers, containing one (zero in the case of an intact bilayer) nearly circular pore in the middle. Each layer consisted of 576 straight amphiphilic molecules with their heads pointing outward. Lattice constants were chosen such that the periodic simulation boxes had predescribed total areas $L_\parallel^2$. Next, the boxes were filled randomly with 10 800 water particles. Perpendicular box dimensions $L_\perp$ were chosen such that in all cases a number density of 2 particles per $3\,\sigma^3$ was obtained. All simulations were done at constant (N,V,T). The temperature was 325 K, or $1.35\,\varepsilon/k_B$, in all cases and was maintained by means of a Nosé-Hoover thermostat. The simulations were executed with a slightly adapted DL_POLY_2.0 package [131], using the Verlet leap-frog integration scheme with a time step of $\sqrt{m\sigma^2/\varepsilon}/500 \approx 2.8\,\text{fs}$.

Each system was run long enough to reach a free energy minimum corresponding to a stable pore or a meta-stable pore. Pore areas were measured using a method inspired by the Widom particle insertion method for measuring chemical potentials [56], The amphiphilic particles constituting a bilayer (heads and tails) were projected onto the basal plane and test particles were randomly inserted in this plane. Those test particles which had no amphiphilic neighbours within a distance of $r_{\text{cw}} = 1.0\,\sigma$ were 'accepted', while the others were 'rejected'. After $M = 25\,000$ insertions, the area A_h of the pore was calculated according to

$$A_h = L_\parallel^2 \frac{M_{\text{acc}}}{M}, \tag{6.1}$$

where $L_\parallel$ is the length of the simulation box parallel to the bilayer and M_{acc} is the number of accepted particles. Using a routine to identify clusters [136], we verified the connectivity of the accepted test particles. In this way we detected occasional outliers, but never a secondary

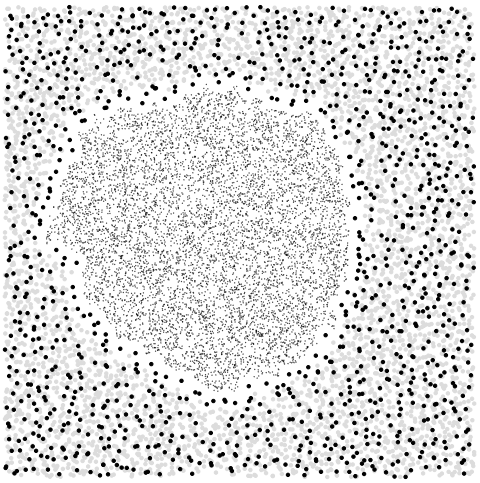

Figure 6.1: Top view of a bilayer with a pore. The large black dots stand for head particles and the large grey dots for tail particles. The 'accepted' Widom test particles (see Section 6.2) are plotted as small black dots. Note the strip of 1 σ width between the outermost accepted test particles and the head particles forming the rim of the pore.

pore of any significant size or life time. A typical example of the distribution of accepted particles is given in Fig. 6.1. The average ratio of the eigenvalues of the inertia tensor of the cloud of accepted particles was found to be $\langle I_{xx}/I_{yy}\rangle \approx 1.28$. Considering that an ellipse of this particular shape has a circumference only 1 % larger than that of a circle with the same area, we are justified in assuming henceforth that pores are circular. Radii of pores were calculated as $R = \sqrt{(A_h/\pi)} + 1$, where the addition of one takes into account the width r_{cw} of the Widom test particles, see Fig. 6.1.

6.3 Theory and results

In this section we present the results of our simulations along with some theoretical expressions needed to interpret these results.

In our theoretical considerations we assume that all of our membranes are flat and that contributions to their free energies from fluctuating undulations may be neglected. The free energy of a periodic square bilayer of length $L_{\|}$, containing a circular pore of radius R, then

reads

$$F = \frac{K_A}{2A_0}\left(L_\parallel^2 - \pi R^2 - A_0\right)^2 + 2\pi k_C R. \tag{6.2}$$

The first term accounts for elastic deformations of the membrane, where $A_0 = Na_0/2 = 1218\,\sigma^2$ is the area of the tensionless membrane without a pore. The last term represents the edge free energy due to the circumference of the pore; k_C is the free energy per unit length of edge and will be called the line tension coefficient. Some examples of the free energies as a function of the radius of the pore are displayed in Fig. 6.2 for several values of the relative stretch $(L_\parallel^2 - A_0)/A_0$; the value of k_C has been chosen equal to the one that we will finally find to describe our data.

6.3.1 Phase diagram

In this subsection we describe the phase diagram representing the radius of the pore in a punctured membrane as a function of the relative amount of stretching.

We have simulated a number of punctured periodic membranes with different relative stretchings for sufficiently long times for the systems to settle in stable or metastable equilibrium states. For the larger values of stretching this resulted in the presence of pores with well defined radii, while for the smaller stretchings the initially created pores disappeared. The results of our simulations are represented by the symbols in the phase diagram of Fig. 6.3.

From a theoretical point of view, the final states of our simulation boxes correspond to local minima of the free energies as functions of the pore radius R for the given values of relative stretchings. Taking the derivative with respect to R of the free energy given in Eq. (6.2), and equating it to zero, we obtain after some rewriting

$$\frac{L_\parallel^2 - A_0}{A_0} = \pi\frac{R^2}{A_0} + \frac{k_C}{K_A}\frac{1}{R}. \tag{6.3}$$

As can be seen in Fig. 6.2, for relative stretchings larger than some critical value this equation has three roots, one of which is negative and two of which are positive. The two positive roots, corresponding to a maximum and a minimum of the free energy respectively,

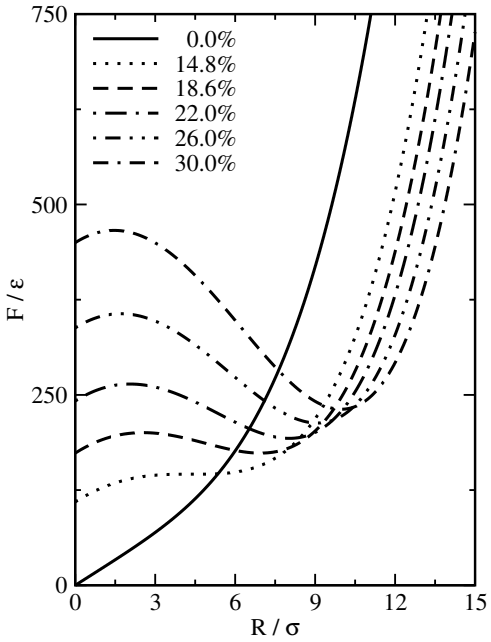

Figure 6.2: Theoretical free energy curves F, see Eq. (6.2), as a function of the pore radius R, for various relative stretchings of the bilayer. The numerical values of K_A, A_0 and k_C are those of the bilayer studied here.

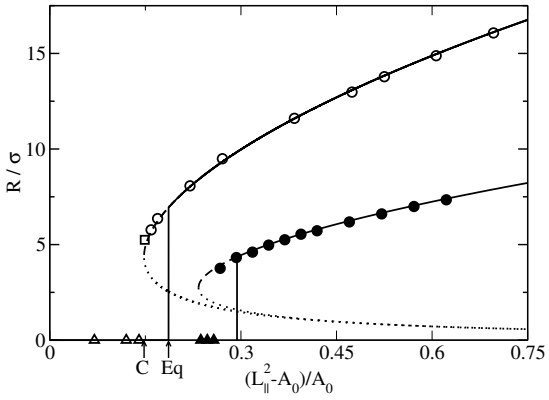

Figure 6.3: Average pore radius as a function of the relative stretch for a bilayer of 1152 amphiphiles (outer lines, open symbols) and for one of 288 amphiphiles (inner lines, solid symbols). Stable pores are marked by circles. The square denotes the average radius, before closure, of an metastable pore. Unstable pores that closed within 10 ns are denoted by triangles. The drawn lines representing the theoretically predicted stable states, see Eq. (6.4), were obtained by fitting the data of the bigger bilayer, with k_C as the only free parameter. The dashed lines give the metastable states, and the dotted lines the location of the activation barrier. The equilibrium and critical relative stretches of the large bilayer are marked by arrows.

are given by

$$R_{\min} = 2\left(\frac{L_\parallel^2 - A_0}{3\pi}\right)^{1/2} \cos\left(\frac{\alpha}{3}\right), \tag{6.4}$$

$$R_{\max} = -2\left(\frac{L_\parallel^2 - A_0}{3\pi}\right)^{1/2} \cos\left(\frac{\alpha+\pi}{3}\right), \tag{6.5}$$

where

$$\cos(\alpha) = -\frac{k_C}{2K_A}\frac{A_0}{\pi}\left(\frac{L_\parallel^2 - A_0}{3\pi}\right)^{-3/2}. \tag{6.6}$$

Fitting the first of these to our simulation results, see Fig. 6.3, we found the line tension

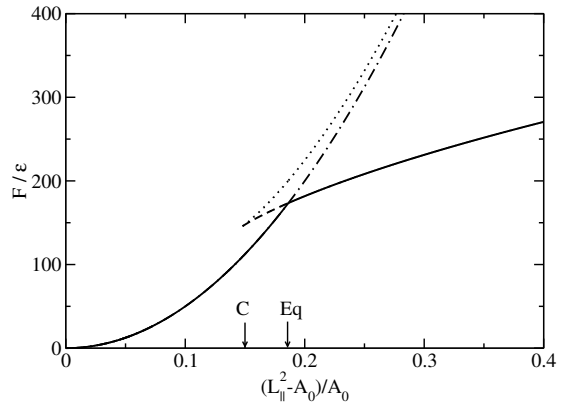

Figure 6.4: The local minima and maxima of the free energy of the intact bilayer and of the punctured bilayer, as a function of the relative stretch. The drawn line stands for stable states (with or without a pore), the dashed line for a metastable bilayer with a pore, the dash-dotted line for a metastable intact bilayer, and the dotted line for the activation barrier.

coefficient k_C to be equal to $3.5\,\varepsilon\sigma^{-1}$ or 3.5×10^{-11} J/m. Additional simulations on a smaller system of 288 amphiphiles and 2700 solvent particles are also well described by the same K_A, a_0 and k_C. The line tension coefficient compares favourably with the above cited range of experimental values, $(0.5 - 5) \times 10^{-11}$ J/m.

In Fig. 6.4 are shown the free energies of the minima and maxima, together with those of the intact bilayers, as a function of their relative stretchings. The drawn line represents the stable states of the membrane. For relative stretchings larger than 0.186, punctured membranes with pore radii equal to $R_{\min}$ have the lowest free energies and therefore represent the stable states. For smaller relative stretchings the intact membrane has the lowest free energy. When the relative stretching is exactly 0.186, the punctured and intact membranes have equal free energies and the system can choose freely between them. We call this the equilibrium relative stretching.

For relative stretchings between 0.148 and 0.186 the punctured membrane is metastable. Both in Fig. 6.3 and in Fig. 6.4 these states are represented by a dashed line. Below the critical relative stretch of 0.148 no stable or metastable punctured membrane exists. Figure 6.5 shows

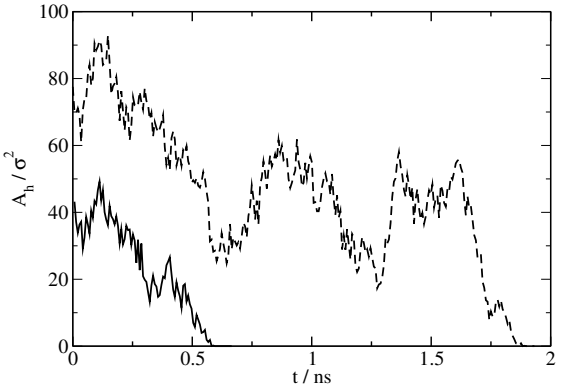

Figure 6.5: Area of a pore as a function of time for a run well below the critical point (solid line, relative stretch of 12%) and a run just below the critical point (dashed line, relative stretch of 14%).

the areas of pores in two artificially punctured membranes with relative stretchings smaller than 0.148. For a stretching value of 12% the pore closed immediately, while for a stretching value of 14%, *i. e.* just below the critical relative stretch, it took about 1.8 nanoseconds. The large fluctuations in the latter case are due to the flatness of the free energy surface in the neighbourhood of the critical point, with a critical pore area of about $50\,\sigma^2$. Here the free energy has an inflection point from which two branches, of local minima and maxima respectively, extend to larger values of the relative stretching. At the critical point $R_{\min}$ and $R_{\max}$ coincide.

With increasing values of the relative stretch above the critical point, the free energy difference between the metastable local minimum and the unstable local maximum quickly grows from zero at the critical point to nearly $20\,k_BT$ at the equilibrium point. As a result, metastable punctured membranes in the neighbourhood of the equilibrium point have to overcome a high activation barrier before they can settle in the stable intact state. For example, the metastable state occurring in Fig. 6.3 at a stretching of 15% *i. e.* just above the critical point, already survived for 12.5 ns before yielding. The next point in the figure was still open when the run was aborted after 20 ns (about one month on a DEC alpha), and is therefore marked

'stable' in the plot. For relative stretchings larger than the equilibrium one, the intact membrane constitutes the metastable state. The barrier between the metastable intact membrane and the stable punctured membrane gradually becomes smaller, starting from nearly $20\,k_BT$ at the equilibrium point to zero for infinite stretchings, with a concomitant decrease in the radius $R_{\max}$ of the transition state. Given that only barriers of a few k_BT can be surmounted on the time scale covered in molecular dynamics simulations, we conclude that by stretching an intact membrane a pore can be created only at stretching values much larger than the equilibrium stretching. In our simulations, rupture was not observed till a relative stretch of 37%, twice the equilibrium stretch. When finally the membrane gives in, the pore that is created is of course much larger than the one that would have been created at the equilibrium point.

6.3.2 Critical and equilibrium points

From our simulations it follows that the critical and equilibrium relative stretchings occur at 14.8% and 18.6% respectively, and these values are even higher for the smaller bilayer. Experimentally, however, it is known that membranes typically rupture (lysis) under a strain of about 2% [50, 86]. In order to understand this seeming discrepancy, we have calculated these values analytically as functions of the system parameters K_A, k_C and A_0.

The equilibrium relative stretch occurs when the free energy of the intact layer equals the free energy of the punctured layer, *i. e.* when

$$\frac{K_A}{2A_0}\left(L_{Eq}^2 - A_0\right)^2 = \frac{K_A}{2A_0}\left(L_{Eq}^2 - \pi R_{Eq}^2 - A_0\right)^2 + 2\pi k_C R_{Eq}. \tag{6.7}$$

This equation must be solved simultaneously with

$$\frac{L_{Eq}^2 - A_0}{A_0} = \pi\frac{R_{Eq}^2}{A_0} + \frac{k_C}{K_A}\frac{1}{R_{Eq}}, \tag{6.8}$$

which guarantees that the free energy of the punctured state is at a minimum. A little bit of algebra yields

$$\frac{L_{Eq}^2 - A_0}{A_0} = 3\left(\frac{k_C}{2K_A}\right)^{2/3}\left(\frac{A_0}{2\pi}\right)^{-1/3}, \tag{6.9}$$

$$R_{Eq} = \left(\frac{k_C}{K_A}\frac{2A_0}{\pi}\right)^{1/3}. \tag{6.10}$$

The area of this pore is related to the excess area by $\pi R_{Eq}^2 = \frac{2}{3}\left(L_{Eq}^2 - A_0\right)$. The critical point occurs when the two extrema of the free energy coincide, *i. e.* when $\alpha = \pi$ in Eqs. (6.4) and (6.5), from which

$$\frac{L_c^2 - A_0}{A_0} = 3\left(\frac{k_C}{2K_A}\right)^{2/3}\left(\frac{A_0}{\pi}\right)^{-1/3}, \tag{6.11}$$

$$R_c = \left(\frac{k_C}{K_A}\frac{A_0}{2\pi}\right)^{1/3}, \tag{6.12}$$

and the area of the pore equals one third of the excess area.

The important point now is that both the critical and the equilibrium relative stretchings are proportional to $A_0^{-1/3}$, and hence to $N^{-1/3}$, *i. e.* the larger the membrane, the smaller the strain it can support. Of course, the critical and equilibrium radii must also grow with system size, which they indeed do proportional to $A_0^{1/3}$ or $N^{1/3}$. These scaling laws are clearly confirmed by the simulation results presented in Fig. 6.3. It is interesting to notice that actually it is not A_0, but the combination of A_0 and k_C/K_A, which governs the scaling of the critical and equilibrium relative stretchings and radii. Finally, we notice that both the ratio of the critical radius to the equilibrium radius and of the critical relative stretch to the equilibrium relative stretch are independent of the system size.

Experiments [50, 86] have shown that amphiphilic bilayers can not support the amount of stretch that we attribute to the equilibrium point of our simulation model. In their study of red blood cells, Evans *et al.* [50] note that 'the maximum area change where immediate lysis occurred was about 4%. Lysis occurred within about 20-30 s for area changes of about 2%.' Using the above scaling argument, we find that for a typical area of $100\,\mu\mathrm{m}^2$ the equilibrium point of our model lies at a relative stretch of about 0.2%. Although this value lies below the onset of rupture in experiments, we think it is satisfying. On the one hand, the simple theory used here leaves room for improvement, which we are currently investigating [140]. On the other hand, as pointed out above, the point of rupture is determined by the stretch as well as the exposure time. It is likely, therefore, that rupture experiments overestimate the equilibrium point.

The equation for the critical radius can also be compared with experimental results. In the experiments by Zhelev and Needham [159] on SOPC/CHOL, a pore was created by electroporation and stabilised by keeping the bilayer under tension through gradual aspiration of the bilayer into a micropipet. Pore radii were obtained from measurements of the volu-

metric flow through the pore. The final pore radius just before collapse must be comparable with our critical pore radius. For comparison we take their liposome radius of $16.0\,\mu\mathrm{m}^2$, *i. e.* an equilibrium surface area $A_0 = 3200\,\mu\mathrm{m}^2$. From their Table I we obtain $R_c = 0.51\,\mu\mathrm{m}$, whereas Eq. (6.12), together with our values of K_A and k_C, yields $R_c = 0.42\,\mu\mathrm{m}$. Since our line tension coefficient k_C is in good agreement with the experimental one for SOPC/CHOL, the good agreement of the two critical radii implies that the elastic coefficient K_A must also agree with the experimental one. The theory thus provides an explanation, alternative to the dynamical stabilisation put forward by Moroz and Nelson [105], for these giant quasi-stable pores, and for their rapid closure. The vesicles studied by Zhelev and Needham were all of roughly the same size, with one exception. This deviant vesicle contained nearly three times as many amphiphiles, and had the largest pore radius. On the basis of this single point, and considering the broad distribution of radii measured for the smaller vesicles, one can at most conclude that the experimental date are commensurate with the power law derived here.

6.3.3 Tension

The change of the free energy of a simulation box upon a change of the parallel box length, at constant total volume, reads as

$$\left(\frac{dF_{\mathrm{box}}}{dL_\parallel}\right)_{N,V,T} = L_\perp L_\parallel \left(2p_{zz} - p_{xx} - p_{yy}\right) = 2L_\parallel \Sigma. \tag{6.13}$$

Here, by definition the left-hand side is equal to

$$\frac{\partial F}{\partial L_\parallel} + \frac{\partial F}{\partial R}\frac{\partial R}{\partial L_\parallel}, \tag{6.14}$$

the first step on the right-hand side is based on the thermodynamic expression for the pressure tensor, and the second step defines the tension Σ. For F_{box} we may read the free energy of the bilayer, Eq. (6.2), because the free energy of the solvent does not change under a volume conserving box deformation. Since $\partial F/\partial R = 0$, we then easily arrive at:

$$\Sigma = \frac{k_C}{R}. \tag{6.15}$$

The above result offers the opportunity to measure the line tension coefficient directly from the simulations, without necessarily knowing the elastic coefficient nor the equilibrium area. In Fig. 6.6 we have plotted the tensions of the punctured membranes, calculated from

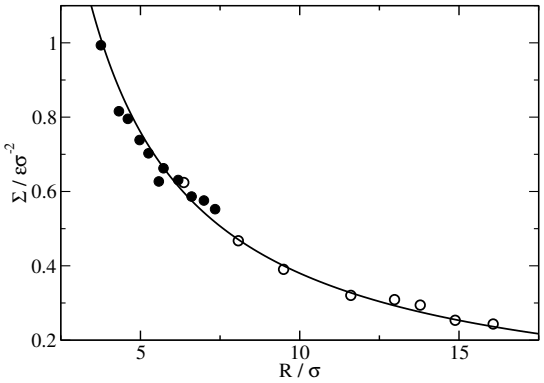

Figure 6.6: The tension on the bilayer plotted against the average radius of the pore. Circles mark the simulation results for a large system (open symbols) and a small system (solid symbols), the line is a fit according to Eq. (6.15).

the pressure difference in Eq. (6.13), against their pore radii. A fit of the large bilayer to the above equation yields k_C equal to $3.9\,\varepsilon\sigma^{-1}$ or 3.9×10^{-11} J/m, in good agreement with our previous result in Section 6.3.1, and consequently with experiments.

Since the equilibrium pore radius increases with increasing membrane size, Eq. (6.15) says that large membranes will rupture under small tensions, and hence under small relative stretches. This is illustrated in Fig. 6.7, where the tension on the ruptured bilayer is plotted as a function of the relative stretch. With increasing system size, the curve moves into the wedge formed by the tension-less state, $\Sigma = 0$, and the linear tension profile of the intact elastic bilayer, $\Sigma = K_A \left(L_{||}^2 - A_0 \right) / A_0$. The theoretical curves, based on the fit to the large bilayer in Fig. 6.3, are seen to match the simulation results for both bilayers. We attribute the small deviations of the small bilayer to the neglect of thermal fluctuations in Eq. (6.2). Elsewhere we describe how the thermal undulations of an intact membrane result in a weak system size dependency of the effective elastic modulus and equilibrium area entering this expression [35].

It is instructive to compare the tensions of the punctured and intact membranes at the equilibrium point. To this end, we write the equilibrium tension of the punctured membrane

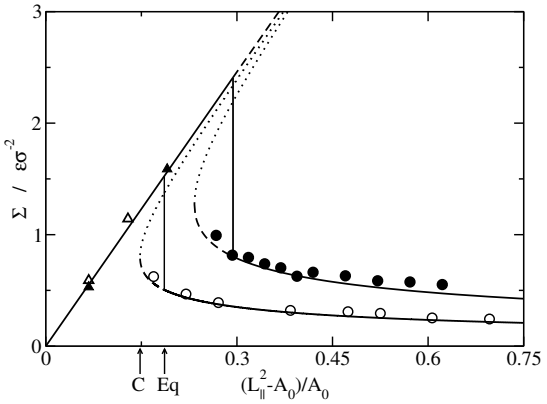

Figure 6.7: The tension on the bilayer plotted against the relative stretch. See Fig. 6.3 for the interpretation of the lines and markers. The straight diagonal lines describe the stable and metastable states of an intact bilayer.

as

$$\Sigma_{Eq}^{\text{pore}} = \frac{k_C}{R_{Eq}} = \frac{1}{3} K_A \frac{L_{Eq}^2 - A_0}{A_0}. \tag{6.16}$$

The tension of the intact membrane at the same relative stretching is

$$\Sigma_{Eq}^{\text{intact}} = K_A \frac{L_{Eq}^2 - A_0}{A_0}. \tag{6.17}$$

Assuming that an intact membrane ruptures near its equilibrium point, we conclude that the tension will drop by a factor of 2/3 as rupture takes place. Conversely, the tension will rise by 50% when a pore closes at the critical point.

Finally, we have performed one more simulation to provide an alternative calculation of the line tension coefficient. In this case the simulation box contained a bilayer strip consisting of 1152 amphiphiles, surrounded by 10 800 solvent particles. All simulation details were identical to those described in Section 6.2. The free energy of such a bilayer reads

$$F = \frac{K_A}{2A_0} \left(L_\parallel w - A_0 \right)^2 + 2k_C L_\parallel, \tag{6.18}$$

where w is the width of the strip. At a given value of $L_\parallel$, the width will adjust itself such that the free energy is minimal, eliminating the surface term from the above expression. The

tension is then found to be given by

$$\Sigma = \frac{k_C}{L_{\|}}, \tag{6.19}$$

The line tension coefficient received from Eq. (6.19) was $4.0\,\varepsilon\sigma^{-1}$ or 4.0×10^{-11} J/m. All calculated line tension coefficients are in good agreement with one another, and lie in the experimental range [23, 49, 91, 105, 159].

6.4 Summary and discussion

Using a coarse grained amphiphilic model, we have simulated a punctured amphiphilic bilayer under various stretching conditions. The phase diagram, showing the dependence of the pore radius on the relative amount of stretching, could well be described on the basis of a simple free energy containing elastic and edge free energies only. The line tension coefficient k_C obtained from our simulations equals $(3.5-4.0) \times 10^{-11}$ J/m, which is in good agreement with available experimental values for such systems: $(0.5-5) \times 10^{-11}$ J/m.

The phase diagram for a membrane of 1152 amphiphiles shows that between 0 and 18.6% of relative stretch the intact membrane is stable, while at the latter point, like at a first order thermodynamic phase transition, the membrane suddenly opens up to accommodate a stable pore. Between 14.8 and 18.6% of relative stretching, the possibility of accommodating a metastable pore exists. The first of these values is called the critical relative stretching and the latter the equilibrium relative stretching. Although obviously no free energy barrier exists between the stable intact membrane and the metastable punctured membrane at the critical point, such a barrier quickly develops on going to larger amounts of relative stretching. At the equilibrium point this barrier amounts to $20\,k_BT$. The existence of such a barrier has often been invoked to explain why during molecular dynamics simulations of stretched intact membranes hardly ever rupturing occurs. This can not be the only reason however, since already our equilibrium relative stretching is much larger than the one usually found experimentally.

In order to explain the above discrepancy, we have undertaken a finite size scaling analysis by calculating analytically the dependence of the phase diagram on the equilibrium size of the system. It turns out that, basically because the elastic surface free energy and the edge free energy scale differently with system size, that the phase diagram moves towards lower

values of relative stretching with increasing system size. Taking these effects into account, we find a satisfying agreement between calculated and experimental critical relative stretchings. A similar analysis has been given by Binder [20] in the case of nucleation free energies in supersaturated gases.

For the simulations presented here we used the $NA_{\parallel}L_{\perp}T$ ensemble, with the projected bilayer area and the perpendicular box height related by the condition of a fixed total volume, $V = A_{\parallel}L_{\perp}$. This particular choice is suggested by Eqs. (6.2) and (6.13). Since experiments are commonly carried out under constant perpendicular pressure, rather than under constant volume, the $NA_{\parallel}p_{\perp}T$ ensemble offers an attractive alternative. A closer inspection of our simulations reveals that the variation of $p_{\perp}$ with $A_{\parallel}$ amounts to just 1%, so we do not expect significant differences between the two ensembles. In this context we want to point out an interesting consequence of Fig. 6.7 for simulations in the constant surface tension, $N\Sigma p_{\perp}T$, ensemble. The intact bilayer requires the common negative feedback algorithm, as present in all barostats: if the tension is too high, the area is reduced to drive the system back to the desired tension. But because the slope of Σ versus $A_{\parallel}$ changes sign after the formation of a pore, the punctured bilayer needs a positive feedback algorithm instead: if the tension is too high, the area should be increased in order to reduce the tension. A negative feedback will tear a punctured bilayer apart, as has been observed in numerous simulations.

Since our theoretical description is macroscopic, it can not be applied at very small values of the pore radius. In particular, our description does not include possible pore nucleation free energies. For a pore to appear, the amphiphiles which are going to constitute the edge of the pore must change orientation from perpendicular to the membrane to parallel to the membrane. The free energy per amphiphile needed for this process will be different from the free energy per amphiphile for a similar process to take place when a pore already exists. The nucleation free energies is described in the previous chapter.

Summary

In this thesis we report on free energy calculations for calix[4]arenes and amphiphilic bilayers by using molecular dynamics simulations. The calix[4]arene is a bowl-shaped molecule consisting of four phenol rings, which can rotate around the connecting methylene bridges. The isomerization of calix[4]arene studied in the first part of this thesis concerns the rotation of one of the phenol rings, while the orientation of the three other phenol rings remains unchanged. An amphiphilic bilayer is a membrane resulting from the self-assembly of amphiphilic molecules dissolved in water. This property reflects the chemical nature of amphiphilic molecules, consisting of a hydrophilic head and a hydrophobic tail. In experiments, bilayers can not support a large mechanical stress. As a result, bilayers rupture or pores are opened. The second part of the thesis is devoted to pore formation in an amphiphilic bilayer under different stretching conditions.

In *Chapter 3* the influence of solvation on the conformational isomerism of calix[4]arene and *p-tert*-butyl-calix[4]arene is studied by using the quantum mechanical (QM) and semi-classical (SC) formalisms of the Miertus, Scrocco, Tomasi (MST) continuum model. The results of both QM-MST and SC-MST are in good agreement with the experimental results and with molecular dynamics simulations performed with explicit treatment of the solvent molecules, as described in *Chapter 4*. As evidenced by the results, the accuracy of SC-MST dependes on the atomic charges used. It is shown that the MST continuum method is inexpensive method, giving an adequate description of solvation effects for calix[4]arene and *p-tert*-butyl-calix[4]arene in water and chloroform.

In *Chapter 4* we studied the isomerization reaction of calix[4]arene and *p-tert*-butyl-calix[4]arene in vacuum and in chloroform by using molecular dynamics simulations. As a first step we calculated the free energies of calix[4]arene and *p-tert*-butyl-calix[4]arene in a vacuum as a function of the reaction coordinate by using the umbrella sampling method. The reaction coordinate chosen was the angle of the rotating phenol ring. The resulting free energies in a vacuum were used as a first trial of the free energy calculations in chloroform. The free energy of calix[4]arene in chloroform is then readily obtained by the umbrella sampling method. The calculation of the free energy of *p-tert*-butyl-calix[4]arene in chloroform, how-

ever, was complicated by the confinement of one of the chloroform molecules inside the cavity present in the cone conformation. We proposed two methods to calculate the free energy in this case: windows umbrella sampling and a new combined coupling parameter−umbrella sampling approach. The rate constants obtained by the reactive flux method were in good agreement with experimental data.

In *Chapter 5* the formation of a pore in an amphiphilic bilayer was studied. The amphiphilic bilayer and solvent were represented by a coarse-grained model. We performed the calculation of the free energy profile by the potential of mean constrained force method with a new type of constrained reaction coordinate. This reaction coordinate was a function of the coordinates of all tail particles, whereas a reaction coordinate usually is a function of the coordinates of only one molecule. With this choice, we could smoothly control the opening of the pore, including the preceding rearrangement of the amphiphilic molecules about to constitute the edge of the bilayer. The obtained free energy as a function of the reaction coordinate was transformed into a function of the pore radius, coinciding perfectly with the macroscopic free energy expression proposed in *Chapter 6*. The line tension coefficient thus obtained agreed well both with the values obtained in *Chapter 6* and with experimental data.

In *Chapter 5* we reported on molecular dynamics simulations of an amphiphilic bilayer with a pore under various elongations. As in *Chapter 6*, we used a coarse-grained amphiphilic model. We proposed that the free energy of a bilayer with a pore is just the sum of elastic and edge free energies. The dependence of the pore radius on the relative stretch of the bilayer was well described by this model. The remarkable result of our model was a system size dependence, which shifted the phase diagram towards lower relative stretching values for increasing system size, resulting in a good agreement of the equilibrium relative stretch and the pore radius with experimental data on much larger systems. The line tension coefficients obtained from our simulations were also in a good agreement with experimental values and with those deduced from the free energy function in *Chapter 5*.

Samenvatting

In dit proefschrift beschrijven we vrije energie berekeningen aan calix[4]arenen en amfifiele bilagen met behulp van moleculaire dynamica simulaties. Een calix[4]areen is een kom-vormig molecuul bestaande uit vier fenolringen, die kunnen draaien om de verbindende methyleenbruggen. De isomerisatie van calix[4]arenen bestudeerd in het eerste deel van dit proefschrift betreft de rotatie van één van de fenolringen, terwijl de oriëntatie van de drie overige fenolringen onveranderd blijft. Een amfifiele bilaag is een membraan dat ontstaat door de zelf-assemblage van amfifiele moleculen opgelost in water. Deze eigenschap weerspiegelt de chemische opbouw van amfifiele moleculen, een hydrofiele kop verbonden met een hydrofobe staart. Experimenteel blijkt dat bilagen geen grote mechanische spanningen kunnen weerstaan; ze scheuren kapot of er ontstaan poriën. Het tweede deel van dit proefschrift is gewijd aan porievorming in amfifiele bilagen onder verschillende spanningen.

In *Hoofdstuk* 3 wordt de invloed van het oplosmiddel op de conformaties van calix[4]-arene and *p-tert*-butyl-calix[4]areen bestudeerd, gebruik makend van een quantum mechanische (QM) en een semi-klassieke (SC) formulering van het Miertus, Scrocco & Tomasi (MST) continuüm model. De resultaten van zowel QM-MST als SC-MST zijn in goede overeenstemming met de experimentele resultaten en met moleculaire dynamica simulaties uitgevoerd met expliciete oplosmiddel moleculen, zoals beschreven in *Hoofdstuk* 4. De bevindingen wijzen erop dat de nauwkeurigheid van SC-MST afhangt van de gebruikte atomaire ladingen. De MST continuüm methode blijkt een goedkope methode, met een adequate beschrijving van oplosmiddel effecten voor calix[4]areen en *p-tert*-butyl-calix[4]areen in water en chloroform.

In *Hoofdstuk* 4 bestuderen we de isomerisatie reactie van calix[4]areen en *p-tert*-butyl-calix[4]areen in vacuüm en chloroform, gebruik makend van moleculaire dynamica simulaties. In de eerste stap worden de vrije energiën van calix[4]areen en *p-tert*-butyl-calix[4]-areen in vacuüm als een functie van de reactiecoördinaat berekend met de umbrella sampling methode. De gekozen reactiecoördinaat is de hoek van de roterende fenolring. De aldus verkregen vrije energiën in vacuüm dienen als een eerste benadering voor de vrije energie berekeningen in chloroform. De vrije energie van calix[4]areen in chloroform wordt dan

eenvoudig verkregen met de umbrella sampling methode. De berekening van de vrije energie van *p-tert*-butyl-calix[4]areen in chloroform, daarentegen, wordt gecompliceerd door de inclusie van één van de chloroform moleculen in de holte van de cone conformatie. We dragen twee methodes aan om de vrije energie in deze situatie uit te rekenen: windows umbrella sampling en een nieuwe gecombineerde coupling parameter - umbrella sampling aanpak. De reactiesnelheden verkregen met de reactieve flux methode zijn in goede overeenstemming met de experimentele data.

In *Hoofdstuk* 5 wordt de vorming van een porie in een amfifiele bilaag bestudeerd. De amfifiele bilaag en het oplosmiddel worden gerepresenteerd met een coarse grained model. Voor de berekening van het vrije energie profiel gebruiken we de potentiaal van de gemiddelde constraint kracht, met een nieuw type geconstrainde reactiecoördinaat. Deze reactiecoördinaat is een functie van de coördinaten van alle staartdeeltjes, terwijl de gebuikelijke reactie coördinaten functies zijn van de coördinaten van slechts één molecuul. Met deze keuze kunnen we het openen van een porie vloeiend controleren, inclusief de daaraan voorafgaande re-orientatie van de amfifiele moleculen die de rand van de bilaag zullen gaan vormen. De verkregen vrije energie als een functie van de reactiecoördinaat wordt getransformeerd naar een functie van de poriestraal, en blijkt goed overeen te stemmen met de macroscopische expressie geïntroduceerd in *Hoofdstuk* 6. De aldus gevonden lijnspannings coëfficiënt komt goed overeen met zowel de waarde gevonden in *Hoofdstuk* 6 als met experimentele waardes.

In *Hoofdstuk* 5 brengen we verslag uit van moleculaire dynamica simulaties van een amfifiele bilaag met een porie onder verschillende uitrekkingen. Net als in *Hoofdstuk* 5 wordt er een coarse grained model gebruikt. We nemen aan dat de vrije energie van een bilaag met een porie simpelweg de som van elastische en rand vrije energiën is. De afhankelijkheid van de poriestraal van de relatieve uitrekking wordt goed beschreven door deze theorie. Een opmerkelijk resultaat van onze theorie is een systeemgrootte afhankelijkheid. Hierdoor verschuift het fasediagram naar lagere relatieve uitrekking met toenemende systeemgrootte, resulterend in een goede overeenstemming van de evenwichts relatieve uitrekking en poriestraal met de experimentele data van veel grotere systemen. De lijnspanningscoëfficiënt verkregen uit onze simulaties is in goede overeenstemming met de experimentele waardes en met de waarde verkregen uit de vrije energie functie in *Hoofdstuk* 5.

Acknowledgements

Dear reader, here I would like to acknowledge the people, who surround me during these almost 5 years.

First of all, I am grateful to my promotor Wim Briels for giving me a possibility to do this PhD research and for stimulating me to be independent in research. I thank a lot my assistant-promotor Wouter den Otter, who taught me to pay attention to details. Owing to him my skills in English improved a lot. Special thanks to Carlos Alemán for extending the field of my PhD research to Quantum Chemistry and without whom Chapter 4 would never appear.

I thank my colleagues PhD students, Johan Padding, Harald Tepper and Reiner Akkermans, for being available for help in the period of adaptation to the research environment of the group. I am grateful to Dick Feil, who was the first person encouraging me to speak Dutch.

I thank Marieke Janssen, Peter Kindt, Albert van der Noort, Sergey Shkulipa, Wladimir Shchettinin, Yuguo Tao and Amol Thakre for making this time interesting and pleasant.

I would like thank my parents for giving me a possibility to study. I thank my mother and my parents in law for frequent family visits, it was very important for us and especially for our kids.

Finally, I thank my husband and my children for their love, friendship and understanding.

Tanya Tolpekina Enschede, September 2004.

About the author

The writer of this thesis was born on February 3, 1975 in Odessa, Soviet Union. In June 1992 she has completed her secondary school education at school № 16 in Odessa, with specialization in physics and mathematics. In the same year she started to study Physics at the Physical faculty of the Odessa State University. Her graduation work, carried at Theoretical Physics Group, was devoted to quantum mechanical description of electron motion along two periodical chains of two different types of atoms. After graduating from Odessa State University in 1997 she followed the Functional Analysis course at Mathematical faculty of the Odessa Pedagogical University. On 15 November 1999 she started PhD research, which has resulted in this Thesis, at the Computational Dispersion Rheology Group at University of Twente in the Netherlands.

Bibliography

[1] R. Abidi, M. V. Baker, J. M. Harrowfield, D. S.-C. Ho, W. R. Richmond, B. W. Skelton, A. H. White, A. Varnek, and G. Wipff. *Inorg. Chim. Acta*, 246:275, 1996.

[2] C. Alemán. *Chem. Phys.*, 244:151, 1999.

[3] C. Alemán. *Chem. Phys. Lett.*, 302:461, 1999.

[4] C. Alemán, W. K. den Otter, T. V. Tolpekina, and W. J. Briels. *J. Org. Chem.*, 69:951, 2004.

[5] C. Alemán and S. E. Galembeck. *Chem. Phys.*, 232:151, 1998.

[6] C. Alemán, M. Orozco, and F. J. Luque. *J. Chem. Phys.*, 189:573, 1994.

[7] C. Alemán and J. Puiggali. *J. Org. Chem.*, 60:910, 1995.

[8] M. P. Allen and D. J. Tildesley. *Computer simulation of liquids*. Oxford University Press, Oxford, 1987.

[9] G. D. Andreetti, Pochini A., and Ungaro R. *J. Chem. Soc. Perkin. Trans. 2*, page 1773, 1983.

[10] K. Araki, S. Shinkai, and T. Matsuda. *Chem. Lett.*, 1989:581, 1989.

[11] P. W. Atkins. *Physical Chemistry*. Oxford University Press, Oxford, U. K., 1990.

[12] M. Bachs, F. J. Luque, and M. Orozco. *J. Comput. Chem.*, 15:446, 1994.

[13] A. C. Backes, J. Schatz, and H.-U. Siehl. *J. Chem. Soc., Perkin. Trans. 2*, page 484, 2002.

[14] R. Bar-Ziv, T. Frisch, and E. Moses. *Phys. Rev. Lett.*, 75:3481, 1995.

[15] F. Benevelli, A. Bond, M. Duer, and J. Klinowski. *Phys. Chem. Chem. Phys.*, 2:3977, 2000.

[16] W. F. Berendsen, H. J. C.; van Gunsteren. *GROMOS Reference Manual*. University of Groningen, Groningen, The Netherlands, 1987.

[17] S. E. Biali, V. Böhmer, J. Brenn, M. Frings, I. Thondorf, W. Vogt, and J. Wöhnert. *J. Org. Chem.*, 62:8350, 1997.

[18] S. E. Biali, V. Böhmer, S. Cohen, G. Ferguson, C. Grüttner, F. Grynszpan, E. F. Paulus, I. Thondorf, and W. Vogt. *J. Am. Chem. Soc.*, 118:12938, 1996.

[19] M. Bier, W. Chen, T. R. Gowrishankar, R. D. Astumian, and R. C. Lee. *Phys. Rev. E*, 66:062905, 2002.

[20] K. Binder. *Physica A*, 319:99, 2003.

[21] J. R. Blas, M. Marquez, J. Sessler, F.J. Luque, and M. Orozco. *J. Am. Chem. Soc*, 124:12796, 2002.

[22] P. G. Bolhuis, D. Chandler, C. Dellago, and P. L. Geissler. *Annual Rev. Phys. Chem.*, 53:291, 2000.

[23] F. Brochard-Wyart, P. G. de Gennes, and O. Sandre. *Physica A*, 278:32, 2000.

[24] E. B. Brouwer, G. D. Enright, and J. A. Ripmeester. *Supramol. Chem.*, 7:7, 1996.

[25] E. Brouyëre, A. Persoons, and J. Bredas. *J. Phys. Chem. A*, 101:4142, 1997.

[26] M. Cajan, P. Lhotak, J. Lang, H. Dvorakova, I. Stibor, and J. Koca. *J. Chem. Soc. Perkin Trans. 2*, 11:1922, 2002.

[27] R. Carr and M. Parrinello. *Phys. Rev. Lett.*, 55:2471, 1985.

[28] J. Casanovas, A. M. Namba, S. Leon, G. L. B. Aquino, G. V. J. da Silva, and C. Alemán. *J. Org. Chem.*, 66:3775, 2001.

[29] D. J. Chandler. *J. Chem. Phys.*, 68:2959, 1978.

[30] P. Claverie, J. P. Daudey, J. Langlet, B. Pullman, and D. Piazzola. *J. Phys. Chem.*, 82:405, 1978.

[31] C. J. Cramer and D Truhlar. *Chem. Rev.*, 99:2161, 1999.

[32] C. Curutchet, C. J. Cramer, D. G. Truhlar, M. F. Ruiz-López, D. Rinaldi, M. Orozco, and F. J. Luque. *J. Comput. Chem.*, 24:284, 2003.

[33] C. Curutchet, M. Orozco, and F. J. Luque. *J. Comput. Chem.*, 22:1180, 2001.

[34] E. Darve and A. Pohorille. *J. Chem. Phys.*, 115:9169, 2001.

[35] W. K. den Otter and W. J. Briels. in preparation.

[36] W. K. den Otter and W. J. Briels. *J. Chem. Phys.*, 107:4968, 1997.

[37] W. K. den Otter and W. J. Briels. *J. Chem. Phys.*, 106:5494, 1997.

[38] W. K. den Otter and W. J. Briels. *J. Chem. Phys.*, 109:4139, 1998.

[39] W. K. den Otter and W. J. Briels. *J. Am. Chem. Soc.*, 120:13167, 1998.

[40] W. K. den Otter and W. J. Briels. *Mol. Phys.*, 98:773, 2000.

[41] W. K. den Otter and W. J. Briels. *J. Chem. Phys.*, 112:7283, 2000.

[42] W. K. den Otter and W. J. Briels. *J. Chem. Phys.*, 118:4712, 2003.

[43] W. K. den Otter, S. A. Shkulipa, and W. J. Briels. *J. Chem. Phys.*, 119:2363, 2003.

[44] M. J. S. Dewar, E. G. Zoebisch, E. F. Healy, and J. J. P. Stewart. *J. Am. Chem. Soc.*, 107:3902, 1985.

[45] W. Dietz and K. Heizinger. *Ber. Bunsenges. Phys. Chem.*, 88:543, 1984.

[46] E. Evans and V. Heinrich. *C. R. Physique*, 4:265, 2003.

[47] E. Evans, V. Heinrich, F. Ludwig, and W. Rawicz. *Biophys. J.*, 85, 2003.

[48] E. Evans, V. Heinrich, F. Ludwig, and W. Rawicz. *BioPhys. J.*, 85:2342, 2003.

[49] E. A. Evans and F. Ludwig. *J. Phys.: Cond. Matter*, 12:A315, 2000.

[50] E. A. Evans, R. Waugh, and L. Melnick. *BioPhys. J.*, 16:585, 1976.

[51] H. J. Eyring. *J. Chem. Phys.*, 3:107, 1935.

[52] O. Farago. *J. Chem. Phys.*, 119:596, 2003.

[53] S. Fischer, P. D. J. Grootenhuis, L. C. Groenen, W. P. van Hoorn, F. C. J. M. van Veggel, D. N. Reinhoudt, and M. Karplus. *J. Am. Chem. Soc.*, 117:1611, 1995.

[54] X. Fradera, M. Marquez, B. D. Smith, M. Orozco, and F. J. Luque. *J. Org. Chem.*, 68:4663, 2003.

[55] S. A. Freeman, M. A. Wang, and J. C. Weaver. *BioPhys. J.*, 67:42, 1994.

[56] D. Frenkel and B. Smit. *Understanding Molecular Simulation*. Academic Press, San Diego, CA, 1996.

[57] M. J. Frisch, G. W. Trucks, H. B. Schlegel, G. E. Scuseria, M. A. Robb, J. R. Cheeseman, V. G. Zakrzewski, J. A. Montgomery, R. E. Stratmann, J. C. Burant, S. Dapprich, J. M. Millam, A. D. Daniels, K. N. Kudin, M. C. Strain, O. Farkas, J. Tomasi, V. Barone, M. Cossi, R. Cammi, B. Mennucci, C. Pomelli, C. Adamo, S. Clifford, J. Ochterski, G. A. Petersson, P. Y. Ayala, Q. Cui, K. Morokuma, D. K. Malick, A. D. Rabuck, K. Raghavachari, J. B. Foresman, J. Cioslowski, J. V. Ortiz, A. G. Baboul, B. B. Stefanov, G. Liu, A. Liashenko, P. Piskorz, I. Komaromi, R. Gomperts, R. L. Martin, D. J. Fox, T. Keith, M.A. Al-Laham, C. Y. Peng, A. Nanayakkara, C. Gonzalez, M. Challacombe, P. M. W. Gill, B. Johnson, W. Chen, M. W. Wong, J. L. Andres, C Gonzalez, M. Head-Gordon, E. S. Replogle, and J. A. Pople. *Gaussian 98, Revision A.7*. Gaussian, Inc., Pittsburgh PA, 1998.

[58] J. Gao. *Biophys. Chem.*, 51:253, 1994.

[59] J. Gao. *Acc. Chem. Res.*, 29:298, 1996.

[60] R. W. Glaser, S. L. Leikin, L. V. Chernomordik, V. F. Pastushenko, and A. I. Sokirko. *bba*, 940:275, 1988.

[61] R. Goetz, G. Gompper, and R. Lipowsky. *Phys. Rev. Lett.*, 82:221, 1999.

[62] R. Goetz and R. Lipowsky. *J. Chem. Phys.*, 108:7397, 1998.

[63] V. Gogonea and K. M. Merz. *J. Phys. Chem. A*, 103:5171, 1999.

[64] R. D. Groot and K. L. Rabone. *BioPhys. J.*, 81:725, 2001.

[65] P. D. J. Grootenhuis, P. A. Kollman, L. C. Groenen, D. N. Reinhoudt, G. J. van Hummel, F. Ugozzole, and G. D. Andreeti. *J. Am. Chem. Soc.*, 112:4165, 1990.

[66] P. Guilbaud, A. Varnek, and G. Wipff. *J. Am. Chem. Soc*, 115:8298, 1993.

[67] C. D. Gutsche. *Acc. Chem. Res.*, 16:161, 1982.

[68] C. D. Gutsche. *Acc. Chem. Res.*, 16:161, 1983.

[69] C. D. Gutsche. *Calixarenes, Monographs in Supramolecular Chemistry*. The Royal Society of Chemistry, Cambridge, 1989.

[70] C. D. Gutsche and L. J. Bauer. *J. Am. Chem. Soc.*, 107:6052, 1985.

[71] C. D. Gutsche, T. C. Kung, and M.-L. Hsu. *Abstracts of the 11th Midwest Regional Meeting of the American Chemical Society, Carbondale, IL*, 517, 1975.

[72] C. D. Gutsche and R. Muthukrishan. *J. Org. Chem.*, 43:4905, 1978.

[73] C. D. Gutsche, J. S. Rogers, D. Stewart, and K.-A. See. *Pure. Appl. Chem.*, 62:485, 1990.

[74] P. Hänggi, P. Talkner, and M. Borkovec. *Rev. Mod. Phys.*, 62:251, 1990.

[75] T. Harada, F. Ohseto, and S. Shinkai. *Tetrahedron*, 50:13377, 1994.

[76] T. Harada, J. M. Rudzinski, E. Osawa, and S. Shinkai. *Tetrahedron*, 49:5941, 1993.

[77] P.C. Hariharan and J. A. Pople. *Theor. Chim. Acta*, 28:213, 1973.

[78] W. Helfrich. *Z. Naturforsch.*, 28:693, 1973.

[79] V. Helms and R. C. Wade. *J. Comput. Chem.*, 18:449, 1997.

[80] H. W. Huang, Chen F. Y., and M. T. Lee. *Phys. Rev. Lett.*, 92:198304, 2004.

[81] A. Ikeda and S. Shinkai. *Chem. Rev.*, 97:1713, 1997.

[82] K. Iwamoto, A. Ikeda, K. Araki, T. Harada, and S. Shinkai. *Tetrahedron*, 49:9937, 1993.

[83] P. A. Kollman. *Acc. Chem. Res.*, 29:461, 1996.

[84] E. Kreyszig. *Differential Geometry*. Dover, New York, 1991.

[85] S. Kumar, D. Bouzida, R. H. Swedsen, P. A. Kollman, and J. M. Rosenberg. *J. Comput. Chem.*, 13:1011, 1992.

[86] R. Kwok and E. Evans. *BioPhys. J.*, 35:637, 1981.

[87] S. León, D. A. Leigh, and F. Zerbetto. *Chem. Eur. J.*, 8:4854, 2002.

[88] H. Leontiadou, A. E. Mark, and S. J. Marrink. *BioPhys. J.*, 86:2156, 2004.

[89] J. H. Lin and A. Baumgaertner. *BioPhys. J.*, 78:1714, 2000.

[90] J. D. Litster. *Phys. Lett. A*, 53:193, 1975.

[91] S. Loi, G. Sun, W. Franz, and H.-J. Butt. *Phys. Rev. E*, 66:031602, 2002.

[92] C. Loison, M. Mareschal, and F. Schmid. *J. Chem. Phys.*, 121:4, 2004.

[93] F. J. Luque, M. Bachs, C. Alemán, and M. Orozco. *J. Comput. Chem.*, 17:806, 1996.

[94] F. J. Luque, J. M. Bofill, and M. Orozco. *J. Chem. Phys.*, 107:1293, 1997.

[95] F. J. Luque and M. Orozco. *J. Phys. Chem. B*, 101:5573, 1997.

[96] F. J. Luque, C. Zhang, C. Alemán, M. Bachs, and M. Orozco. *J. Phys. Chem.*, 100:4269, 1996.

[97] P. Marmottant and S. Hilgenfeldt. *Nature*, 423:153, 2003.

[98] S.-J. Marrink, E. Lindahl, O. Edholm, and A. E. Mark. *J. Am. Chem. Soc.*, 123:8638, 2001.

[99] M. H. Mazor, J. A. McCammon, and T. P. Lybrand. *J. Am. Chem. Soc.*, 111:55, 1989.

[100] M. H. Mazor, J. A. McCammon, and T. P. Lybrand. *J. Am. Chem. Soc.*, 112:4411, 1990.

[101] D. A. McQuarrie. *Statistical mechnics*. Harper and Row, New York, 1976.

[102] K. C. Melikov, V. A. Frolov, A. Shcherbakov, A. V. Samsonov, Y. A. Chizmadzhev, and L. V. Chernomordik. *BioPhys. J.*, 80:1829, 2001.

[103] S. Miertus, E. Scrocco, and J. Tomasi. *Chem. Phys.*, 55:117, 1981.

[104] S. Miertus and J. Tomasi. *Chem. Phys.*, 65:239, 1982.

[105] J. D. Moroz and P. Nelson. *BioPhys. J.*, 72:2211, 1997.

[106] T. Mülders, P. Krüger, W. Swegat, and J. Schlitter. *J. Chem. Phys.*, 104:4869, 1996.

[107] M. Müller, K. Katsov, and M. Schick. *J. Chem. Phys.*, 116:2342, 2002.

[108] Ronald R. Netz and M. Schick. *Phys. Rev. E*, 53:3875, 1995.

[109] H. Noguchi and M. Takasu. *J. Chem. Phys.*, 115:9547, 2001.

[110] M. I. Ogden, A. L. Rohl, and J. D. Gale. *Chem. Commun.*, page 1626, 2001.

[111] L. Onsager. *Phys. Rev.*, 37:405, 1931.

[112] L. Onsager. *Phys. Rev.*, 38:2265, 1931.

[113] M. Orozco, M. Bachs, and F. J. Luque. *J. Comput. Chem.*, 16:563, 1995.

[114] M. Orozco and F. J. Luque. *Chem. Rev.*, 100:4187, 2000.

[115] M. Orozco, R. Roca, C. Alemán, M. A. Busquets, J. M. López, and F. J. Luque. *J. Mol. Struct.*, 371:269, 1996.

[116] P. Parzuchowski, V. Böhmer, S. E. Biali, and I. Thondorf. *Tetrahedron-Asymmetry*, 11:2393, 2000.

[117] D. A. Pearlman and P. A. Kollman. *J. Chem. Phys.*, 94:4532, 1991.

[118] R. A. Pierotti. *Chem. Rev.*, 76:717, 1976.

[119] C. Reichart. *Solvents and Solvent Effects in Organic Chemistry*. VCH, Weihein, 2 edition, 1990.

[120] C. A. Reynolds, J. W. Essex, and W. G. Richards. *J. Comput. Chem.*, 114:9075, 1992.

[121] J. P. Ryckaert, G. Ciccotti, and H. J. C. Berendsen. *J. Comput. Phys.*, 23:327, 1977.

[122] S. A. Safran. *Statistical Thermodynamics of Surfaces, Interfaces and Membranes*. Addison-Wesley, Reading, MA, 1994.

[123] O. Sandre, L. Moreaux, and F. Brochard-Wyart. *Proc. Nat. Acad. Sci. USA*, 96:10591, 1999.

[124] J. C. Schillock and U. Siefert. *BioPhys. J.*, 74:1754, 1998.

[125] I. Schlachter, U. Höweler, W. Iwanek, M. Urbaniak, and J. Mattay. *Tetrahedron*, 55, 1999.

[126] Jürgen Schlitter and Marco Klähn. *J. Chem. Phys.*, 118:2057, 2002.

[127] P. Sens and S. A. Safran. *Europhys. Lett.*, 43:95, 1998.

[128] J. C. Shillcock and U. Seifert. *BioPhys. J.*, 74:1754, 1998.

[129] B. Smit, P. A. J. Hilbers, K. Esselink, L. A. M. Rupert, N. M. van Os, and A. G. Schlijper. *J. Phys. Chem.*, 95:6361, 1991.

[130] T. R. Smith, W.; Forester. *DLPOLY_2 User Manual,CCLRC*. Daresbury Laboratory, Daresbury, U.K., 2001.

[131] W. Smith and T. R. Forester. *J. Mol. Graphics*, 14:136, 1996.

[132] A. Soi, A. Bauer, H. Mauser, C. Moll, F. Hampel, and A. Hirsch. *J. Chem. Soc. Perkin Trans. 2*, page 1471, 1998.

[133] D. Sornette and N. Ostrowsky. In W. M. Gelbart, A. Ben-Shaul, and D. Roux, editors, *Micelles, Membranes, Micro-Emulsions and Monolayers*, page 251. Springer Verlag, Berlin, Germany, 1994.

[134] M. Sprik and G. Ciccotti. *J. Chem. Phys.*, 109:7737, 1998.

[135] J. J. P. Stewart. *MOPAC 93 Revision 2*. Fujitsu Limited 1993, version modified by F. J. Luque and M. Orozco, 1994.

[136] S. D. Stoddard. *J. Comput. Phys*, 27:291, 1977.

[137] L. Stryer. *Biochemistry*. W. H. Freeman and Comp., New York, N. Y., 4 edition, 1995.

[138] V. Talanquer and D. W. Oxtoby. *J. Chem. Phys.*, 118:872, 2002.

[139] D. P. Tieleman, H. Leontiadou, A. E. Mark, and S.-J. Marrink. *J. Am. Chem. Soc.*, 125:6382, 2003.

[140] T. V. Tolpekina, W. K. den Otter, and W. J. Briels. accepted in J. Chem. Phys.

[141] T. V. Tolpekina, W. K. den Otter, and W. J. Briels. accepted in J. Chem. Phys.

[142] T. V. Tolpekina, W. K. den Otter, and W. J. Briels. *J. Phys. Chem. B*, 107:14476, 2003.

[143] J. Tomasi and M. Persico. *Chem. Rev.*, 94:2027, 1994.

[144] R. Ungaro, A. Pochini, G. D. Andreetti, and V. Sangermano. *J. Chem. Soc. Perkin. Trans. 2*, page 1979, 1984.

[145] J. M. van Gelder, J. Brenn, I. Thondorf, and S. E. Biali. *J. Org. Chem.*, 62:3511, 1997.

[146] W. F. van Gunsteren. In W. F. van Gunsteren and P. K. Weiner, editors, *Computer Simulations of Biomolecular systems: Theoretical and Experimental Applications*, volume 2, page 27. ESCOM, Leiden, The Netherlands, 1989.

[147] W. F. van Gunsteren. In W. F. van Gunsteren and P. K. Weiner, editors, *Computer Simulations of Biomolecular systems: Theoretical and Experimental Applications*, volume 2, page 27. ESCOM, Leiden, The Netherlands, 1989.

[148] W. F. van Gunsteren, F. J. Luque, D. Timms, and A. E. Torda. *Annu. Rev. Biophys. Biomol. Struct.*, 23:847, 1994.

[149] W. F. van Gunsteren, P. K. Weiner, and A.J Wilkinson. *Computer Simulation of Biomolecular Systems: Theoretical and Experimental Applications*, volume 3. Eds.;Kluwer, Dordrecht, 1997.

[150] W. P. van Hoorn, W. J. Briels, J. P. M. van Duynhoven, F. C. J. M. van Veggel, and D. N. Reinhoudt. *J. Org. Chem.*, 63:1299, 1998.

[151] W. P. van Hoorn, G. H. Morshuis, F. C. J. M. van Veggel, and D. N. Reinhoudt. *J. Phys. Chem. A*, 102:1130, 1998.

[152] A. Varnek and G. Wipff. *J. Phys. Chem.*, 97:10840, 1993.

[153] J. Vicens and V. Böhmer. *Calixarenes. A Versatile Class of Macrocyclic Compounds*. Kluwer Academic, Dordrecht, 1991.

[154] D. E. Williams. *J. Comput. Chem.*, 9:745, 1988.

[155] D. E. Williams. *Biopolymers*, 29:1367, 1990.

[156] Y. D. Wu, D-F. Wang, and J. L. Sessler. *J. Org. Chem.*, 66:3739, 2001.

[157] M. Zacharias, T. P. Straatsma, and J. A. McCammon. *J. Chem. Phys.*, 100:9025, 1994.

[158] D. Zahn and J. Brickmann. *Chem. Phys. Lett.*, 352:441, 2002.

[159] D. V. Zhelev and D. Needham. *Biochim. Biophys. Acta*, 1147:89, 1993.

[160] A. Zinke, R. Kretz, E. Leggewie, and K. Hössinger. *Monatsh. Chem.*, 83:1213, 1952.